BUNDESWEHR UNIVERSITY
Munich

Advances in Grayscale Lithography Modeling

by

Bassem Badawi

Full copy of the thesis approved by the Department of
Electrical Engineering and Information Technology
of the Bundeswehr University Munich for obtaining the doctoral degree
Doctor rerum naturalium (Dr. rer. nat.)

Advisor
Prof. Dr. rer. nat Christoph Kutter
Prof. Dr. rer. nat Alfred Kersch

The docotral thesis was submitted at the Bundeswehr University Munich on December 19, 2022 and accepted by the Department of Electrical Engineering and Information Technology on March 7, 2023. The oral examination took place on March 8, 2023.

ABSTRACT OF THE DISSERTATION

Advances in Grayscale Lithography Modeling

by

Bassem Badawi
Doctor rerum naturalium (Dr. rer. nat.)
Bundeswehr University Munich, 2023

In this work, an alternative simulation approach for positive-tone photoresist modeling in grayscale lithography is developed, which is called the "three-state lithography model". The algorithm is adjacent to the state-of-the-art simulation programs, with a particular focus on a straightforward photomask desing procedure. The model performance is tested on spherical, pyramidal and chess field structures with a vertical resolution limit of 20-40 nm. Determining parameters and surface optimization of the produced 3D-topographies is presented in detail. Moreover, market analysis for grayscale lithography shows possibilities for the application of the semi-empirical approach developed in the present thesis. In addition, a modified process flow for the fabrication of a low-noise junction-gate field-effect transistor (JFET) is presented with lower process costs and reduced environmental footprint through the use of the grayscale lithography technique. The grayscale lithography model that is developed is suitable for the integration into commercial photomask design software or as add-on feature in state-of-the-art lithography simulators.

ZUSAMMENFASSUNG DER DISSERTATION

Fortschritte in der Modellierung für Grautonlithographie

von

Bassem Badawi
Doctor rerum naturalium (Dr. rer. nat.)
Bundeswehr Universität München, 2023

Innerhalb dieser Dissertation wird ein alternativer Simulationsansatz mit dem Namen "three-state lithography model" neben den herkömmlichen Modellierungmethoden für Positivfotolack in der Grautonlithographie entwickelt. Das Modell ist als Ergänzung zu kommerzieller Simulationssoftware mit einem Fokus auf eine vereinfachte Fotomaskenherstellung entwickelt worden. Getestet wurde der Algorithmus an sphärischen, pyramiden- und schachbrettförmigen Strukturen, welche eine vertikale Auflösungsgrenze von 20-40 nm aufweisen. Die Festlegung der Modellparameter und Oberflächenoptimierung der hergestellten 3D-Topographien werden im Detail vorgestellt. Darüber hinaus wird anhand einer Marktanalyse für Grautonlithographie das Potential für die Anwendungen des hier entwickelten Algorithmus aufgezeigt. Ergänzend wird ein Prozessfluss für die Herstellung eines rauscharmen Sperrschichtfeldeffekttransistors modifiziert, welcher durch die Nutzung von Grautonlithographie die Herstellungskosten und den umwelttechnischen Fußabdruck bei der Produktion verringert. Der entwickelte Algorithmus kann auf einfache Weise in Designprogramme für die Fotomaskenherstellung oder in kommerzielle Lithographiesimulatoren integriert werden.

"Den Wahn erkennt natürlich niemals,

wer ihn selbst noch teilt"

Sigmund Freud

Acknowledgments

Over the course of my academic career, I have met many people who inspired and guided me into becoming a technological scientist. At the same time, I have had the chance to meet people from a range of interdisciplinary fields. Whoever reads this acknowledgement section and who is not mentioned personally should know that I definitively appreciate all of the investments that others have made in my personal growth. Sadly, this section must remain at a readable length, so I will concentrate here on people with the most impact on me from my subjective point of view.

I want to thank Prof. Dr. Ignaz Eisele for the chance to begin my academic career at the Fraunhofer EMFT and for the initiative for the topic of the present PhD thesis.

A huge thank you goes to Prof. Dr. Christoph Kutter for his continuous mentorship. You showed me the relation of my own presence to achievable goals. I appreciate the open discussions we have had, not just about scientific topics, and that you always managed to have a free slot for me despite your demanding role as Director of the Fraunhofer EMFT.

Another person of importance is Dr. Peter Ramm, aka Mr. 3D. In the second part of this thesis, you began mentoring me in your unique, unconventional way. I really appreciate the scientific, strategic and political discussions we have had. Even our arguments were useful and pushed me in the right direction. You deserve particular recognition for the trust you have placed in my work and the chance you gave me to join scientific committees. It was a pleasure to work in team "hetero-integration".

I want to also thank the whole cleanroom staff at the Fraunhofer EMFT for their support and discussions, especially Dr. Armin Klumpp, Erwin Hacker, Horst Hengelmann, Josef Weber, Dr. Reinhard Merkel and Andreas Drost.

Finally, I want to thank my family. All of you influenced me positively and have been an important safety net and foundation of my strength. A special thank you goes to Jasmin Güngör for your love, your ongoing support, our mountaineering adventures and the sympathetic hint that 40 days constitutes a limited time frame.

Table of Contents

List of Figures

List of Tables

LIST OF SYMBOLS

$\boldsymbol{A, B, C}$	Dill parameters
$\boldsymbol{A, a, b, c, d,}$ $\boldsymbol{e, f, g, h}$	Fit parameters
C	Carbon
$\mathbf{CO_2}$	Carbon dioxide
$\boldsymbol{D_0}$	Initial photoresist thickness
DMSO	Dimethyl sulfoxide
DNQ	Diazonaphthoquinone
$\boldsymbol{D_x}$	Feature width
$\boldsymbol{D_y}$	Feature length
$\boldsymbol{E}$	Exposure dose
$\boldsymbol{E_{Clearance}}$	Clearance dose
$\boldsymbol{E_{shift}}$	Altering threshold
$\boldsymbol{f}$	Focal length or frequency
$\boldsymbol{G}$	Gap mask/substrate
$\boldsymbol{GS}$	Fill factor
H	Hydrogen
$\boldsymbol{h}$	Planck's constant
$\mathbf{H_2O}$	Water
HMDS	Hexamethyl disilizane
$\boldsymbol{I}$	Light intensity
$\boldsymbol{I_0}$	Incident light intensity
$\boldsymbol{I_d}$	Fourier pattern intensity
$\boldsymbol{k_1}$	K-factor
$\boldsymbol{k_F}$	Fourier factor
KOH	Potassium hydroxide
$\boldsymbol{k_x}$	Wave vector
$\boldsymbol{k_y}$	Wave vector
$\boldsymbol{M}$	Reduction ratio
$\boldsymbol{N}$	Number of slits
$\mathbf{N_2}$	Nitrogen
$\boldsymbol{NA}$	Numerical aperture
NaOH	Sodium hydroxide
NMP	1-methyl-pyrrolidone
$\boldsymbol{p}$	Pattern pitch
$\boldsymbol{P_{1,2}}$	Phase intersection points
S	Sulfur
$\boldsymbol{Si()}$	Sine integral
$\boldsymbol{T}$	Photoresist thickness
TMAH	Tetramethylammonium hydroxide
$\boldsymbol{w_F}$	Resolution limit projection lithography
$\boldsymbol{w_L}$	Resolution limit proximity lithography
$\boldsymbol{\alpha}$	Angle in xy-place or absorption coefficient
$\boldsymbol{\beta}$	Angle in yz-plane
$\boldsymbol{\theta}$	Object-sided opening angle
$\boldsymbol{\kappa}$	Extinction coefficient
$\boldsymbol{\lambda}$	Wavelength of light

LIST OF ACRONYMS

AFM	Atomic force microscopy
BARC	Bottom-anti-reflective coating
BPSG	Borophosphosilicate glass
CAGR	Compound annual growth rate
CLP	Classification, labelling and packaging
CMOS	Complimentary metal oxide semiconductor
DRAM	Dynamic random access memory
DWL	Direct-write lithography
FFT	Fast Fourier transformation
HEBS	High-energy-beam-sensitive
JFET	Junction-gate field effect transistor
LCoS	Liquid-crystal on silicon
LED	Light emitting diode
MEMS	Micro-electro-mechanical system
MOE	Micro-optical elements
MOEMS	Micro-opto-electro-mechanical system
MtM	More-than-Moore
OPC	Optical proximity correction
PAC	Photoactive compound
PEB	Post-exposure bake
RCR	Risk characterization ratio
STM	Scanning tunneling microscopy
TACD	Technology computer-aided design
TARC	Top-anti-reflective coating
TSLM	Three-state lithography model
t-SPL	Thermal scanning probe lithography
RET	Resolution enhancement technique
WLO	Wafer-level optics

CHAPTER 1

Introduction

Over the past three decades, grayscale lithography has steadily gained prominence in both industrial and scientific communities. The ability to create desired 3D-topographies on a surface through a cost-efficient method has enabled grayscale lithography to improve the field of micro-optics, micro-electro-mechanical systems and microfluidics, as well as semiconductor applications.

The generation of arbitrary 3D-shapes can be accomplished through various lithography technologies (i.e. laser-beam, e-beam, x-ray or traditional UV exposure). Due to complex photomask preparation methods and their intensive manufacturing requirements, traditional UV exposure technology becomes quite time-consuming and cost-intensive for the production of 3D-topographies. For this reason, direct-write techniques for grayscale lithography spread because tool manufactures offer competitive systems as an alternative to traditional mask-based lithography. Nevertheless, traditional lithography is a still state-of-the-art technique in the mass production of micro- and nanotechnology devices.

Standard lithography simulation tools use sophisticated numeric algorithms to simulate the solubility of a photoresist following exposure, which requires for detailed knowledge of the optical properties of the illumination system that is used and the known parameters of standardized photoresist materials. On the one hand, current simulators offer high prediction qualities and include several sub-models that are required to simulate diffusion or interference effects; on the other hand, however, these software tools are costly and often require for increased simulation experience to generate sufficient results. In addition, the state-of-the-art simulation programs do not offer automatic photomask generation methods,

resulting in expensive photomask design procedures. In order to simplify the current mathematical process of simulating the photoresist solubility, a straightforward semi-empirical approach is developed in the present thesis that is conjungable with commercial photomask design software. Moreover, this mathematical concept makes an easy optimization procedure possible, improving upon current simulation applications. This model has been bestowed the name "three-state lithography model" (TSLM) due to the three distinct solubility phases that occur in the photoresist during exposure.

Beginning from the physical and engineering background of modern photolithography, developments in binary and grayscale lithography are presented. A detailed market analysis for grayscale lithography is provided with regard to future applications before the state-of-the-art positive-tone photoresist lithographic simulation techniques are presented. The development of the TSLM and its optimization will be discussed in greater detail and subsequently tested on spherical, pyramidal and chess field structures to examine the TSLM prediction performance. Moreover, the present work presents an alternative process flow for producing a low-noise junction-gate field effect transistor (JFET), replacing the traditional lithography via grayscale lithography and resulting in lower process costs and a reduced environmental footprint.

CHAPTER 2

Physical and engineering background

This chapter provides information about physics, mathematical expressions, and applications, both in theory and engineering. The background content in this chapter does not claim to be fully complete. Rather, this chapter aims at explaining the basic physical and engineering knowledge necessary to follow the outcomes of this work.

2.1 The Fraunhofer diffraction and interference of light

Pointing a laser beam on a lattice with slit pitches in the range of the laser wavelength is a common experiment to show students the wave nature of light. The simple set-up of a low budget laser pointer and a screen-printing frame with the right mesh creates stunning faces when an interference pattern appears at the wall on the backside of the set-up. The physical phenomena of light diffraction was observed long ago, mentioned by Francesco Maria Grimaldi's in his work *"De Lumine"* in 1665.[1] Isaac Newton's theory of the corpuscular nature of light stands in contrast to the wave nature of light that was claimed by Grimaldi and later by Thomas Young. The double slit experiments conducted by Thomas Young could have strengthened this perspective. A mathematical description of Young's observations, mostly ignored by the scientific community at this time, are given by Augustin Fresnel[1, 2]. The experiments of Young, Fresnel, and Arago revealed that the distance between the maximum light intensities of the interference pattern is dependent upon the lattice slit pitch. These researchers also examined the correlation between the slit size and the light intensity distribution. According to the Fraunhofer diffraction, the intensity distribution in the far field of an incidental plane wave traveling through a two-dimensional lattice follows the

expression[2, 3]

$$\frac{I}{I_0} = \text{sinc}^2\left(\frac{D_x k_x}{2}\right)\text{sinc}^2\left(\frac{D_y k_y}{2}\right)\left(\frac{sin\left(\frac{N k_x p}{2}\right)}{sin\left(\frac{k_x p}{2}\right)}\right)^2\left(\frac{sin\left(\frac{N k_y p}{2}\right)}{sin\left(\frac{k_y p}{2}\right)}\right)^2, \tag{2.1}$$

where λ is the wavelength of the plane wave, α is the angle in the x-plane, β is the angle in the y-plane, D_x and D_y are the slit length and width, p is the slit pitch, N represents the number slits, and $\text{sinc}(x) = sin(x)/(x)$. The factor I_0 refers to the maximum light intensity propagating through the slits and can be measured in the zero-order of diffraction. It is expressed as $I_0 = (D_x D_y)/(\lambda\ d))^2\, I_i$[3], where I_i represents the intensity of the plane wave and d is the distance measured between the lattice and observer plane. The spatial frequencies are expressed by $k_x = 2\pi sin(\alpha)/\lambda$ and $k_y = 2\pi sin(\beta)/\lambda$. For all simulations in this chapter $I_i = 1$ W, $\lambda = 365$ nm and $d = 1$ cm, which satisfies the rule-of-thumb $d > D_{x,y}^2/\lambda$ for Fraunhofer approximation.[2] Figure.2.1 shows the two-dimensional interference pattern for a lattice, with $N = 10$, $p = 1.5$ µm, $\lambda = 365$ nm and $D_{x,y} = 1.3$ µm.

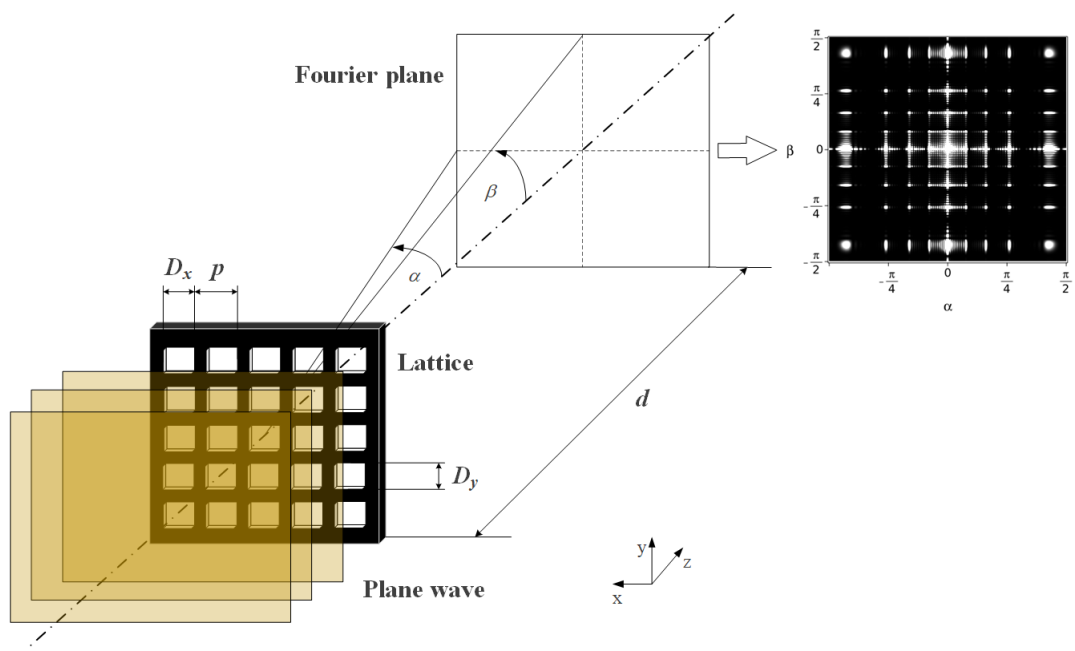

Figure 2.1: Plane wave propagates through lattice in z-direction. In the Fourier plane, a diffraction pattern appears dependent upon the lattice specifications.

Modifications of the lattice, lead to a change of the interference pattern in the Fourier plane. A cross-section of the interference pattern for a varied slit amount N, a slit pitch $p = 1.5$ µm, and a slit size $D_{x,y} = 1.3$ µm for $\beta = 0$ is illustrated in Fig.2.2a-Fig.2.2c. The intensity of the diffraction orders increases by the factor N^2.[3] Secondary maxima between the order of diffraction occur at the amount of $N - 2$.[4]

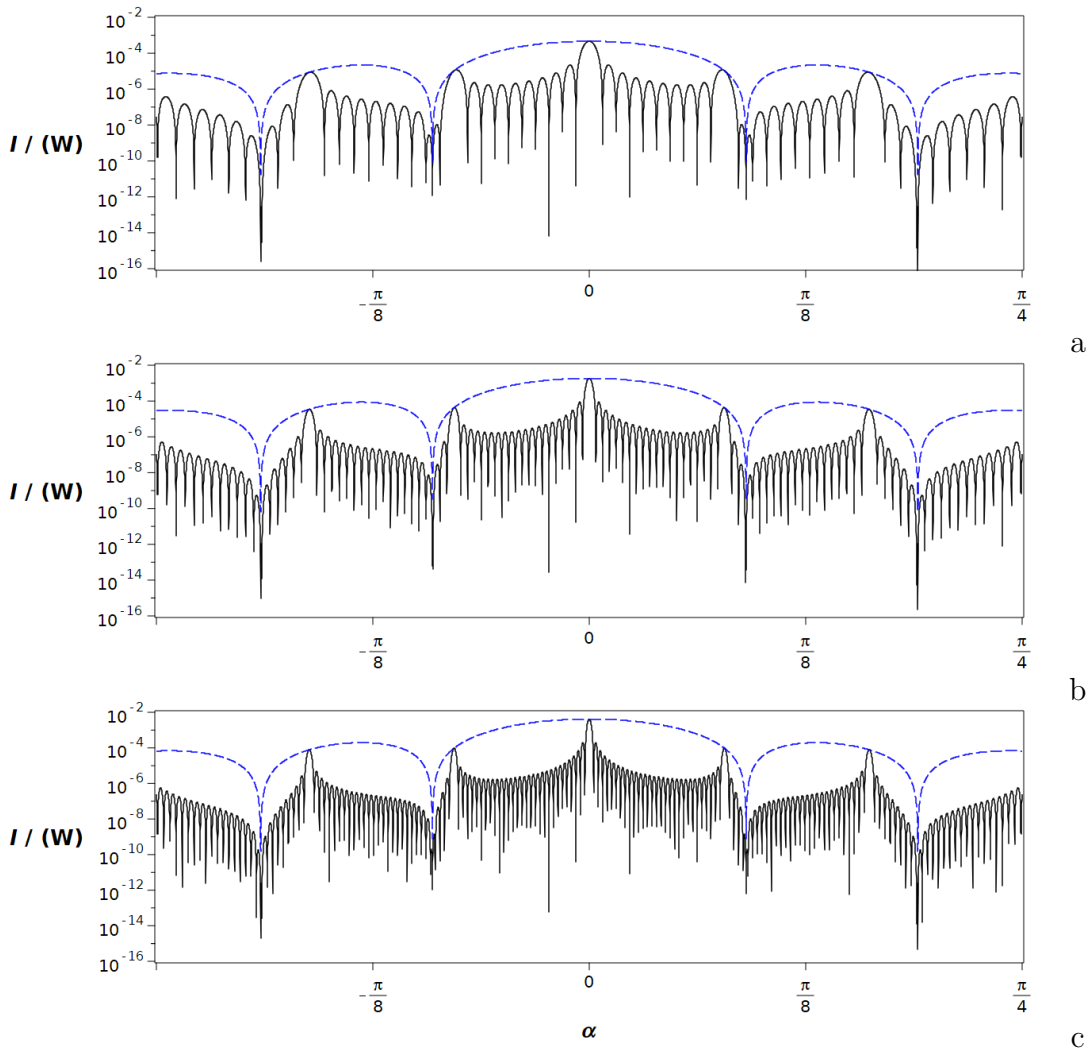

Figure 2.2: Cross-section of the interference pattern in the Fourier plane for $\beta = 0$ and different slit amounts $N = 10$ in a, $N = 20$ in b and $N = 30$ in c. The solid lines represent the interference pattern while the dashed lines correspond to the related sinc-function of Eq.2.1

Modifying the slit size D_x or D_y changes the intensity distribution of the interference pattern. The smaller the slit size, the broader and homogenous the light intensity that is

distributed over the interference pattern in the Fourier plane. The sinc-functions of Eq.2.1 limit the intensities of the interference pattern. Example interference in cross-sections for $\beta = 0$ and lattices with varied slit sizes from $D_{x,y} = 0.7$ µm to 1.3 µm are displayed in Fig.2.3.

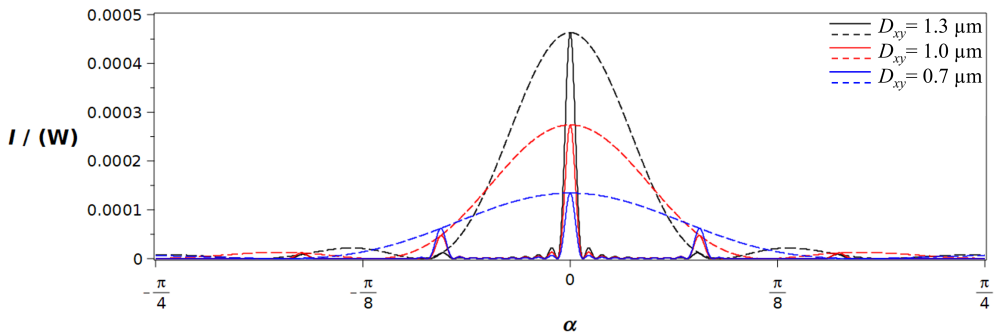

Figure 2.3: Cross-section of the interference pattern in the Fourier plane for $\beta = 0$ and slit sizes $D_{x,y} = 0.7$ µm-1.3 µm. Solid lines represent the interference pattern and dashed lines correspond to the related sinc-function of Eq.2.1

The position of the interference maxima is determined by the last two terms of Eq.2.1. While the number of slits N affects the interference orders full half width maximum (FWHM) and intensities, the slit pitch p defines their angle of appearance. Figure 2.4 shows the cross-section in the Fourier plane of the interference pattern for $\beta = 0$, $N = 10$, $D_{x,y} = 1, 3$ µm

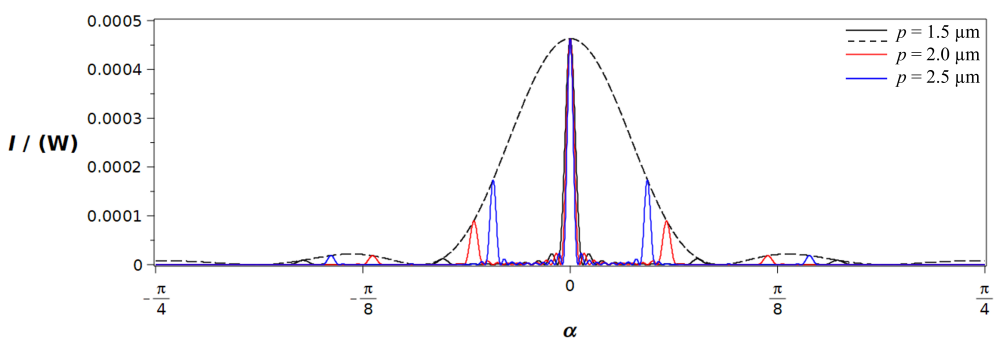

Figure 2.4: Cross-section of the interference pattern in the Fourier plane for $\beta = 0$ and slit pitches $p = 1.5$ µm-2.5 µm. Solid lines represent the interference pattern and dashed lines correspond to the related sinc-function of Eq.2.1

and varied slit pitch from 1.5 µm-2.5 µm. The first interference orders ±1 shifting to smaller angles for larger slit pitches. Through their shift, they also gain intensity due to the remaining shape of the sinc-function.

The ability to calculate the interference pattern is invaluable for designing optical systems today. By knowing the interference pattern, an image of an object can be controlled in the Fourier plane or an object can be manufactured in order to produce an interference pattern of desire, which is applied in this work.

2.2 Introduction to Fourier optics

In the previous section, we described the observed interference pattern by the Fraunhofer diffraction, which is a simplified version of the Fresnel approximation valid in the far-field. This approximation is not just easier to solve than the Fresnel diffraction, it also simplifies the calculation of the interference pattern by a simple Fourier transformation of the object transmittance[5]. For this reason, the plane in which the interference pattern occurs is referred to as a Fourier plane. An effective realization of the Fraunhofer condition can be achieved through an optical system that consists of two lenses, which is illustrated in figure Fig.2.5. The lens L_1 with a focal length equal the to distance between the source and L_1

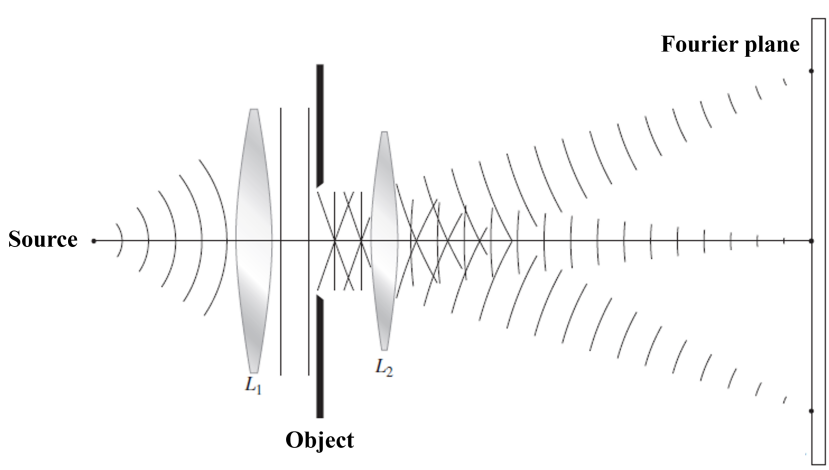

Figure 2.5: Fraunhofer diffraction using lenses, so that the source and interference pattern are in convenient distances from the aperture.[2]

transformes the wavefront to a plane wave, which subsequently propagates via the object before lens L_2 images the Fourier transformation of the object in a distance equal to the focal length of L_2.[2] Controlling the Fourier plane distance offers the possibility to manipulate the image from an object by using an aperture in the Fourier plane. Doing so cuts out desired spatial frequencies. Figure 2.6 illustrates the spatial filtering for a 4-f imaging system. A

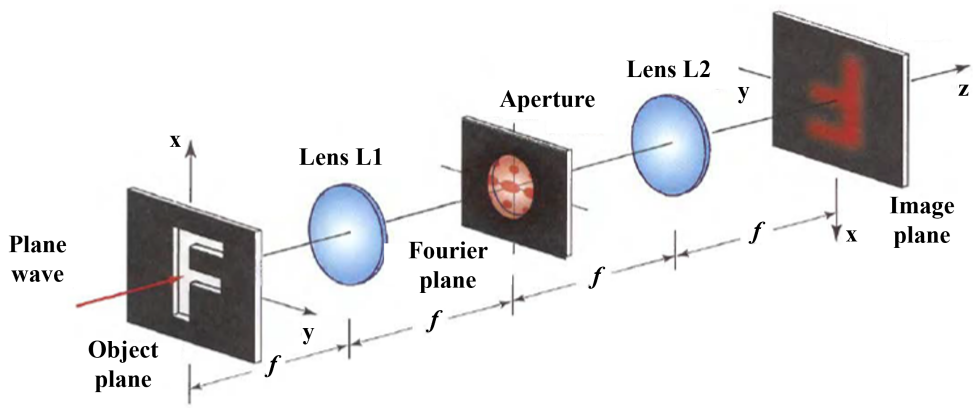

Figure 2.6: Spatial filtering in a 4-f imaging system.[3]

plane wave travels in z-direction through the object, which sits in the focal length f of the lens L_1. In distance f behind lens L_1, the Fourier transformation of the object occurs in the Fourier plane in which a circular aperture is placed. The manipulated Fourier transformation is inversely transformed by lens L_2 with similar f to L_1. The picture of the inverse Fourier transformation appears in the image plane in distance f behind the lens L_2. Beyond the inverted image of the object, the image of the object suffers from low contrast, which is caused by the filtering of higher spatial frequencies. This behavior is similar to digital electric filters, where signals are analyzed and filtered in the Fourier space. One example for spatial filtering is shown in Fig.2.7. The Lunar Orbiter picture in Fig.2.7a shows horizontal lines in the image, which relate to vertical points in the Fourier transformation in Fig.2.7c. The manipulated Fourier image is displayed in Fig.2.7d and the inverse transformation in Fig.2.7b shows a corrected image of the moon surface with improved image quality.

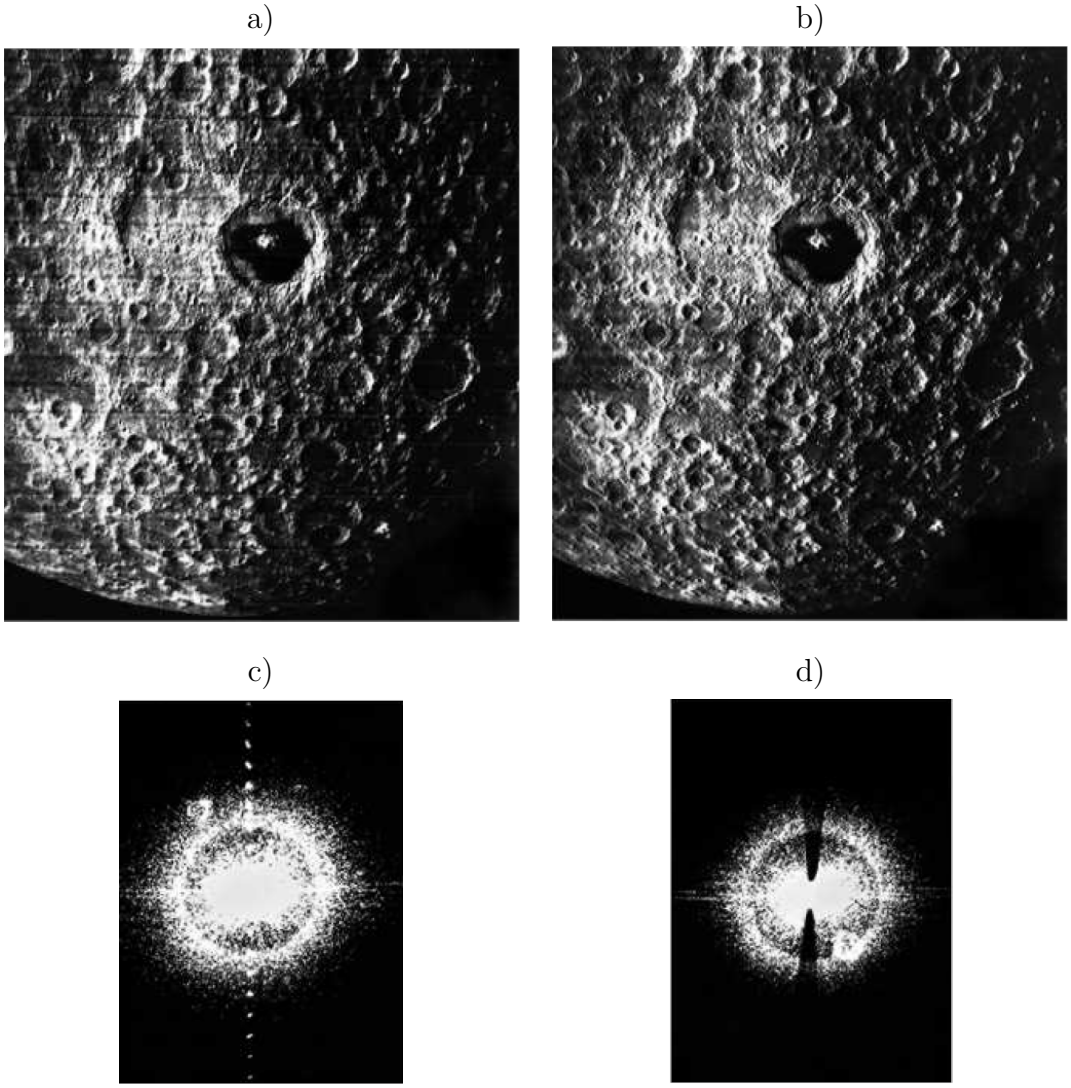

Figure 2.7: Spatial filtering of Lunar Orbiter picture from the moon surface. In a) the original image and in c) the Fourier transformation of a) is visualized. The corrected moon surface image in b) does not contain horizontal lines. The manipulated Fourier transformation of c), which produces b) by inverse Fourier transformation, is shown in d).[2]

2.3 Insights in photolithography

In the semiconductor industry, the photolithography process is considered state-of-the-art for the transition of highly complex circuit patterns drawn on a photomask and exposed on a silicon substrate, which is known as a wafer. According to Gordon E. Moore, the number of components per integrated function will double per year in the future.[6] Later, Moore revised this position to doubling components per integrated function only every two years.[7] Nevertheless, this shrinking of electronic components demands extraordinary high control of the lithography sub-processes with high costs for lithography cleanroom tools. An example for a photolithography process in the semiconductor industry is illustrated in Fig.2.8 for one mask level. The process, with a positive-tone photoresist, consists of several sub-processes that will be described in detail in the following subsections. It should be mentioned that process flow and process parameter can vary depending on the demands of the produced pattern, the materials that are used, and the exact product specifications.

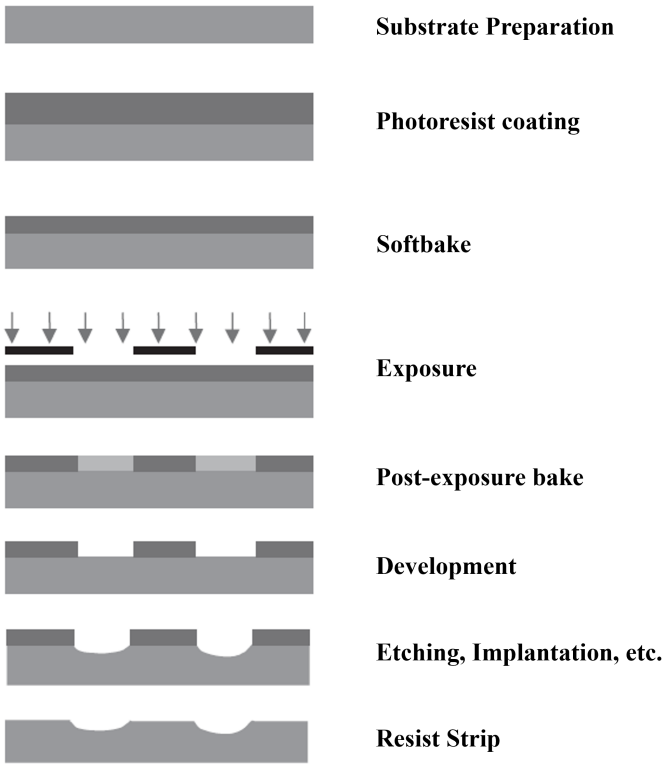

Figure 2.8: Example of a typical process, illustrated for a positive resist.[8]

2.3.1 Substrate preparation

The preparation of the substrate is applied to improve the adhesion of the photoresist and to provide a contaminant-free substrate surface. This preparation includes a chemical/mechanical substrate clean to remove contamination, a dehydration bake to remove water, and the coating of an adhesion promoter.

In the first step, particles and pre-process residuals are removed either by pure chemical treatment or a hybrid chemical-mechanical treatment. Any remaining particles on the substrate surface would result in defects in the final resist pattern, whereas film contamination can cause poor adhesion and the subsequent loss of linewidth control. The basis for wet chemical cleaning in semiconductor front-end technologies is the RCA-clean to remove metal contamination and particles.[9] Due to high chemicals consumption, a grown semiconductor market and environmental restrictions new cleaning processes, such as the IMEC-clean, are now applied with a relatively minimal consumption of chemicals and environmental impact. Next to wet chemicals, organic and inorganic residuals are removable via plasma stripping.[8]

Subsequent heat treatment removes adsorbed water from the substrate surface. This step is also known as a dehydration bake. Temperatures between 200 °C to 400 °C are applied for up to 60 minutes.[8] MicroChemicals GmbH, a supplier of AZ ECI photoresists, recommends a bake temperature of 120 °C for just a few minutes. A two-step cleaning process with acetone and isopropyl alcohol lead to the same result. However, the dehydration bake does not completely remove the water from silica surfaces, including silicon, polysilicon, silicon dioxide, and silicon nitride. A remaining water monolayer forms covalent-bonded silanol (SiOH) to the silicon surfaces atoms, which resist bake temperatures of up to 600 °C. As a result of the immediate rebuilding of silanol in nondry environments, the preferred removal of silanol is via chemical means.[10]

Heating the substrate to over 140 °C will crack OH-bonds of any oxidized surface such as, silicon, glasses, quartz or ignoble metals.[10] Otherwise, these OH-bonds form a hydrophilic surface with inferior photoresist adhesion. A sufficient suppression of the rebuilding of OH-groups in air ambient is difficult to establish and impractical. For the formation of an

adhesion layer, silanes are often used. The most common silane is hexamethyl disilizane (HMDS). On water free surfaces, HMDS bonds with their silicon atom to the oxygen atom of oxidized substrate surfaces, by the release of ammonia. If necessary, OH-bonds of the substrate surface are cracked in the reaction. The chemically bonded non-polar methyl groups form a hydrophobic surface with correspondingly good resist wetting and adhesion. HMDS can be either spin-coated or vapor-deposited. Spin-coating of HMDS only displaces a small amount of the silonal groups when the surface is not entirely free of water. Vapor deposition at elevated temperatures and reduced pressure delivers better adhesion performance, and is therefore the preferred method of deposition.

2.3.2 Photoresist coating

Accurate and homogeneous photoresist coating over the full substrate is crucial for the lithography process. For a circular substrate, in particular, which is the standard shape for substrates in semiconductor industry, the spin-coating process has been carried out as a state-of-the-art coating method. The film thickness, depends upon the spin speed and the photoresist viscosity, which is displayed in Fig.2.9. Stringent requirements are essential

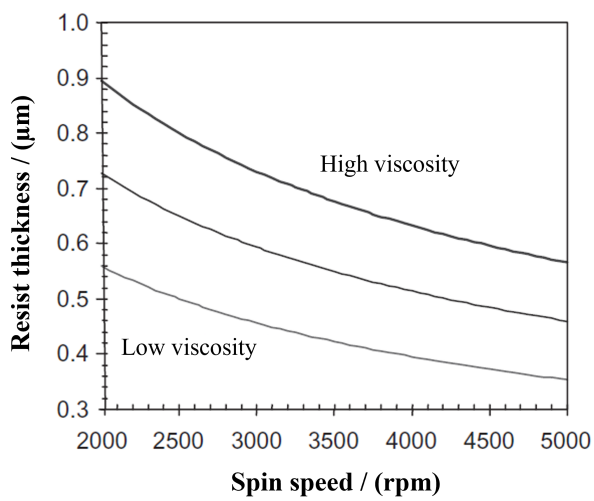

Figure 2.9: Spin curves of an arbitrary photoresist with different viscosities.[8]

for thickness control, uniformity, and low defect density in this process. Beyond spin speed,

static (substrate stationary while resist is dispensed) or dynamic (substrate spinning while dispense) dispense, dispense volume, spin acceleration, surface topography, and substrate material also play important roles in the resist thickness uniformity. On the one hand, the short cycle times of less than one minute makes this process advantageous in the industrial production; on the other hand, this process suffers from a very low yield of the dispensed photoresist volume. Only a small percentage of the dispensed photoresist remain as a film on the substrate.[10] The majority of the photoresist is spun off the substrate edges and ends up as waste material. At the moment, this fact is of just minor interest in the semiconductor industry and constitute a mere cost factor for low-priced products. It will, however, play a more important role in the future when the environmental impact of production will be internalized into the product costs.

As an alternative to spin-coating, spray or dip-coating are applied to deposit a photoresist film onto a substrate. Both techniques deliver significantly higher photoresist yields, with up to 15% for spray-coating and 100% or 50% in double- or single-sided dip-coating processes.[10] Spray-coating advances the coating uniformity for textured substrates in instances where spin-coating is not technically feasible or does not provide sufficient results with regard to homogeneity and the edge coverage of the resist film over the substrate topography. Photoresist droplets are formed via a gas-filled nozzle or ultrasonic atomization and then spread over the substrate surface. Spray-coating delivers non-uniform thicknesses above the surface structures. The film thickness is typically thinned on texture edges and thickend in the grooves near sidewalls. Due to the statistical distribution of the droplets and a minimum droplet density needed for a closed photoresist film, it is difficult to produce thin films < 1 µm.[10] Dip-coating is exploited either for substrate types that are not suitable for spin-coating or spray-coating, or when the photoresist yield plays an important role for product costs. In vertical dip-coating processes, substrates are dipped into a cuvette filled with photoresist and then drawn out at a steady speed. The produced photoresist film thickness is adjusted depending upon the draw speed. Next to the vertical dip-coating, a roll-to-roll dip-coating is used for continuous substrates, e.g., flexible electronic substrates.

This coating technique is not suitable for substrates with strong textures and applications where double-sided coating or the coating of holes and trenches is not desired.

2.3.3 Softbake

After the coating process, liquid photoresists contain a residual solvent concentration of up to 40%, depending upon the film thickness and the solvent used (details about photoresist components will be discussed in Sec.2.4).[8] The evaporation of the remaining solvent in a subsequent bake step, known as softbake or prebake, is chiefly necessary to stabilize the photoresist film. A less solvent contain in the photoresist film also leads to:[10]

- a reduction of photomask contamination and sticking for contact lithography;
- a prevention of nitrogen forming of DNQ-based photoresists during exposure;
- an improved photoresist adhesion on the substrate surface;
- a minimization of the dark erosion for positive-tone photoresists;
- the possibility of multiple resist coating sequences;
- a prevention of bubbling of evaporated solvent in subsequent thermal processes;
- an increase of the softening point necessary for the thermal stability in the subsequent thermal processes.

Solvent in the photoresist diffuses to the film surface before it is evaporated into the ambient air. Like the other diffusion process, the material transport - in this case the solvent in the photoresist - is dependent upon temperature and concentration. Typically, bake temperatures of 90-100 °C lower the residual solvent concentration below 5% in a reasonable amount of time.[10] Elevated temperatures would result in even lower solvent concentrations but are not necessary and are often detrimental for most processes following the softbake (e.g., increased mechanical stress in thick resist films, decomposition of the photoactive component (PAC), and cross-linking and/or oxidization of the resin).

The most common technique to apply a softbake on the photoresist is the contact or proximity bake on a hot plate. The heat gradient for standard silicon substrates can be neglected due to the high thermal conductivity of silicon. For other substrates with low heat conductivity, baking in a convection oven is considerable for better temperature control on the substrate surface. In general, proximity baking is preferable due to the reduced particle contamination, the improved uniformity of the bake temperature, and the reduced cycle times against the bake in contact to a hot plate or in a convection oven. For accurate control of the baking time, a chill plate is necessary to cool the substrate after the bake step within a short timeframe and abort the baking. Otherwise, the bake process continuous uncontrolled during a convection cool-down in ambient air with undesirable results.

Next to the solvent, also the water content in the photoresist decreases through the softbake procedure. Photoresists with a photoinitiator that is based on diazonaphthoquinone (DNQ) require a certain amount of water for the chemical reaction during the exposure process. For detailed information about the transformation of DNQ-photoresist during exposure, Sec.2.4 discusses this topic in detail. In order to increase the water content after softbake, the photoresist has to rehydrated. The rehydration occurs in ambient air and diffusion limited. Thus, the rehydration process for thick photoresist films takes longer to establish a homogeneous water concentration and is dependent on the ambient air humidity for a given temperature. In case of a 22 µm thick AZ 9260 photoresist, the insufficient rehydration process stretches the development for up to two hours, while a delay of 10 minutes between softbake and exposure minimizes the development time to several minutes. Humidity of 40-50% is recommended for sufficient rehydration.[10] Humidity under this limit would result in photoresists that are too dry. Above 50% humidity the photoresist adheasion onto the substrate is decreased, which aggravates the coating process. Higher temperatures would shorten the diffusion time but lead to dryer photoresist films.

2.3.4 Exposure

Like the principle of analog photography, the photolithography exploits the chemical conversion of a photosensitive material to copy the image of an object onto a substrate surface. During the exposure a photosensitive material is chemically transformed, which leads to a different solubility for exposed and unexposed areas in developer medium. Different techniques and tools for exposure have been invented in recent decades in order to satisfy the demands for continually shrinking structures. The desired lateral variation of the exposure energy on the photosensitive surface can be achieved either with maskless or with mask-based exposure techniques. In mass production industries (e.g., semiconductor industry), the mask-based illumination systems are state-of-the-art due to their high troughput. For this reason, this work concentrates on the mask-based techniques which can be differed in contact, proximity, and projection lithography, which are illustrated in Fig.2.10, without ignoring maskless methods.

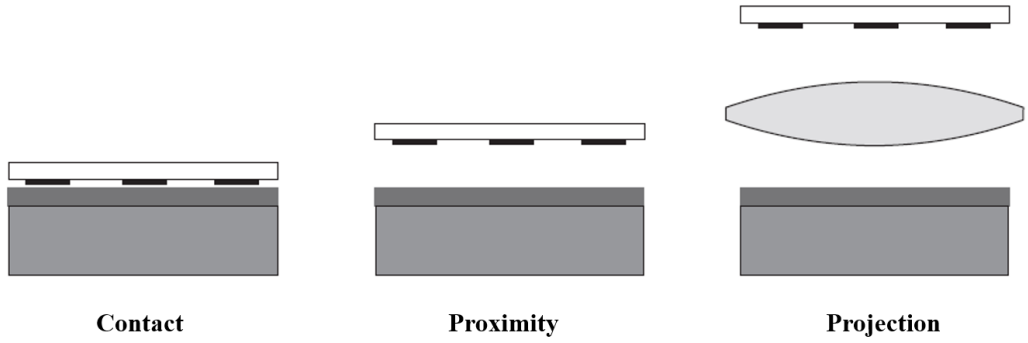

Figure 2.10: Lithographic printing in semiconductor manufacturing evolved in the early 1960s from contact printing to projection printing, progressing between mid-1970s to today.[8]

2.3.4.1 Proximity and contact lithography

Contact and proximity lithography is the simplest method to expose a photosensitive substrate through a patterned photomask. Contact imprinting delivers a resolution limit in the range of the used wavelength. In practice, these techniques result in damages and particle

contamination of the mask. The resulting low yield during the exposure process makes this method unsuitable for mass production industries. Proximity lithography overcomes this issue through a gap between the photomask and the coated substrate surface, but the resolution limit for an enhanced production yield is sacrificed in this method. The resolution limit in proximity lithography processes is expressed as line-width (half pitch) w_L and follows the expression[11]

$$w_L = \frac{3}{2}\sqrt{\lambda\left(G + \frac{D_0}{2}\right)} \sim \sqrt{\lambda G}, \tag{2.2}$$

where λ is the exposure wavelength, G is the distance between substrate surface and photomask and D_0 represents the photoresist film thickness.

Modern tools for proximity lithography are called mask aligner. The principle optical system of such systems is showed in Fig.2.11. Mercury plasma lamps are usually used as UV-light sources. The emitted light is collected by an ellipsoidal mirror and reflected towards the condenser lens by another mirror, which collimates the incident light. Behind the condenser, there is an integrator unit that is placed there for homogenizing and shaping the light before it is reflected by mirrors towards the front lens. These systems provide divergence angles of approximately ±3°-±5°.[11] Typically, a fly's eye condenser or Köhler

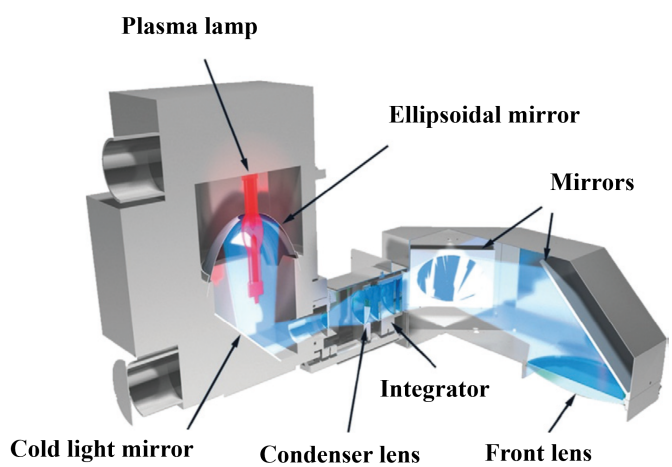

Figure 2.11: Scheme of the optical system of a mask aligner for proximity lithography. The light is collected by an ellipsoidal mirror and collimated by a condenser lens. An integrator unit provides uniform illumination with a well-defined angular spectrum.[11]

integrator, as illustrated in Fig.2.12, is exploited for the light homogenization in a mask aligner. The Köhler integrator consists of two similar plano-convex microlens arrays placed in their same focal length $f_{1,2}$ as well as a Fourier lens. Modern arrays carry up to hundred of thousands different light channels. Every light channel acts as a miniaturized Köhler illumination system. The Fourier lens images every channel into the Fourier plane, where all of the sub-images from the first array are superimposed, resulting in an uniform irradiance distribution of 2% for full field exposure.[11] To decouple the irradiance uniformity from the

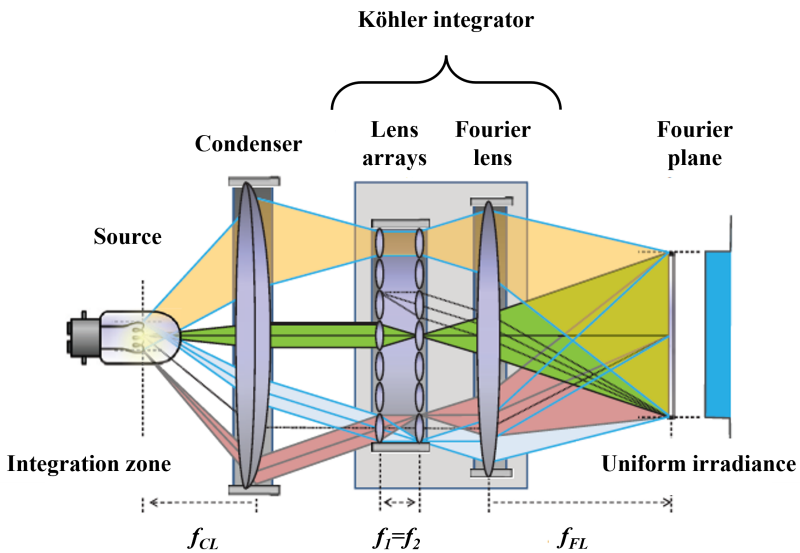

Figure 2.12: Scheme of a microlens-based Köhler integrator as used for light homogenization in a mask aligner.[11]

sort of used light source and possible misalignment of the light source, modern tools for proximity lithography are often equipped with a tandem Köhler integrator unit, where a second Köhler integrator is placed in the Fourier plane of the first. Between the integrator units, it is possible to integrate filters for spatial filtering.[12]

After the front lens, the light is diffracted from the photomask, which is placed above the substrate surface at a distance from 30-100 µm.[11] Due to the narrow gap between the photomask and the substrate surface, the Fraunhofer approximation used in Sec.2.1 is not valid. Therefore, the light distribution in the near field onto the substrate surface follows

the Fresnel diffraction.[11]

The precise alignment of the substrate to the photomask is invaluable for creating a multilayered device. Mask aligners typically achieve a photomask to substrate alignment precision of 0.5 µm at best. In mass production, the heating amid exposure can lead to a significant deformation of the photomask, which limits the alignment accuracy to just 2 µm.[11]

The fabrication of power devices[13], micro-electro-mechanical systems (MEMS),[14, 15, 16, 17] or bio/chemical sensors[18] requires a front-to-back alignment during the lithography process. In contact or proximity lithography several techniques are developed for this purpose. Reports show an alignment accuracy of 5 µm for infrared mask aligners, which are only applicable with infrared transparent substrates and film stacks near the alignment marks. Enhanced alignment accuracy of under 1 µm are delivered by double-sided mask aligner systems[19]. This tools are also suitable to align front- to backside of opaque substrates.

2.3.4.2 Projection lithography

As manufacturing capabilities for refractive optics in the mid-1970 became sufficiently advanced so that the image quality was only dependent on the diffraction limit and not on the abberations of the optical system, the projection lithography took place in the mass fabrication of micro-system.[20] Two different systems for projection lithography exist on the market, scanning and step-and-repeat (short stepper) systems. Their working principle is illustrated in Fig.2.13. The first projection lithography tools, produced for the fast growing semiconductor industry, were scanners. These systems align a wafer on a wafer stage to a photomask and illuminate the photomask through a slit with a monochromatic wavelength in a 1:1 reduction ratio (in terms of object to image size). Wafer and photomask are then moved synchronized to image the photomask pattern onto the substrate. The exposure dose of scanning systems is determined by the light intensity, scanning speed, and slit width. Step-and-repeat systems expose the wafer in image fields. Here again, photomask and wafer are aligned to each other but only the wafer is moved in xy-direction. The same field of

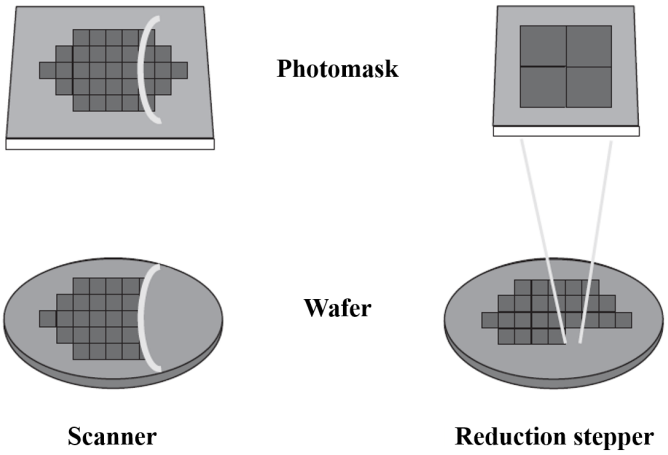

Figure 2.13: Scheme of scanner and stepper projection technique.[8]

the patterned photomask is repeatedly imaged onto the substrate at a certain chip size that is determined by the reduction of the optical system. The reduction capability of steppers simplifies the photomask production, especially for high-resolution imaging. In the early to mid-1980s, steppers began to dominate the projection lithography for mass production and were used throughout the 1990s.[8] A hybrid lithography tool using the step-and-scan concept combines the virtues of scanners and stepper systems. These lithography tools repeatedly scan individual exposure fields on the substrate and include an optical system with reduction possibilities.[21] The step-and-scan technique is considered state-of-the-art in current lithography tooling for mass production projection lithography.

The optical systems in modern tools for projection lithography require outstanding manufacturing precision with regard to their optical components, which makes them one of the main cost factors in a lithography tool system, a fact that is nicely illustrated by the ASML PAS5500 wafer stepper in Fig.2.14. Here, the operator works in front of the workstation. Substrates are inserted via wafer cassettes into the tool manually from the operator. For high performance projection lithography, the photoresist coating equipment interfaces with the illumination tool and transfers the substrates automatically. In the single wafer process, a photoresist coated wafer is taken from the cassette or photoresist coating equipment and transfered onto the wafer stage. There it is aligned underneath the projection lens and illu-

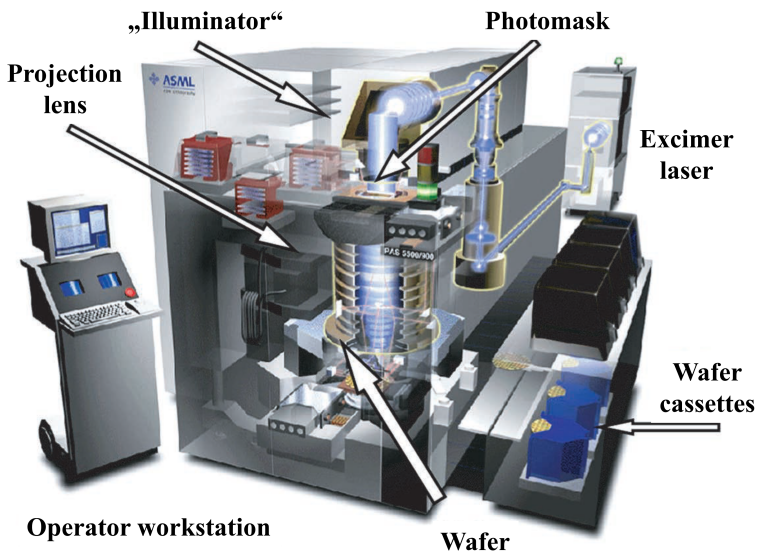

Figure 2.14: Schematic of ASML PAS5500 wafer stepper.[22]

minated from the top. The photomask sits on the reticle stage above the projection optics in the light path. To make adjustments of the exposure energy, a shutter is used to determine illumination time per exposure field.

The resolution limit, expressed as smallest printable feature w_F of all these systems, is based upon the the Rayleigh-criterion and follows[22]

$$w_F = k_1 \frac{\lambda}{NA}, \tag{2.3}$$

where λ corresponds to the source wavelength, NA is the numerical aperture, and k_1 is a varying factor dependent on the applied photoresist process (also called the k-factor). In the past, resolution enhancement has generally been done by decreasing of the exposure wavelength or increasing the numerical aperture. The first scanner optics exhibit numerical apertures of 0.16. At the same time, optical systems of contemporary stepper or step-and-scan systems achieve NA of 0.93 (and greater than 1 for immersion lithography).[8]

With modern projection lithography tools, the numerical aperture has already hit a feasible maximum. The light source wavelength plays an important role in the ongoing shrinkage of critical dimensions. The initial projection tools were equipped with mercury-arc lamps. Optical filters were also applied to cut the optical spectrum for monochromatic

illumination. In the 1990s, mercury-arc lamps are replaced from excimer lasers, pushing the resolution limit towards 150 nm. In the 2000s, excimer lasers have been considered state-of-the-art to print features under the illumination wavelength, though now new light sources in the extreme-ultraviolet spectrum are pushing the resolution limit to 7 nm.[23] Figure 2.15 displays the shrinkage of printable feature sizes over time alongside the illumination wavelength used. Table 2.1 lists the applied light sources of past and current lithography tools alongside their source wavelengths and location in the electromagnetic spectrum. The

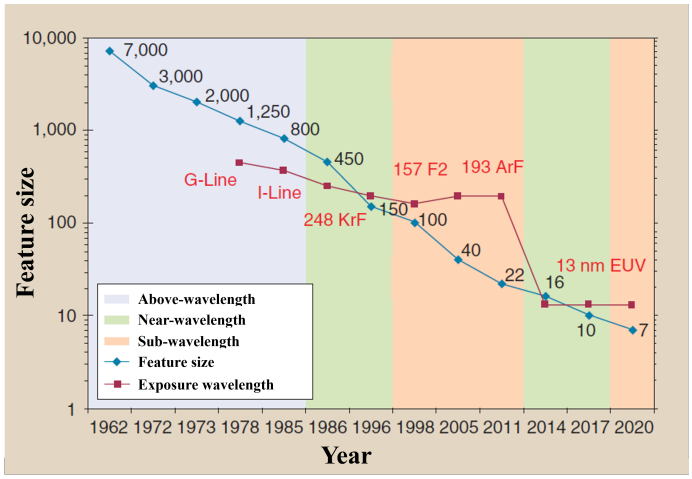

Figure 2.15: Semiconductor lithography trends that show the transistor feature size versus the lithography lamp/laser light wavelength.[23]

Table 2.1: Light sources and wavelengths used in projection lithography.[22, 24]

Light source	**Type**	**Wavelength/(nm)**	**Location in the el. spectrum**
Mercury-arc lamps	g-line	436	Visible
	h-line	405	Visible
	i-line	365	Mid-ultraviolet
		240-255	Deep-ultraviolet
Excimer lasers	KrF	248	Deep-ultraviolet
	ArF	193	Deep-ultraviolet
Laser produced plasma	Xe,Sn	13	Extreme-ultraviolet

trend of lithography is differed in three cycles, namely above-wavelength, near-wavelength, and sub-wavelength, where the smallest features are above, near, or under the illumination wavelength. Since the invention of the 150 nm node, the gap between illumination wavelength and feature size has been growing, as has the requirement for complex techniques to resolve this structures.

A single light spot is mathematically expressed by an Airy-disc. With respect to Eq.2.3 the smallest distance between two distinguishable Airy-discs next to each other is fixed for $k_1 = 0.61$.[22] This relationship considers the resolution limit only from an optical point of view and neglects the chemical properties of the photoresist, decoherence of the light source, and resolution enhancement techniques (RET). A more accurate prediction of the resolution limit of the applied lithography process is necessary when it comes to yield enhancement. Figure 2.16 shows the evolution of the k-factor over time. Conventional lithography stands for k-factors values above 0.65, where lithography processes do not demand for RET. Mild RET and strong RET are required for k-factors between 0.65-0.5 and from 0.5-0.25, which represents the limit of single-exposure optical lithography.[25] Source optimization, optical

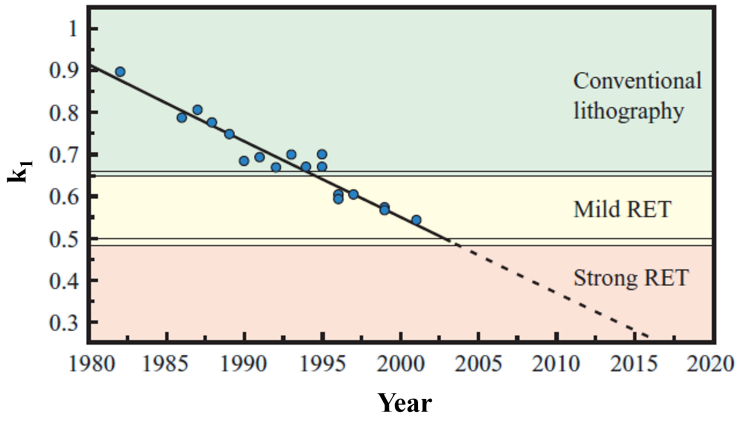

Figure 2.16: Trend of k_1 values in IBM semiconductor manufacturing lithography for several generations of exposure wavelength and numerical aperture.[25]

proximity correction, and multiple pattering are the most advanced RET to print features in the mild and strong RET area within an acceptable process window and affordable yield.[26]

As the effort increased over time to print consistently smaller features, the costs per single lithography layer have increased significantly.

The alignment accuracy in projection lithography systems is crucial for shrinkage in semiconductor industry. Next to the resolution limit of the lithography tool, the overlay of subsequent lithography layer is essential for the functionality of fabricated devices. The overlay defined precisely in SEMI Standard P18 is as follows:[27]

> *Vector quantity defined at every point on the wafer. It is the difference $\vec{O}$ between the vector position $\vec{P_1}$ of a substrate geometry, and the vector position of the corresponding point $\vec{P_2}$ in an overlaying pattern, which may consist of photoresist.*

As the feature sizes shrink, the overlay tolerances also have to be tightened. Overlay limitations for different semiconductor technologies are displayed in Tab.2.2 for producing a dynamic random access memory (DRAM). The overlay limits of modern projection systems

Table 2.2: DRAM overlay requirements from the 2008 International Technology Roadmap for Semiconductors.[22]

Node (DRAM half pitch)/(nm)	**Year**	**Overlay requirement/(nm)**
68	2007	13.6
45	2010	9.0
32	2013	6.4
22.5	2016	4.5

are almost three powers smaller than the alignment strategies that proximity lithography can deliver. This level of accuracy is only feasible by applying sophisticated alignment strategies consisting of a mechanical prealignment, an intermediate optical alignment, and a fine alignment procedure. The basic principle of alignment is the translation of the wafer coordinate system into the stage coordinate system, which is precisely controlled and monitored. With the alignment to the photomask, laying on the reticle stage, lateral, and rotational alignment errors of the substrate to exposure field are adjusted via stage movements. Back-to-front alignment in projection lithography is not a common technique. ASML published

a method to project backside alignment marks to the frontside, where it can be measured by the frontside alignment system. An embedded lens system in the wafer stage provides the back-to-front projection of the alignment marks. The tested back-to-front alignment accuracy is < 500 nm.[28] This back-to-front overlay accuracy enables a high precision fabrication of various MEMS and MOEMS devices that is not possible with proximity or contact lithography.

2.3.4.3 Alternative lithography technologies

Next to classical proximity and projection lithography, alternative technologies have been established in order to solve the primary shortcomings of the conventional exposure systems. All of these alternatives are faced with their own problematic circumstances. Alternative lithography technologies, considerable also for grayscale lithography, are discussed in this section, with their specific benefits and disadvantages outlined compared to the conventional techniques.

X-ray lithography is a noteworthy example of an alternative exposure technique. Motivated from the very short wavelength of 6.7 Å and 15 Å,[22] the hope was significant that it would allow for the resolution limits of conventional lithography to be overcome. Nevertheless, even at these illumination wavelengths, significant diffraction occurs for desired features sizes under < 100 nm. Due to a lack of refractive components in this wavelength spectrum, x-ray lithography is a proximity lithography technique with unique demands on materials. As there is no existing high transparent material for x-ray radiation, the photomask pattern is not produced onto quarz or soda-lime glass substrates but onto a thin membrane < 2 µm[22] comprised of low-atomic-number material. Materials with high-atomic-number are used for the mask pattern on top of the membrane substrate. Silicon carbide is commonly used as membrane material, while compounds of tantalum show beneficial properties for the use as high-atomic-number material due to the compatibility with various etch and cleaning processes.[22] Like UV-proximity lithography, the absence possibility of pattern reduction increases the demands for mask production. Before interest in EUV lithography took hold,

x-ray lithography had been seen with the high potential to overcome the resolution limits of conventional lithography technologies. As a result of the extraordinary demands for mask manufacturing, most x-ray lithography programs have been scaled back or terminated.

The direct exposure of the photoresist is known as direct-write lithography (DWL). The source of illumination of these lithography systems can be laser beams, accelerated electrons, or ions. Acceleration of electrons at energies of 5-100 keV require photomask feature sizes on the atomic level to be diffracted and enables the print of features at the size of 10 nm or below.[22] This lithography technique is commonly used for mask manufacturing and has little contribution to mass production, due to the slow writing times. A brief example calculation examines a writing time of over one week for a 300 mm wafer substrate in a 22-nm technology.[22] The relationship of the resolution R to the area throughput T for different lithography technologies are displayed in Fig.2.17. This image was published in the year 2003. Compared to the Fig.2.15, advanced RET and the change to EUV illumination have ensured a feature size shrinkage down to 7 nm in the range of e-beam lithography with similar or better throughput to past DUV systems. The empirical law of Tannet,

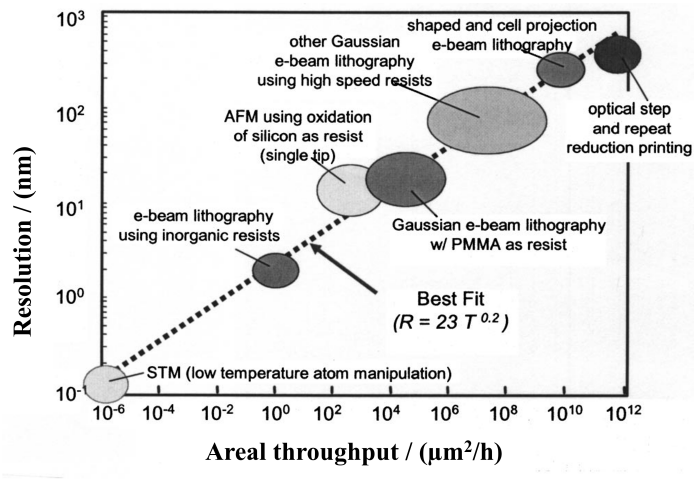

Figure 2.17: Resolution-area throughput trade-off of lithographic techniques.
Abbreviations: STM = scanning tunneling microscopy, AFM = atomic force microscopy[29]

invented by Tennat D. M. in the year 1999[30], is represented by the best fit in Fig.2.17 and is not valid for modern optical reduction lithography. For e-beam lithography, the energy

deposition in the substrate also has to be taken into consideration. While e-beam writing is commonly used in photomask production without problems due to the larger feature sizes on a photomask used in reduction systems, the direct-writing lead to thermal distortion of the substrate and then result in overlay errors with significance for the 22-nm technology and beyond. Sophisticated multi-e-beam direct-write[31], cell projection[32], and scattering-mask electron-projection (SCALPEL)[33] systems have been established in order to enhance writing times. Nevertheless, these systems still cause thermal distortion dependent upon the beam current and therefore limit writing speed. High speed electron-beam lithography tools also require very fast data processing. Hsin-I Liu et al.[34] demonstrate the need of 12 Tb/s using 22 nm pixels for 45 nm feature sizes. This data rate thus require high-end electronics and data processing for these lithography systems. The electron-beam direct-write systems are commonly used in prototyping or cutting-edge technologies that deal with low volumes. This technology can only barely fulfill the demands in mass production due to the limitation of throughput or efforts to increase the throughput towards suitable amount. Nevertheless, e-beam writing or hybrid approaches, in which critical structures are printed by e-beam writing and only repeated structures are printed by projection lithography, constitute some well-established lithography techniques.[35]

Laser direct-wirte is an well-known technique in photomask fabrication but is also applied for direct patterning of photoresists[22, 36]. By applying multiple beams, laser direct-write has significant higher throughput compared to the electron-beam direct-write method in photomask production. The resolution limit with an Argon ion laser at a wavelength of 257 nm was determined to be suitable for a feature size of 200 nm.[37] Compared to e-beam the laser direct-write technique deposits much less energy into the substrate but cannot deliver similar resolution limits. Nevertheless, laser direct-writing enables multiphoton lithography based upon nonlinear photon-photoresist interactions.[38] This technique is commonly used to produce 3-dimensional topographies, which is further discussed in Sec.3.1 of this work. The basis of this technology is the exposure with ultra-fast laser pulses, which causes a two-photon absorption in the focus of the laser beam. The principle of two-photon absorption is

fundamentally different from that of one-photon excitation. In linear absorption processes, an atom or molecule is excited by the absorption of a single photon with an energy $E_{ph} = hf$, where h is the Planck‘s constant and f is the frequency of the electromagnetic wave. The linear absorption process only occurs if the photon energy is greater than the band gap $E_{gap} < E_{ph}$ of the exposed atom or molecule. A similar excitation state is achieved for the simultaneous absorption of two photons with $E_{gap} > E_{ph}$. The energy transfer from two photons towards the molecule happens over a virtual energy state in the band gap of the exposed material. The two-photon absorption process increases for higher laser intensity, which requires for ultra-short laser pulses.[38] The most applied laser source for 3D-printing is a Ti:sapphire laser oscillator in the near infrared spectrum of light approx. 800 nm with femotsecond pulse width, repitition rates in the MHz range, and pulse energies of 2-40 nJ or higher. Laser sources with higher repitition rates in the GHz range are not commonly used, as the optical system need higher design efforts. Amplified laser systems also play an alternative role to the laser oscillators for multi-photon polymerization processes. Ultra-fast frequency-doubled fiber lasers at wavelength around 780 nm are applied in industrial tools due to the cost-efficiency of such systems. A significant number of publications operate with green laser sources in a wavelength spectrum approx. 500–532 nm.[39] Direct-laser printing tools offer two basic writing modes: the dot-by-dot or line-by-line processing. Line-by-line writing is advantageous for the throughput and results in smoother surfaces. The most commonly used systems work with line-by-line writing. Like e-beam systems, laser direct-write technologies enable a further increase of the throughput, which is generated by multiple laser beams. Diffractive optical elements[40, 41] or digital mirror devices[42] are commonly used as spatial light modulators in such DWL tools. In a projection based direct-write grayscale lithography system, a liquid-crystal on silicon (LCoS)-chip is applied to modulate the light intensity of a UV-light emitting diode (LED) array at a wavelength of 405 nm.[43]

DWL alignment strategies differ significantly from the known procedures in proximity and projection lithography. In e-beam direct-write lithography, back-scattered electrons are used to align onto double cross marks.[44]. With the application of Barker marks and hybrid

alignment strategies, the modern e-beam lithography achieves an overlay accuracy in the sub-10 nm range.[45, 46] However, during the alignment procedure the photoresist is exposed by the electron beam. For this reason, e-beam exposure doses must be kept small, which limits the total number of alignment structure reads. In addition, the signal-noise ratio decreases for a low trench depth of the alignment marks. The limit of this alignment strategy was found for 70 nm mark step height.[45] Laser-DWL systems offer optical alignment strategies, which enable front-to-back alignment. The maskless aligner MLA150 of Heidelberg Instruments offers global alignment accuracy of 500 nm and a backside alignment accuracy of 1 µm.[47] Polar coordinate maskless laser lithography systems provide an alignment accuracy of the rotary stage to the laser optical axis of < 400 nm.[48]

2.3.5 Post-exposure bake

The exposure of the substrate to monochromatic illumination generates a standing wave in the photoresist when the substrate is reflective. This standing wave forms scallops in the photoresist sidewalls, which are displayed in Fig.2.18. For decreasing feature sizes, the

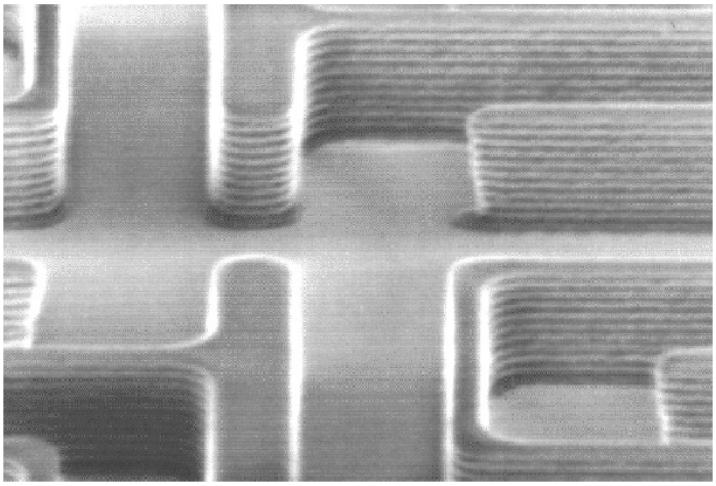

Figure 2.18: Sidewall scallops in photoresist pattern on a silicon substrate caused from standing wave formation[8]

scallops formation can affect the imaging quality significantly. In the semiconductor industry, the post-exposure bake (PEB) is applied after the exposure so as to suppress the formation

of sidewall scallops. A heat treatment is performed in order to diffuse the illuminated PAC of the photoresist. The bake times and temperature are independent on the resist thickness, but on the applied photoresist. Typical conditions of the post-exposure bake are approximately 110-120 °C for a few minutes of baking. Figure 2.19 shows the $\sin^2$-modulated intensity distribution of illuminated PAC in the direction of incidental light and after diffusion in chronological sequence until a smooth distribution of illuminated PAC within the photoresist film has been achieved.

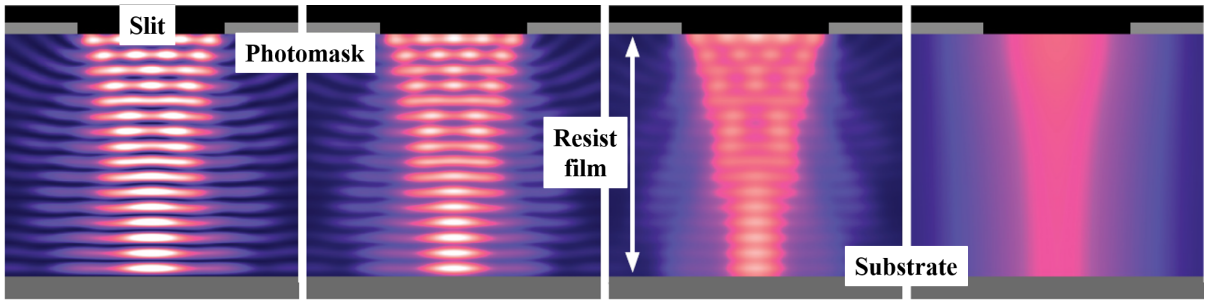

Figure 2.19: Diffusion of illuminated PAC during the post-exposure bake in chronological sequence of numerical modeling from left to right.[10]

DNQ-based photoresists do not require additional heat treatment after exposure but are commonly applied for sidewall smoothing. For chemically amplified photoresists, the PEB is a necessary step to complete the photoreaction initiated in the exposure process. A chemical amplification is introduced during the PEB. The chemical products form during the exposure and work catalytically to the chemical amplification. This enables an illumination of thick photoresist films with a relative low exposure dose. A PEB is also necessary for image inversal photoresists and cross-linking negative resists.[10]

2.3.6 Development

The development process is one of the most critical steps during the full lithographic process sequence. Depending upon the photoresist material that is used, either exposed (positive-tone) or unexposed (negative-tone) photoresist areas on the substrate dissolve in the alkaline developer medium. Common developer media used in industrial manufacturing sites include

aqueous potassium hydroxide (KOH), sodium hydroxide (NaOH), and tetramethylammonium hydroxide (TMAH) solutions. TMAH is mostly applied in complimentary metal oxide semiconductor (CMOS) applications due to the metal-ion-free composition. Commercial developer solutions contain chemical buffers against neutralization via carbon dioxide (CO_2), surface wetting and additives to remove resist residues.

Typically, the aqueous developer medium is spun on the substrate in the photoresist coating tool. Mass manufacturing tools are equipped with separated coating and development lines. The puddle development is a common development technique, in which the slowly rotating substrate is poured with a certain developer volume before it is stopped for the duration of the development time. Shacking the substrate via small rotational movements improves the development quality for high structure topographies. Following the development time, the substrate is rotated and spins off the developer medium and resolved photoresist. During the spin process, de-ionized water continuously flows onto the substrate so as to break the development immediately. Spray development is the second method to coat the substrate with developer medium, in addition to the puddle development. This technique provides a more uniform developer coverage by spraying a mist of aqueous developer medium through a nozzle across the substrate surface. A side effect of this method is the reduction of developer medium for similar results compared to puddle development.

It is clear that in terms of environmental impact, development plays a key role in the entire lithography process. Current commercially available developer solutions do not contain just alkaline media, which has to be PH-neutralized before it can be dumped, but they also contain several ingredients of environmental relevance.

The developer AZ 400 K contains 2-3% (w/w) potassium hydroxide and 3-10% (w/w) dipotassium tetraborate.[49] The developer solution is corrosive to metals, causes serve skin burns, eye damage, and is suspected of damaging fertility. Potassium tetraborate is viewed as a substance of evaluation required by the REACH article 48.[50] The substance was under investigation due to its repro-toxicity, consumer use, exposure to workers, high risk characterization ratio (RCR), and wide dispersive use. Due to the possible damage to unborn

children, the report suggests a new entry in the regulation of the substance to cover the reproductive toxicity.

Standard AZ developer contains 3-5% (w/w) disodium metasilicate and 3-5% (w/w) trisodium phosphate. This developer solution can cause serious eye irritation and damage in the case of accidentally exposure.[51] Both AZ developers provide extended bath life in batch immersion applications. Additionally, AZ 400 K developer deliver low foaming properties, which suits the developer well in spray development processes.[52]

CMOS technology require a special developer medium with minimal contamination of metallic elements. To avoid the diffusion of metal elements into the silicon substrate, TMAH-based developer solutions are the method of choice to substitute the standard KOH and NaOH developer in CMOS processes. AZ 726 MIF developer is a metal-ion-free developer solution with a concentration of 1-2.5% (w/w) of TMAH.[53] Unlike the metal-containing developer solutions, MIF developers have significant higher hazardous potential to workers and the environment, more generally. The substance TMAH is classified as corrosive to metals, harmful if swallowed, toxic when in contact with skin; it also causes severe skin burns and eye damage, may cause damage to organs, and may cause damage to organs through prolonged or repeated exposure. Concerning health effects have been reported in the literature after exposure to a low-concentrated solution of 2.38% to a skin area of 28% happened in Taiwan. Reports have also shown several fatalities with higher concentrations and smaller exposed body areas.[54, 55] Most accidents with TMAH concentrations $\leq 2.38\%$ that were monitored from the Taiwan Poison Control Center between July 2010 and October 2017 caused first-degree chemical skin injuries without systematic toxicity effects.[56]

TMAH does not just cause serious health issues to exposed persons but is in fact a critical substance in wastewater. The Taiwanese semiconductor industry uses 2,000 tons of TMAH every month.[54] In the U.S., 10-50 million pounds of the substance were used.[56] Excessive entry of TMAH into the environment over wastewater damages the aquatic ecosystems and may result in large amount of algal bloom and the eutrophication of rivers, streams, lakes, and reservoirs.[57] In order to limit TMAH pollution in wastewater, the European directive

2010/75/EU[58] regulates the maximum concentration of TMAH in wastewater to 7 ppm. Adhering to the European directive is a major challenge for the industry. Available technologies to clean wastewater include catalytic oxidation[59], electrodialysis[60], ion exchange[61], combination of membrane bioreactor with photocatalysis[62], or reverse osmosis[63], biological treatment[64, 65], and membrane distillation[66]. In the case of membrane distillation, it was possible to reduce the TMAH concentration in the wastewater to 1 ppm. With defined system specifications, an annual thermal energy consumption of 14 GWh is needed to clean 20,000 m^3 of wastewater. Expected costs were estimated to \$16/m^3 wastewater.[66]

2.3.7 Resist strip

After the development process, the generated pattern is transferred into the substrate by either dry or wet etch techniques. The patterned photoresist is also utilized as a mask for ion implantation profiles. These processes are of secondary importance to the present work and therefore are not (or only briefly) discussed in the following chapters and sections. After the pattern transfer into the substrate, residual photoresist must be cleaned (henceforth called stripped) from the substrate surface. The stripping process is also applied in the case of failures during the lithographic steps before the pattern transfer, where the substrate is cleaned for a secondary process run with adjusted process parameters.

In general, there are two classes of stripping techniques. Typically, the clean is either completed via wet stripping that uses organic or inorganic solutions, or through a plasma strip using an oxygen plasma to incinerate the organic photoresist material. Most commercial organic strippers are phenol-based. However, wet strippers for positive-tone photoresists are commonly inorganic, acid-based systems that are used at elevated temperatures.[8] Acetone as a stripper medium is not recommended due to the risk of fire and the high vapor pressure that causes photoresist streaks on the substrate.[10] NMP (1-methyl-pyrrolidone) is a stripper solvent with low vapour pressure and allows heating up to 80 °C. However, the substance is classified and labelled according to the CLP regulation (EC) No 1272/2008[67], as the substance may cause damage to unborn children. A substitution for NMP is DMSO

(dimethyl sulfoxide), which can be heated to 60-80 °C with comparable stripping perfomance to NMP.[10] DMSO is not classified as hazardous in accordance with Regulation (EC) No. 1272/2008 and is grouped in the water hazardous class D with slight hazardous effects to water. Nevertheless, a risk of reproductive effects cannot to be excluded if the occupational exposure limit value and the biological limit value is maintained for DMSO.[68] If the substrate is stable to alkaline media, aqueous 2-3% KOH or NaOH solutions may be used to remove photoresist. Cross-linked photoresist may also require higher concentrations and temperatures. In the case of too overly cross-linked photoresist, a plasma strip is recommended. Wet cleaning after the plasma strip should be applied to remove residual organic particles from the substrate surface.

2.4 Photoresist chemistry

The photoresist conceptional functionality involves the conversion of spatial distributed light energy into a spatial distribution of photoresist solubility. This principle of work is valid for all positive-tone and negative-tone photoresists, as well as for chemically amplified photoresists. Nevertheless, the chemical reactions are different for the distinct types of photoresists.

The kinetics of the photoresist is inextricably tied to the phenomena of light absorption necessary to start the photochemical reaction. The mathematical basis for the description of the absorption of light is Lambert's law in Eq.2.4 following[8]

$$I(z) = I_0 e^{\alpha_z z}, \tag{2.4}$$

where I_0 is the incident light intensity and α_z is the absorption coefficient depending upon the penetration depth z. The absorption coefficient α is related to the imaginary part of the refractive index κ following the expression[8]

$$\alpha = \frac{4\pi\kappa}{\lambda}, \tag{2.5}$$

where λ is the vacuum wavelength of the propagating light.

Positive-tone photoresists are commonly used in lithography processes for the i-line, h-

line, or g-line wavelengths. Rather than providing a review of all of the types of photoresists, this work will focus in particular on positive-tone photoresists. General principles will often apply to any photoresist.

A positive-tone photoresist involves three main components:

- A base novolac resin that acts as a matrix and provides the resist its structural properties and etch resistance;
- A photoactive compound (PAC) or sensitizer that chemically reacts at light exposure;
- A solvent that dilutes the photoresist components into a liquid suitable for spin-coating.

The chemical structure of the photoresist and the reaction of the DNQ-molecule during UV exposure is shown in Fig.2.20. The base-soluble novolac resin is rendered insoluble

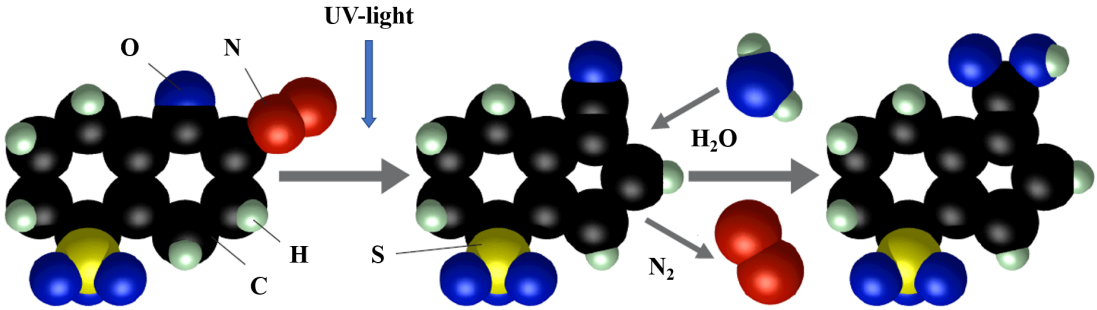

Figure 2.20: Conversion of the diazonaphthoquinone during UV exposure.[10]

through the incorporation of hydrophobic diazonaphthoquinone (DNQ). During light exposure, DNQ is converted into an indene carboxylic acid via the Wolff rearrangement[69] under the release of nitrogen N_2 and absorption of water H_2O. A certain water concentration in the photoresist is necessary for appropriate conversion. An insufficiant rehydration process (see Sec.2.3.3) leads to undesired secondary reactions (e.g., esterfication with the resin or polymerisation with CO_2 splitting). After the induced photochemical conversion of the PAC, the product is chemically bonded onto the novolac resin and turns the photoresist soluble into an alkaline medium. The development process is illustrated in Fig.2.21 at a molecular level.

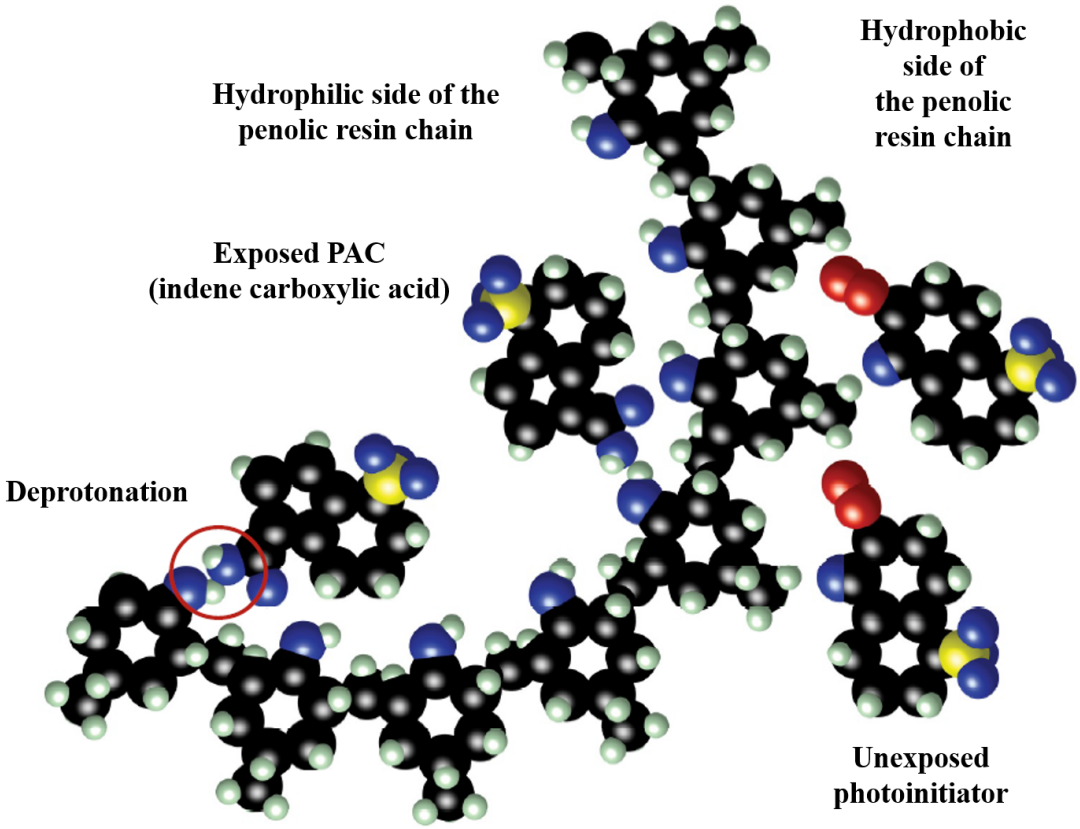

Figure 2.21: Schematic process of development for a positive-tone photoresist on a molecular level.[10]

It shows the unexposed state of the PAC located on the hydrophobic side of the phenolic resin chains. During exposure, indene carboxylic acid is formed and expands to the hydrophilic side of the phenolic resin chains. It is at this position that a proton is separated from the resin, which turns the resin molecule into a charged state. In the charged condition, the resin is soluble in the alkaline medium.

CHAPTER 3

Developments in the field of grayscale lithography

The content of this chapter focuses on the technological development, simulation techniques and applications of grayscale lithography. Starting with a review of existing technologies involved in the production of 3D-topographies and their current developments, the first section provides insight into commercial and cutting-edge grayscale lithography techniques. In a subsequent market analysis for grayscale lithography, market revenues and fabrication equipment are discussed under distinct conditions. State-of-the-art of lithography simulation and its pros and cons are also analyzed before the chapter concludes with an overview regarding applications fabricated by grayscale lithography with a focus on future market trends.

3.1 Exposure systems and techniques

The foundation for grayscale lithography is the partial exposure of photoresist, which becomes soluble either from top to bottom for positive-tone photoresist or vice-versa in the case of negative-tone photoresist. To achieve varying lateral height levels in a photoresist, the exposure dose must be modified laterally.

In 1994 and 1995, novel techniques for the production of arbitrary shaped 3D-structures using standard IC manufacturing processes were published.[70, 71] For the fabrication of the 3D-structures, a g-line stepper system was used to illuminate of a gray-tone photomask. This gray-tone photomask consists of mask features with a pitch under the resolution limit of the projection system, which results in spatial filtering of the Fourier image due to a limited numerical aperture. The intensity distribution in the areal image is adjustable either

by the modulation of the feature size or the modulation of the feature pitch, as illustrated in Fig.3.1. This approach relies upon certain restrictions. One of the demands is a medium

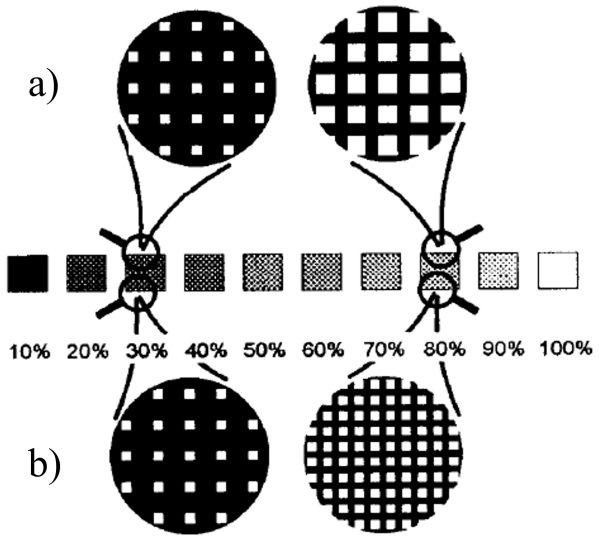

Figure 3.1: Modulation of the photomask pattern in grayscale lithography either by the variation of the feature size in a) or the modulation of the feature pitch in b).[70]

contrast of the photoresist along with a linear resist thickness loss with increasing exposure dose. Due to the significant data requirement, a data compaction solution was developed. Reimer et al. estimated the data amount for a 1x1 mm^2 element on the photomask as being about 5200 kBytes. From today's perspective, this amount of data seems handy on standard desktop computers. Reimer et al. proposed a five step data preparation procedure consisting of several correction functions, which are considered in an exclusive design software for grayscale lithography photomask design with the name "GRADED".[72, 73]

An interesting approach for grayscale lithography is the so-called half-tone proximity lithography.[74] This technique uses an aperture in conjunction with the Köhler integrator unit of the proximity illumination system and a periodic patterned photomask to print periodic 3D-structures into photoresist. The approach is a cost-efficient method to print 3D-structures into photoresist, due to the illumination system simplicity and the lower demands for photomask manufacturing. However, the design of the aperture and the photomask

require complex simulations to ensure satisfactory results.

The HEBS (high-energy-beam-sensitive) glass, which was developed by Canyon Materials Inc., is exploited in contact lithography for the lateral variation of the exposure dose. The glass itself is processed via e-beam writing and becomes more opaque for higher electron doses.[75] Beyond the disadvantages of contact lithography that were mentioned in Chapter 2, this approach requires a sophisticated procedure for the HEBS glass fabrication, as illustrated in Fig.3.2. Along with multiple test procedures necessary for investigating resist characteristics, HEBS dose calibration and possible optimization of the exposure profiles the benefit of simple contact printing is consumed for photomask fabrication.

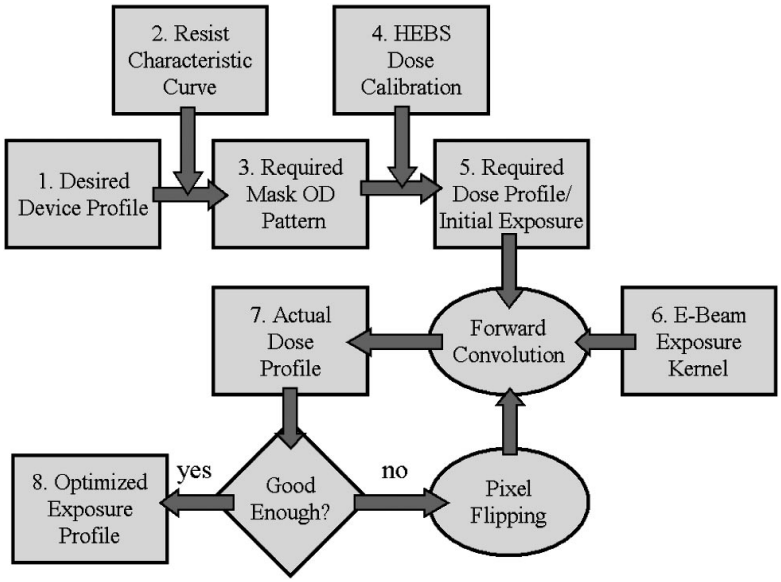

Figure 3.2: HEBS glass fabrication process flow.[75]

Maskless approaches are prominent techniques in the field of grayscale lithography. Direct-write lithography systems, in particular, are suitable for the fabrication of 3D-topographies due to the ability to adjust the exposure dose in each exposure spot. A straightforward process development detached from complicated photomask production qualify these illumination tools nicely for prototype or low volume fabrication. E-beam writing was exploited early on for the production of blazed gratings and Fresnel lenses even on non-flat substrates[76, 77]. Nevertheless, e-beam grayscale lithography produces charged surfaces and scattering elec-

trons, which widens the exposed spot size dependent upon penetration depth. Laser-based direct-write lithography represents an interesting alternative to e-beam lithography for the production of 3D-structures. Using a laser beam instead an electron beam for the exposure solves the charging issue but comes with much higher resolution limits. For high precision grayscale lithography, the two-photon direct laser-writing generates new possibilities. The two-photon photopolymerization (TPP) is considered to be one of the most important applications of two-photon absorption, which enables the intrinsic 3D fabrication for high penetration depth. The prepolymer photoresist contains three main components: the photosensitizer, the photoinitiator and the monomers. During the TPP process, two photons are absorbed simultaneously by the photosensitizer, which emits fluorescent light in the UV-visible spectrum. As a result, the fluorescent light is absorbed by the photoinitiator and gives rise to radicals. These radicals react with the photoresist monomers or oligomers, resulting in monomer radicals that expand in a chain reaction until two radicals undergo termination. Finally, the low-weight monomers are polymerized into cross-linked, high molecular weight materials. With the TPP, a lateral spatial resolution of 50 nm and an aspect ratio of 1.38 were achieved for photocured polymer lines. The application of diffusion-assisted high-resolution direct femtosecond laser-writing, woodpile structures with 400 nm intralayer period have been successfully fabricated. By using a radical quencher for the voxel tuning, lateral resolution was improved down to 100 nm[39] Thus, the continuous development of the TPP photoresists creates new possibilities for free-standing 3D-structures, as the produced fly replication in Fig.3.3 remarkably shows.

The nanoimprint lithography (NIL) was developed in the 1990s as a promising method for high volume production of nanostructures beyond the diffraction limits of projection systems. The principle of nanoimprint technology follows a straightforward process flow, which is illustrated in Fig.3.4 for traditional NIL and step-and-flash NIL (S-FIL). The NIL process uses a nanostructured hard mold that embosses its nanostructure into a polymer-coated substrate for controlled temperature and pressure conditions. The contrast image of the mold is then transferred into the substrate via anisotropic etching. In the S-FIL process flow, the

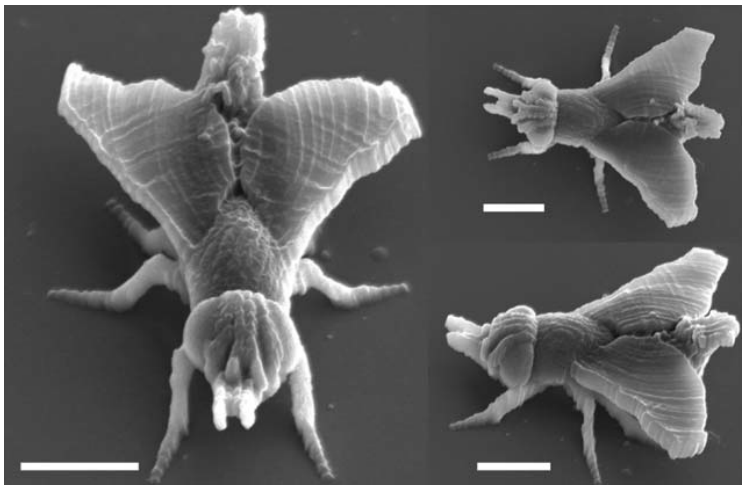

Figure 3.3: Scanning electron microscopy images of a fly fabricated by photoinitiator with radical quenching moiety. Scale bars represent a length of 5 µm.[78]

substrate is coated with an organic transfer layer. A UV-transparent mold is aligned in proximity to the substrate surface. In this position, a photopolymerizable organosilicon solution is introduced into the gap between the mold and substrate surface, which completely fills the gap. Consequently, the photopolymerizable organosilicon is exposed to UV-irradiation and polymerizes. Following the mold release, the nanostructure is transferred into the transfer layer. NIL opens up the possibility of producing sub-10 nm[79] structures with relatively small efforts compared to projection lithography. S-FIL, in particular, is considered to be a next generation lithography technique due to its ability to be performed in a step-by-step manner similar to the known principle of stepper tools. This technology offers new opportunities, especially for the mass production of 3D-structures for several application fields. The production of T-gates for microwave transistors constitutes a good example of the advantage of NIL. With the NIL approach, the classically used double e-beam lithography process can be significantly shortened from over two hours to less than 60 s[80]. Nevertheless, NIL technology faces major challenges on its way to becoming a mass production technology. Due to the direct contact to the substrate, there are defects, a risk of contamination and it exhibits an insufficient overlay accuracy.[81] In 2017, NIL overlay errors provided 2.5 nm and 4.5 nm for NIL to NIL and NIL to optical lithography.[82] These values barely achieve

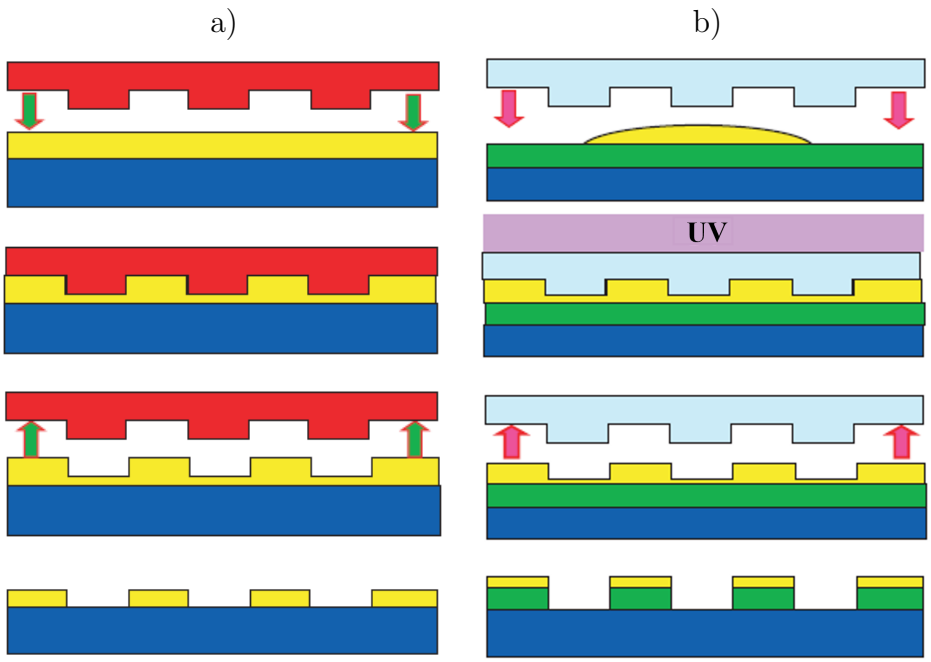

Figure 3.4: Process flow of NIL in a) and S-FIL in b).[79]

the requirements for the 22.5 nm node, but do not deliver the overlay precision required in future semiconductor applications.

Generally used in university environments rather than in mass production fabrication sites, thermal scanning probe lithography (t-SPL) plays an important role as a high precision lithography tool. The t-SPL modifies the surface material of a substrate through a heated cantilever tip, which is shown in Fig.3.5a. For surface modification, the t-SPL is categorized into the basic concepts of removal, conversion and the addition of material, which is illustrated in Fig.3.5b. The basic working principles of t-SPL provide distinct resolution limits and writing speeds. The best resolution was achieved in removal mode with 8 nm half-pitch, with a maximum writing speed of 20 mm/s. The conversion mode is tested with minimal features of 10 nm and a writing speed of 1.4 mm/s, while the additional mode provides 10-35 nm resolution limits with lower writing speed of 40 µm/s. In experiments with a NanoFrazor t-SPL tool, 3D-structures with a vertical resolution of 1 nm (1σ error) and up to 256 gray levels were produced.[84] Overlay and field stitching are in the sub-10 nm range.[83] Due to the low writing times, this grayscale lithography technique is applied for

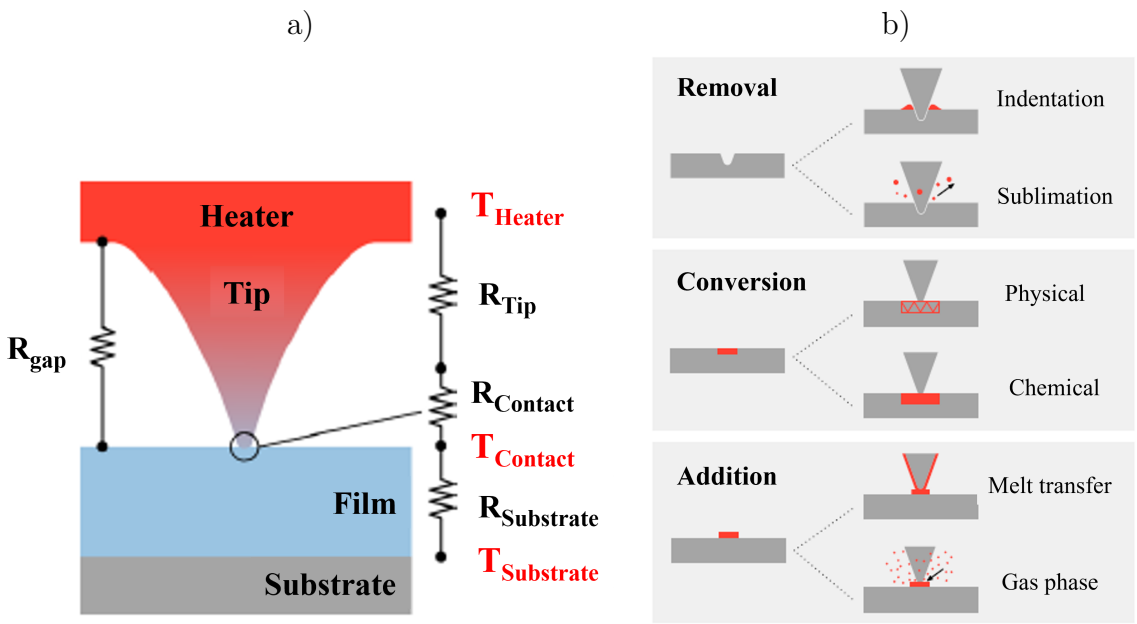

Figure 3.5: Heat transfer model of the t-SPL cantilever tip in a) and concepts of t-SPL surface modification in b).[83]

high precision prototyping and for NIL mold production. Future hybrid systems will exploit t-SPL and DWL to enhance the writing times, where just low-resolution patterns < 1 µm written with t-SPL and high-resolution patterns above 1 µm are produced by DWL.[84]

3.2 Market analysis for grayscale lithography

Grayscale lithography is commonly exploited for the production of micro-optical elements (MOE), which are key technologies in cameras, displays, light emitters and optical sensors. As illustrated in Fig.3.6, the revenue forecast by market for wafer-level optics (WLO) estimates a compound annual growth rate (CAGR) of 55% for the target markets mobile, consumer, automotive, medical and industrial.[85] The mobile market, in particular, drives overall market growth with smartphone applications. However, with more and more smart products, higher interests in virtual and augmented reality within the consumer market and the increased exploitation of micro-optical components in the medical sector, these branches have significant contributions to the total market growth.

Figure 3.6: 2012-2024 WLO-revenue forecast.[85]

In addition to the classical market of MOE, the MEMS and microfluidic branches are operational areas for grayscale lithography. The forecast of 2021-2027, illustrated in Fig.3.7, has a CAGR of 9% split by devices for the consumer, industrial, telecom, automotive, defense and aerospace and medical market, with a total volume of $13.6B in 2021 to $22.3B in 2027. The MEMS forecast is dominated by the consumer market, primarily driven by MEMS sensors and actuators that enable new functions for wearables, smartphones and other smart applications. Additionally, with a CAGR of 10% toward a revenue of $4.1B, the automotive industry will play an important role with microphones and optical MEMS in LIDAR systems, where grayscale lithography is often used to produce these components. Telecom market growth is estimated with a strong 25% CAGR from 2021-2027, where it reaches $290M. 70% of the overall market growth results from MEMS timing, replacing the formerly popular Quartz-based oscillators. MEMS oscillators will also utilized in the defense & aerospace market.[86]

Grayscale lithography plays an especially important role in the microfluidic industry. YOLE forecasts a CAGR of 10.1% with a revenue of $18.1B-$32.3B in 2021-2027. A closer look at the material repartition shows that less than 11% of the modules in the market base

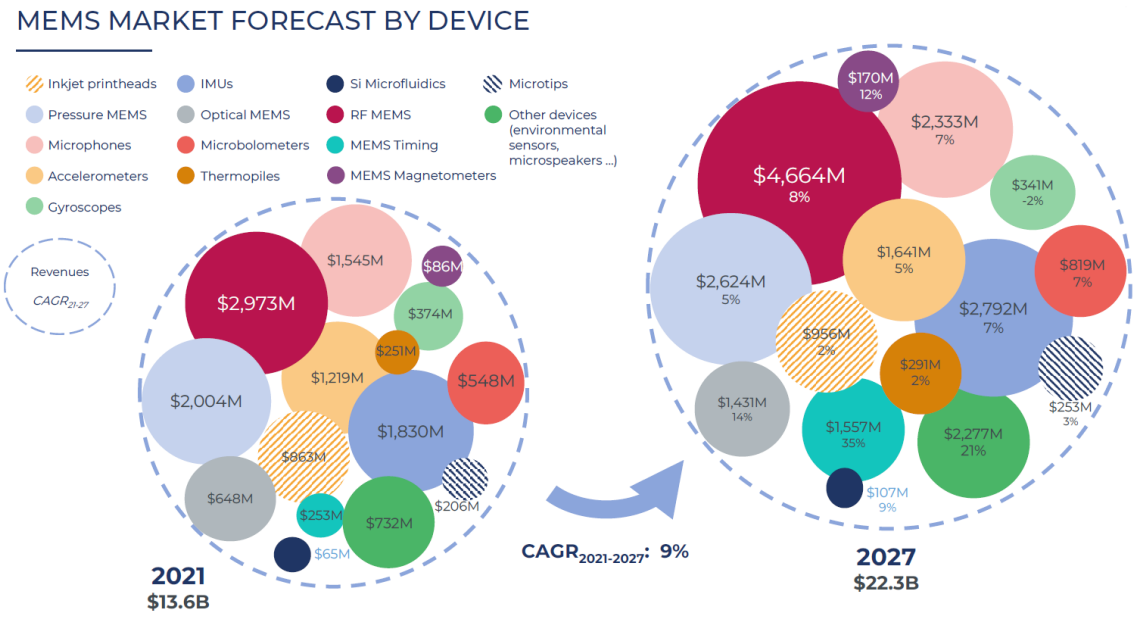

Figure 3.7: 2021-2027 MEMS-revenue forecast by device.[86]

on silicon or glass technologies.[87] The predominate material in this market is and remains polymer, which almost entirely excludes the semiconductor manufacturing industry from taking part in this technology.

NIL is seen as the future method of choice for the mass production of micro- and nanostructures. However, projection lithography remains an attractive but costly alternative. The market forecasts predict NIL a CAGR of 24% from $38M to $146M in the time horizon of 2018-2024. The main markets for NIL are photonic devices and biochips (e.g., microfluidic chips, lab-on-chips or DNA sequencing chips). It is expected that NIL could also take over the NAND fabrication from projection lithography in the semiconductor industry.[88] However, the high defect rates of the NIL process have inhibited this prediction.

Forecasts of device fabrication tooling estimates a CAGR of 5% for lithography tools with a revenue of $1.3B-$1.9B between 2020-2027. A closer look on the equipment technology used for the fabrication of future components, illustrated in Fig.3.8, reveals a strong dependence on UV projection lithography for the fabrication of photonic devices, MEMS and sensor technologies in which grayscale lithography is a standard fabrication method.[89] Figure 3.9 shows the forecast of the photolithography equipment market.

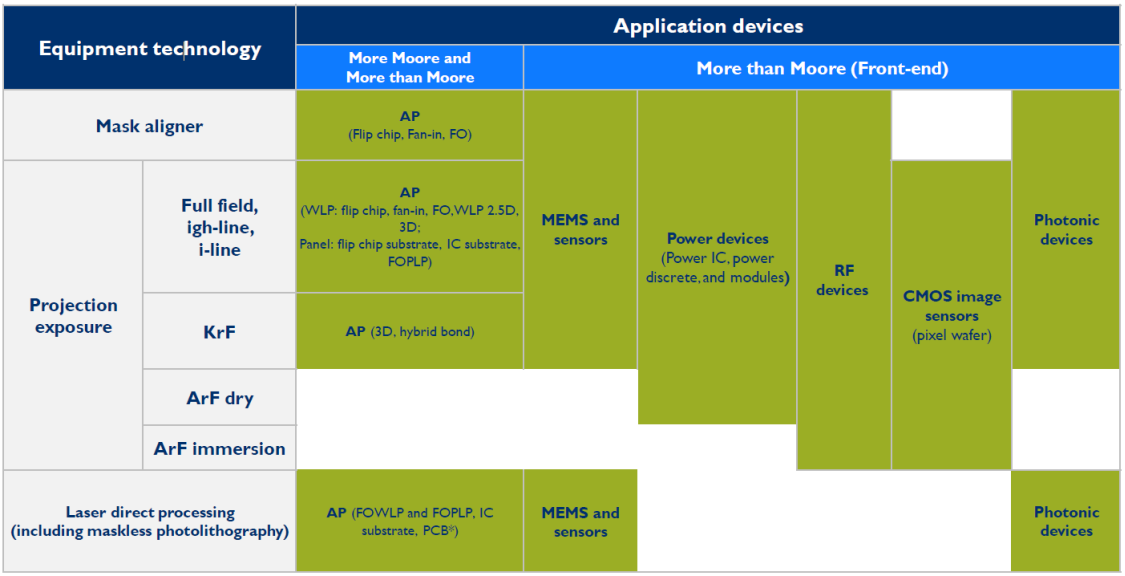

Figure 3.8: Photolithography equipment versus targeted components for the fabrication.[89]

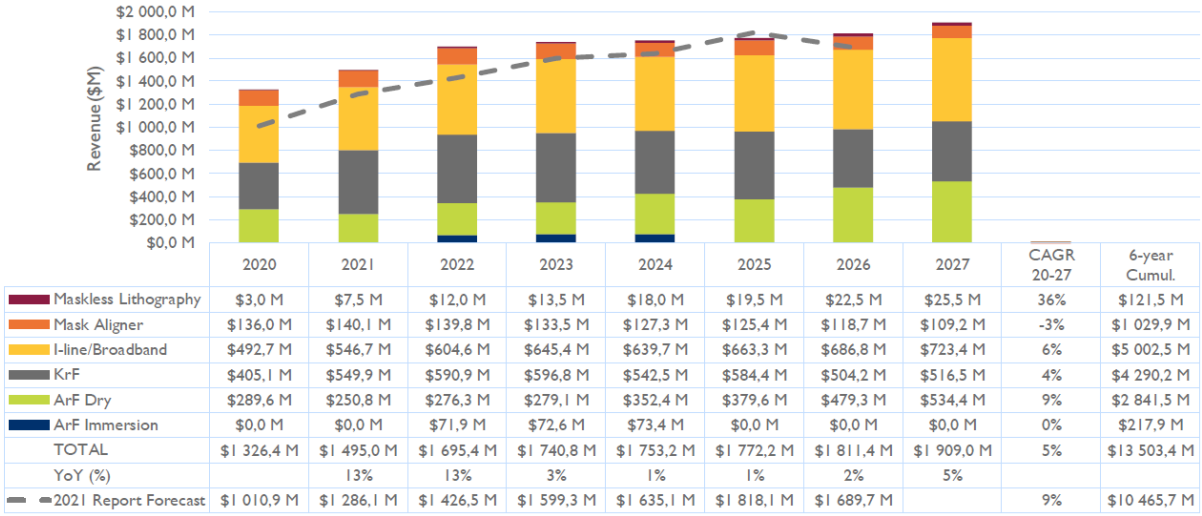

	2020	2021	2022	2023	2024	2025	2026	2027	CAGR 20-27	6-year Cumul.
Maskless Lithography	$3,0 M	$7,5 M	$12,0 M	$13,5 M	$18,0 M	$19,5 M	$22,5 M	$25,5 M	36%	$121,5 M
Mask Aligner	$136,0 M	$140,1 M	$139,8 M	$133,5 M	$127,3 M	$125,4 M	$118,7 M	$109,2 M	-3%	$1 029,9 M
I-line/Broadband	$492,7 M	$546,7 M	$604,6 M	$645,4 M	$639,7 M	$663,3 M	$686,8 M	$723,4 M	6%	$5 002,5 M
KrF	$405,1 M	$549,9 M	$590,9 M	$596,8 M	$542,5 M	$584,4 M	$504,2 M	$516,5 M	4%	$4 290,2 M
ArF Dry	$289,6 M	$250,8 M	$276,3 M	$279,1 M	$352,4 M	$379,6 M	$479,3 M	$534,4 M	9%	$2 841,5 M
ArF Immersion	$0,0 M	$0,0 M	$71,9 M	$72,6 M	$73,4 M	$0,0 M	$0,0 M	$0,0 M	0%	$217,9 M
TOTAL	$1 326,4 M	$1 495,0 M	$1 695,4 M	$1 740,8 M	$1 753,2 M	$1 772,2 M	$1 811,4 M	$1 909,0 M	5%	$13 503,4 M
YoY (%)		13%	13%	3%	1%	1%	2%	5%		
2021 Report Forecast	$1 010,9 M	$1 286,1 M	$1 426,5 M	$1 599,3 M	$1 635,1 M	$1 818,1 M	$1 689,7 M		9%	$10 465,7 M

Figure 3.9: Photolithography equipment market forecast broken down by photolithography technology and by revenue.[89]

An impressive revenue of $13.5B is expected for the lithography equipment shipments only for the More-than-More (MtM) device manufacturing between 2020-2027. Most of the revenue is generated by projection lithography, in particular by i-line systems. Mask aligner revenue will shrink by 3% but will remain far ahead of the maskless lithography with only $121M of cumulated revenue between 2020-2027. The primary challenge of maskless photolithography for mass production seems to be less throughput compared to stepper systems. Despite the higher costs of projection systems, this lithography technology remains method of choice in mass production for the next decade.[89]

Different lithography technologies are available for grayscale lithography. Unique maskless techniques are ready to use in specific markets with low volumes but high resolution with less overlay requirements to modern IC fabrication. The two-photon laser-DWL technology is a promising candidate for rapid prototyping and the precise fabrication of 3D-structures is not limited to silicon substrate. Together with the t-SPL technology, the laser-DWL is suited for NIL mold production, which is still traded as a next-generation lithography technology. Nevertheless, the market forecast for new projection lithography tooling in fabrication sites speak another language in terms of the possibility of mass production. Especially for MtM, the i-line projection lithography will play an important role with growing market share. Fabrication sites probably invest high amounts of money in new front-end technologies (e.g., EUV projection lithography) for the continually shrinking feature size. It is assumed that used UV projection system will be reused in the back-end of line of these fabrication sites, where they could be exploited for grayscale lithography, as well. Manufacturers will calculate critically before investments for new tooling will be spend when older projection systems are ready to use for the production of 3D-structures.

3.3 State-of-the-art positive-tone photoresist lithographic simulation

In 1975, Frederick Dill, together with other authors, formulated the first scientific description of a lithography process via mathematical equations. This group of researchers published their pioneering work in a series of papers, which formed the foundation of modern lithography simulation techniques.[90, 91, 92, 93] The mathematical approach and the developments of the positive-tone photoresist modeling up to date is the primary focus of this section.

During the UV exposure, the resin R, the unexposed sensitizer M, the solvent S and the product of chemical conversion P contribute to the absorption coefficient α. By applying Beer's law, the absorption coefficient follows as[8]

$$\alpha = \alpha_M M + \alpha_P P + \alpha_R R + \alpha_S S, \tag{3.1}$$

where α_M, α_P, α_R and α_S are the absorption coefficients of M, P, R and S. A reduction of the Eq.3.1 follows[8]

$$\alpha = Am + B, \tag{3.2}$$

where A, B and m following the expressions[8]

$$A = (\alpha_M - \alpha_P)\, M_0 \tag{3.3}$$

$$B = \alpha_P M_0 + \alpha_R S + \alpha_S S, \tag{3.4}$$

$$m = M/M_0 \tag{3.5}$$

where M_0 is the initial sensitizer concentration. The vertical local optical intensity $\delta I(z,t)/\delta z$ and the local sensitizer destruction rate $\delta m(z,t)/\delta t$ in the photoresist follows[91]

$$\frac{\delta I(z,t)}{\delta z} = -I(z,t)\,(Am(z,t) + B) \tag{3.6}$$

and

$$\frac{\delta m(z,t)}{\delta t} = -I(z,t)m(z,t)C, \tag{3.7}$$

where C is a measurable sensitivity term. The initial boundary conditions before exposure of the equations Eq.3.6 and Eq.3.7 following

$$m(z,0) = 1 \tag{3.8}$$

$$I(z,0) = I_0 e^{-(A+B)z} \tag{3.9}$$

$$I(0,t) = I_0 \tag{3.10}$$

$$m(0,t) = e^{-I_0 C t} \tag{3.11}$$

The equations Eq.3.6 and Eq.3.7 are solved via numerical integration techniques for $I(z,t)$ and $m(z,t)$ once the Dill parameters A, B, C and initial exposure intensity I_0 is specified.

The factors A and B are referred to as bleachable and non-bleachable absorption coefficients.[91] The term of bleaching describes the loss of absorption capability for UV radiation during exposure. A completely bleached photoresist occurs for $\alpha = B$. The Dill parameters A, B and C are determined through the absorption spectra of a specific photoresist, which is illustrated in Fig.3.10, for a bleached ($t \to \infty$ s) and unbleached ($t = 0$ s) state.

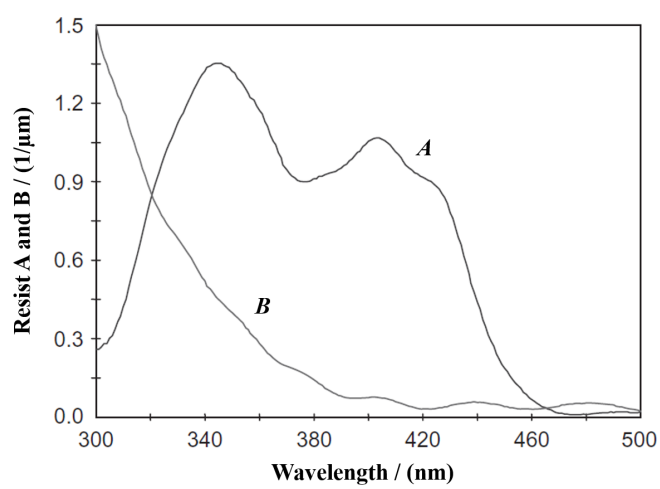

Figure 3.10: Dill parameter A and B as a function of wavelength measured with a UV spectrophotometer for a typical g-line resist.[8]

Calculating unexposed sensitizer concentration is based upon a homogeneous distribution of the PAC in the photoresist film. For thin film thicknesses up to few microns, a homogeneous distribution can be approximated. Thicker resist films need to be split into several thin resist films in which this approximation is valid.

In addition to the simulation of sensitizer conversion for a specific photoresist material and fixed exposure conditions, the development rate for a defined sensitizer concentration has to be determined before the remaining photoresist can be predicted. The optical determination of the development rate for matched substrates is challenging. Karl Konnerth and Frederick Dill specifically built a development cell for in-situ measurements of the photoresist during exposure for this task.[92] The empiric data of the development rate is associated with the calculated unexposed sensitizer (henceforth designated inhibitor, due to the magnitudes of less development rate for unexposed PAC against exposed PAC) concentration for that location in the photoresist film. Consequently, the measured data is fitted to an exponential function and used for the prediction of remaining photoresist after development. Experiments with different softbake temperatures and developer concentrations showed significant variations of the development rate.[91] Thus, process variations or a change of materials lead to new determination of the Dill parameters A, B, C and the development rate.

Dill et al. present a flow chart for the calculation of inhibitor concentration for projection lithography, which is illustrated in Fig.3.11.[93] The simulation flow chart is split into two arms, one for the calculation of the lateral intensity distribution for a given illumination system and the other for the calculation of the vertical exposure distribution within the photoresist film. Thus, inhibitor concentration can be calculated in lateral and vertical directions for a given time step. The model uses a Fourier transform of the object and the modulation transfer function of the illumination system for calculating the spatial frequency distribution, which is transformed via inverse Fourier transformation into the intensity distribution on the photoresist surface. This procedure requires detailed knowledge about the optical properties of the illumination system that is used.

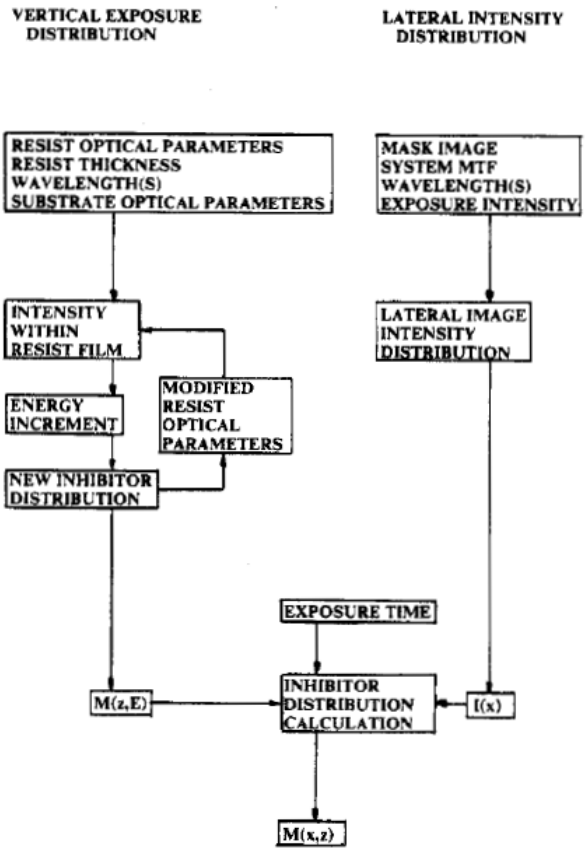

Figure 3.11: Flow chart of inhibitor calculation for projection printing.[93]

The approach of Dill et al. led to the first lithography simulator which is known as "SAMPLE" and it enabled lithography simulation to the community. Researchers in the field could then use the simulation software to understand and improve their lithography processes. Another large name in the lithography community, Chris Mack, introduced the model PROLITH (Positive Resist Optical LITHography model) in 1985. The model enhanced the approach formulated by Dill et al. with an analytical expression for standing wave intensity, a softbake model, a kinetic model for resist development, a model for polychromatic exposure, a kinetic model for exposure reaction and the first model for contact and proximity printing.[94] In 1990, PROLITH/2, the second version of the simulator, was commercially distributed by FINLE Technologies. The software ran on normal personal computers with an easy-to-use interface, which enabled lithography simulation for advanced researchers as well as for manufacturing engineers. With these attributes, the expanded

PROLITH software family is commercially distributed by KLA-Tencor and has continued to advance state-of-the-art method for lithography simulation. A breakdown to the basic working principle of PROLITH is illustrated in Fig.3.12.

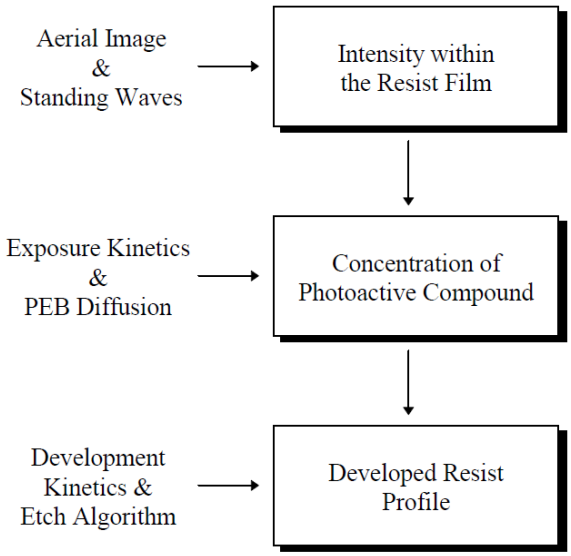

Figure 3.12: Flow chart of the working principle of PROLITH.[95]

Beyond KLA-Tencor, several companies offer lithography simulation programs on similar working principles. However, the software package Dr.LITHO should be identified, in particular. The framework approach provides a research and development-orientated simulation environment.[96] Developed by researchers at the Fraunhofer IISB, Dr.Litho uses the Python script programming language as an integrating platform for different packages developed in C++. This makes the software framework highly adjustable to customer demands and reduces the software costs, as well. The Python script language seems not a very convenient environment for non-programmers but provides the possibility to interface with consumer coding. This possibility is quite useful for simulation studies and optimization tasks, where high amounts of evaluations are often necessary. Beyond the presented approaches, semi-empirical concepts were developed through the use of the contrast curve of a specific photoresist. A few of them a commercially distributed (e.g., the software "GRADED")[73], while others are developed in academic works and often exhibit just limited process windows and do not offer a general procedure for calibration or mask designing.[97, 98, 99]

3.4 Applications for grayscale lithography processes

Grayscale lithography processes are primarily applied in the fabrication of MOE, MEMS, microfluidics but also in semiconductor devices. In this section, for each of these markets, examples of commercial devices, academic research and simulation studies in which grayscale lithography processes play a key role in the fabrication are presented.

High-power semiconductor devices are confronted with high electric fields in the vicinity of the junction termination. The junction depletion etch was first presented in 1976 in order to adjust the shape of the highly doped implant region to improve the breakdown voltage at the p-n junction of the semiconductor device.[100] The similar author published a paper in 1977 with the objective of reshaping the junction termination by the junction termination extension (JTE).[101] Rather than shaping the junction termination via etching, this method exploits a junction extension via implanting, which has several advantages, such as control over the actual dosage charge up to 1% accuracy and added flexibility in the process flow. JTE profiles are often produced via multiple implantation through a modulated checkerboard mask, followed by the diffusion of the implant islands during activation. In SiC-devices, this technique is not applied due to the low diffusivity of the acceptor dopants available for anode termination. In this case, a pure grayscale approach overcomes this issue and was tested with an effectiveness near the ideal breakdown voltage for PiN-diodes.[102] Imhoff et al. used a mask aligner to produce two different photoresist tapered profiles, illustrated in Fig.3.13a and Fig.3.13b, which were covered by carbon subsequently for the use as implantation mask. The exact details about the photomask and the lithographic process are treated as proprietary information. Apart from that, the JTE manufactured by boron ion implantation around an aluminum anode of the PiN-diode showed breakdown voltages up to 6.1 kV and 90% of the ideal parallel-plate breakdown voltage.[102] The grayscale approach enables essential flexibility for the fabrication of power devices, such as silicon carbide PiN, Schottky, and JBS rectifiers, as well as high-voltage silicon carbide thyristors, FETs and bipolar transistors, and is easily applicable to other high-power semiconductor devices in which dopant diffusion is difficult to manage.

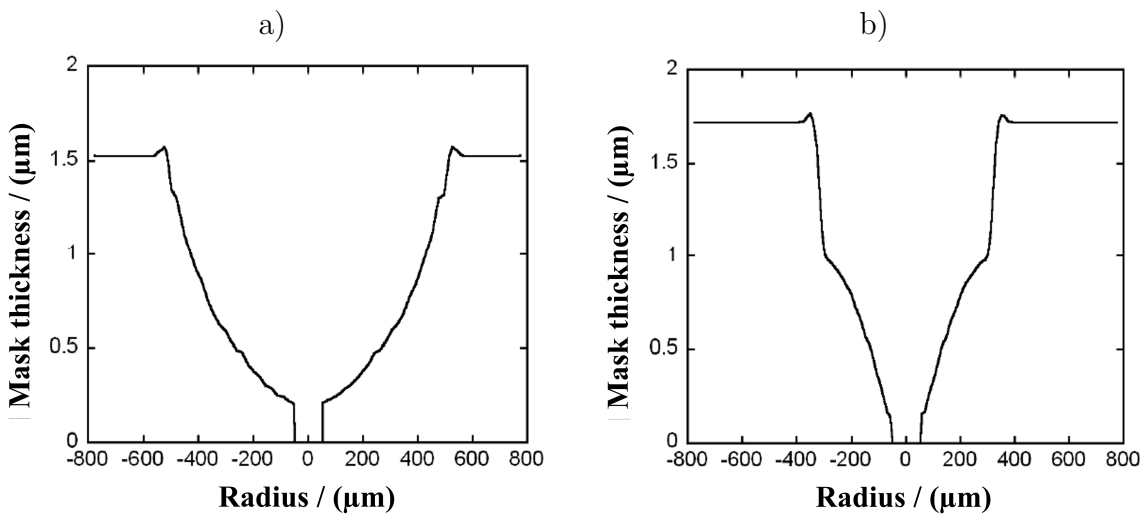

Figure 3.13: Measured carbon profiles of concave taper in a) and convex taper in b) of two different termination widths. The central, mask-free regions are the anodes. The sloped wings result in tapered junction termination extensions around the anodes.[102]

The possibility of doping a semiconductor substrate with sharp 3D-shapes enables the production of unique sensor applications, as presented by Schneider et al.[103] Through the use of TACD simulations, different ion implantation profiles were generated to model distinct semiconductor sensors. Figure 3.14 illustrates the simulated implantation profile of two photodiode anodes in silicon substrate. The stepwise patterned photoresist acts as an implantation mask and is easily fabricable in one grayscale lithography process step. As the wavelength depends upon penetration depth of electromagnetic radiation in the silicon, collecting the photo-generated charge carriers at various depths enables a wavelength-resolved light sensor. A prominent example of this application include ambient-light sensors for optimized color rendering of displays or CMOS and CCD cameras.

The V-shaped doping implantation profile, which is displayed in Fig.3.15, represents a substrate integrated stress sensor. Once the isotropy of the conductivity is broken (as is the case for mechanical stress) the quantity causing the effect can be electrically monitored. Furthermore, this approach enables the fabrication of 3D-Hall sensors for the precise measurement of magnetic fields in the wafer plane.

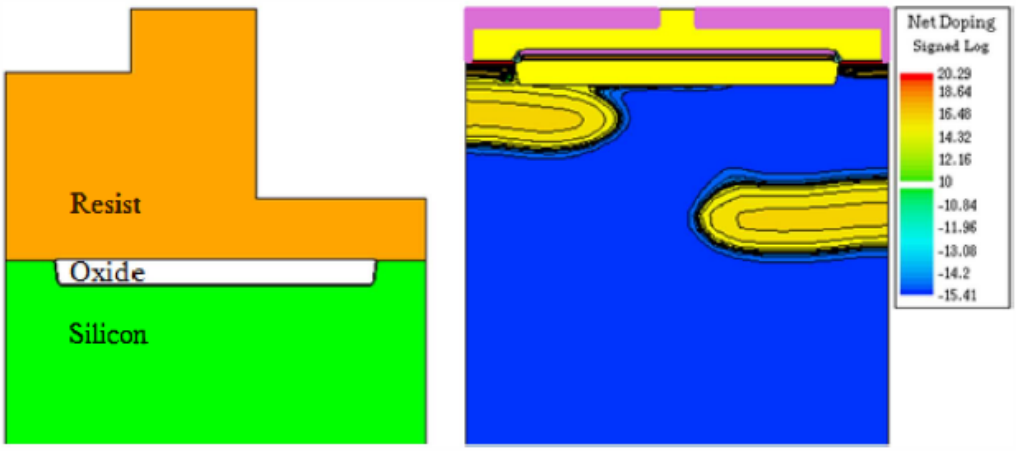

Figure 3.14: TCAD simulation of n-weIIs with varying depth, as they could be used in an optical sensor application.[103]

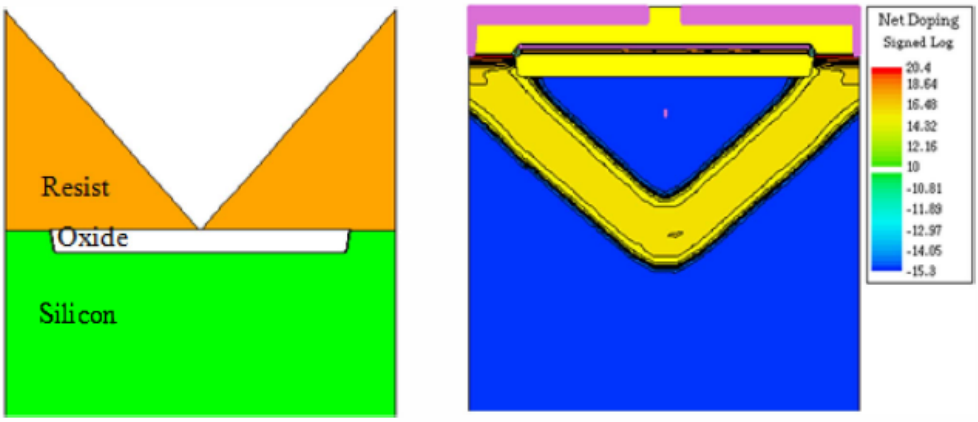

Figure 3.15: Tapered resist profile and resulting net doping in the silicon for the use as stress sensor.[103]

The classic largest field of application for grayscale lithography processes is the fabrication of MOE. Rather than repeatedly presenting the fabrication of Fresnel lenses or blazed gratings, this work focuses on its actual purpose: the fabrication of hyperspectral filter arrays that enable the spectral analysis of images taken from CMOS sensors. The optical filter arrays consist of a set of Fabry-Pérot interferometers that are placed next to each other on top of a CMOS image sensor. The conceptual drawing of a linescan sensor is illustrated in Fig.3.16. Different concepts of filter arrangements are available with distinct filter band

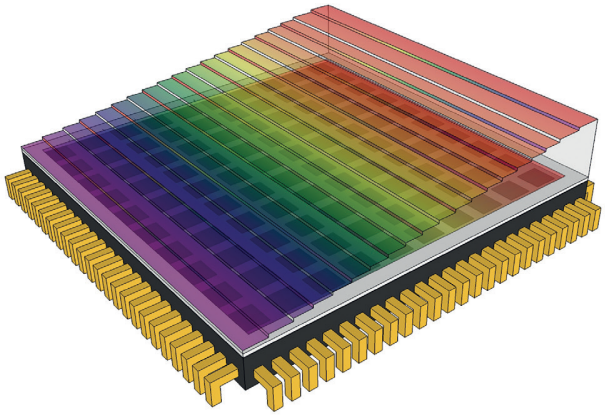

Figure 3.16: Conceptual drawing of hyperspectral linescan imager with 100 static spectral filter structures.[104]

amounts. These filter arrays are efficiently producible via a grayscale lithography process, where a transparent insulator, enclosed between two semi-permeable mirrors, is structured with up to more than 100 thickness steps in a spectral range from UV-VIS-NIR.[105, 106]. The CMOS-compatible optical filter arrays overcome the bulky and expensive systems of classical spectrometry methods. Target markets for hyperspectral imaging cameras include agriculture monitoring, food monitoring, life sciences, mineral exploration and the analysis of drill cores and mining samples.[107, 108] The transmission efficiency of commercially available systems reaches 85% with an full-width half maximum of 10 nm for collimated light.[106]

MEMS resonators have gained significant attention in applications, such as gyroscopes[109], electrostatic field sensors[110] or as narrow bandpass filters.[111] Due to their large travel range and lower damping, in-plane resonators are used for these applications. Comb-drives demonstrated the tunability over large amplitudes, which makes them preferable for these applications. However, this resonator principle requires large area for single comb-pairs, which reduces finger density and the overall electrostatic spring strength. The vertical structuring of the comp-resonator fingers enables the fabrication of electrostatic springs without increasing the device area. Figure 3.17 illustrates three distinct finger designs with stiffening and weakening electrostatic force during finger engagement. Experiments in which the

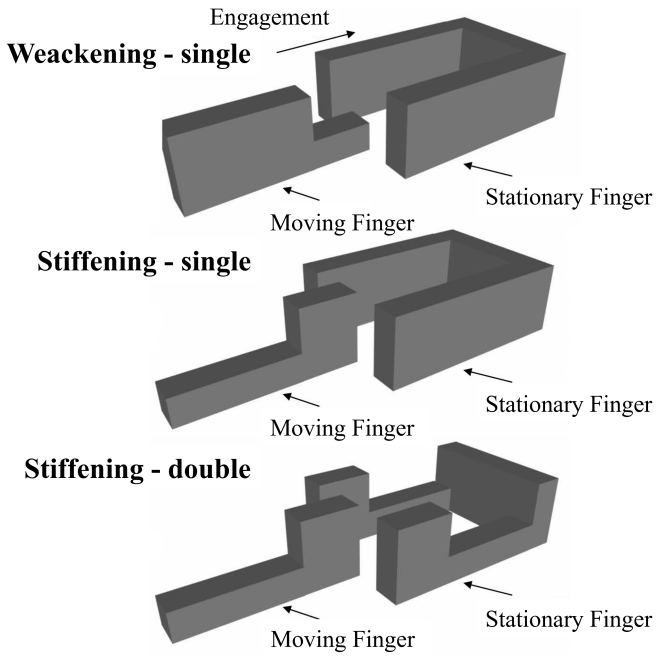

Figure 3.17: Vertically shaped comb-resonator designs of a single comb-pair with a weakening electrostatic spring that leads to lower resonant frequencies and stiffening electrostatic springs that lead to higher resonant frequencies.[112]

comp-fingers were structured in a single step via projection grayscale lithography show spring constants of up to 1.45 N/m at 120 V with the capability of bidirectional resonant frequency tuning of 17% without increasing the device size.[112] Moreover, multilevel 3D-structured comb-fingers and suspensions enable lower driving voltages.[113]

The ability of micro 3D-structuring has led to impressive fabrications in the field of microfluidic devices. DWL technologies, in particular, are used to manufacture arbitrary shapes for micro-mixers[114, 115], circular microfluidic channels[116], micro-needles[117] or micro-wavy patterns on substrate surfaces[118] and will lead to more novel device approaches in the field. In this section, just a few of the latest achievements are presented. Figure 3.18 shows a 3D mixing element (3DME) printed in SU-8 photoresist by two-photon polimerization. The construction enhances the quality of mixing and the possibility of optical inspection

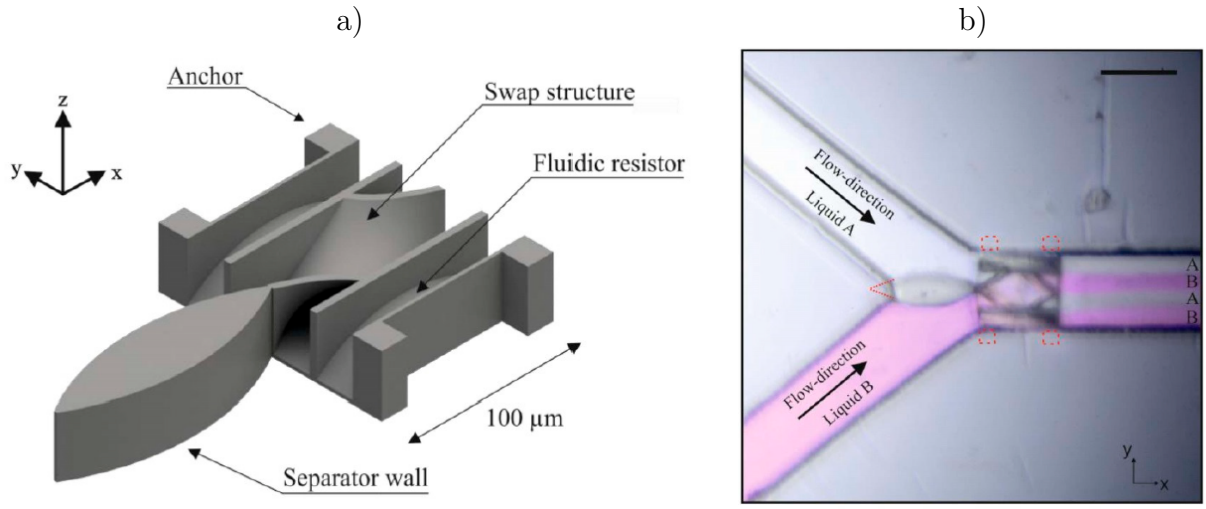

Figure 3.18: CAD rendering of the 3DME in a) shows a cut along the xy-plane to show the swap-element and fluidic resistors. The microscopy image in b) shows the functionality of the 3DME for de-ionized water (liquid A) and de-ionized water stained with Rhodamine B (liquid B).[114]

by the vertical alignment of the mixed liquids. In principle, microfluidic applications do not require high-class cleanroom environments for the fabrication. In this regard, He et al. demonstrated a cost-efficient method for producing micro-waves onto a polymer (PDMS) substrate.[118] To demonstrate the capabilities of a projection system that is based on a digital micro-mirror device (DMD), they produced several wavy substrates with wavelengths of 21-2100 µm with an amplitude-to-wavelength ratio up to 300%. The purpose of the device, illustrated in Fig.3.19, is to capture circulating tumor cells (CTCs) for detection. In the test, HCT-116 cells were selected as target cells with good results. During the Covid-19 pandemic, knowledge about possible vaccination techniques grew rapidly. Thus, the approach of

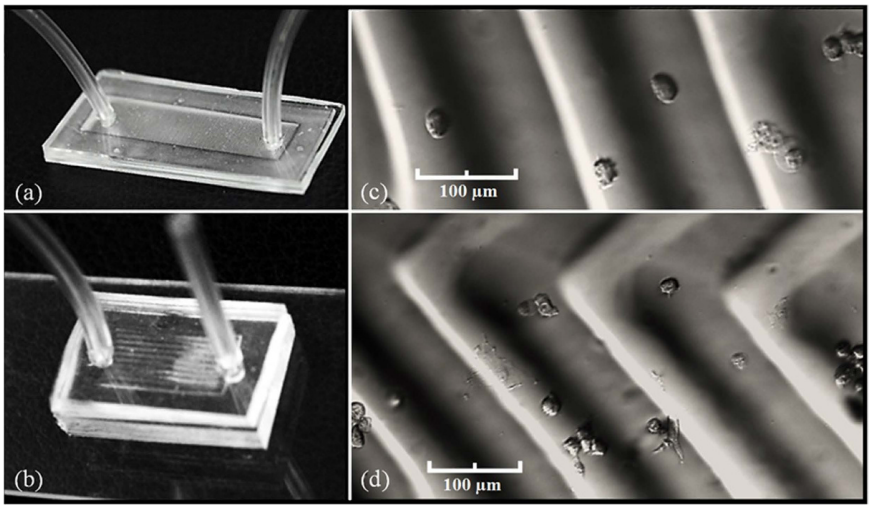

Figure 3.19: Microfluidic devices for the detection of tumor cells with pure wavy pattern in (a) with captured CTCs in (c) and wavy-herringbone pattern in (b) with captured CTCs in (d).[118]

Balmert et al. is not surprising for using a micro-needle array fabricated via 3D laser lithography for vaccination. The micro-needle array, which is illustrated in Fig.3.20, is composed of needles that feature pyramidal heads supported by undercut stem regions with filleted bases to ensure successful skin penetration and retention during application. The cutaneous vaccination elicited more antigen-specific cellular humoral immune response than traditional intramuscular injection. The enhanced immune response may reduce the amount of antigen needed, lowering the risk of both toxicity and cost.[117]

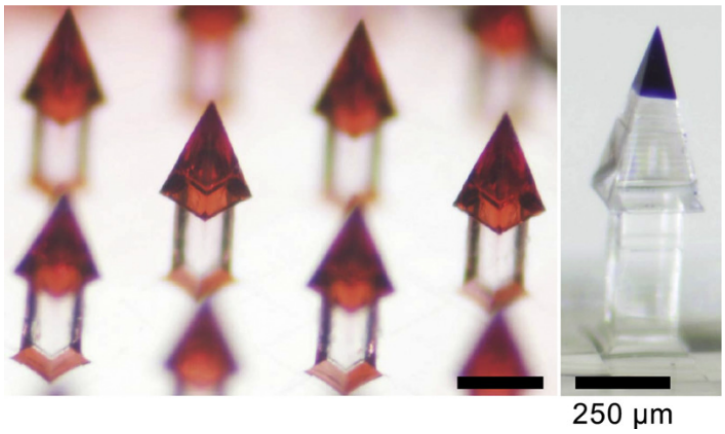

Figure 3.20: Tip-loaded CMC/trehalose micro-needle array integrating Allura Red R40 dye at the pyramid region of the micro-needles.[117]

CHAPTER 4

The three-state lithography model

In this chapter, the three-state-lithography model (TSLM) is developed from a mathematical perspective for positive-tone photoresists. The mathematical approach consists of several parameters that must be determined before the TSLM can be applied for the design of a photomask to pattern 3D-structures in a photoresist. The parameter definition procedure is described in detail and a mathematical method for the optimization of the TSLM parameters is presented. The model is validated with a Fourier analysis of the areal image and certain test structures produced with the use of the TSLM.

For the experimental procedure, we utilize a postive AZ ECI 3027 photoresist for all test processes and the pyramidal, spherical, and chess field sample structures. Operating on a Suess Gamma spin coating and development system, resist thicknesses of 3 µm were coated on 200 mm silicon substrates. The UV exposures were performed using a Canon FPA-3000 i4 stepper with an i-line illumination system, a numerical aperture $NA = 0.63$, and an object-to-image reduction ratio $M = 5{:}1$. No post-exposure bakes were executed before development in AZ 726 MIF. Thickness measurements of the contrast curve were carried out using a KLA-Tencor UV1280. Microscopy images are captured with a Reichert-Jung Polyvar SC.

4.1 Mathematical approach

The photoresist simulation with the three-state lithography model bases on the precise knowledge of the contrast function for a given resist and developer combination. This function or contrast curve includes specific process parameters, such as the optical absorption and

reflection properties of the substrate, as well as applied soft-bake and development process parameters. Exemplary shapes of contrast functions for an ideal and realistic photoresist are displayed in Fig.4.1. A contrast curve follows the border where a photoresist turns its

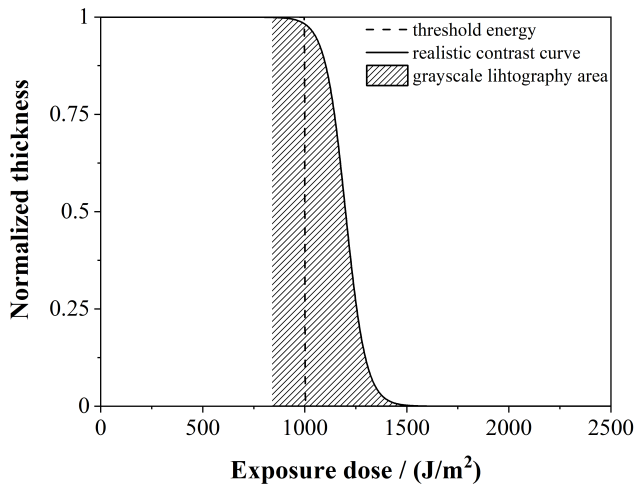

Figure 4.1: Shapes of contrast curves for an ideal and realistic photoresist.

solubility in developer medium depending upon the exposure dose. An ideal photoresist shows an infinite high contrast at the threshold exposure energy. Over the threshold dose, the photoresist becomes entirely soluble in the developer medium. However, real photoresists show limited contrast, which make them usable for grayscale lithography. The higher the contrast of the photoresist, the smaller the area applicable for grayscale lithography. The contrast curve shape follows the mathematical expression of a sigmoid function (henceforth designated s-function). To model an asymmetric course of the contrast curve that is caused from the resist's inner light absorption, the s-function is weighted with Lambert's law from Eq.2.4, using the boundary condition of a constant absorption coefficient α during exposure.

As a result, the mathematical expression for the contrast curve can be written as[119]

$$T = \frac{D_0}{1 + e^{\left(a \ E \ e^{-\alpha(D_0 - T)} + b\right)}} \ , \tag{4.1}$$

where a and b are parameters extracted from measurement data and D_0 represents the initial resist thickness.

As presented in the work of Wagner et al.[71], rectangular sub-resolution mask patterns with a width D_x and length D_y, separated through a constant pitch p, can be applied to

alter the intensity distribution in the areal image. From these parameters, a fill factor GS for mask features is expressed as[119]

$$GS = \frac{D_x D_y}{p^2} \,. \tag{4.2}$$

Considering the optical Rayleigh resolution limit (Eq.2.3) with $k_1 = 0.61$, the pitch p is set to 300 nm for the i-line projection system that is used. The physical basis of intensity variations for specific mask features is a limited entrance pupil of the projection system, which acts as an optical low-pass filter. The Fourier plane in a Köhler illumination system is located in the entrance pupil position[8]. Given ray optics, the object-sided opening angle θ can be given as[119]

$$\theta = \frac{2NA}{M} \,, \tag{4.3}$$

where NA is the numerical aperture and M represents the reduction ratio. The mathematical treatment of the intensity distribution is derived from the theory of Fraunhofer diffraction (Eq.2.1) and describes the propagation of an incident plane wave on a lattice in the far field. For a two-dimensional quadratic aperture, the intensity I_d of the diffraction pattern is proportional to[119]

$$I_d \propto (D_x D_y)^2 \left(\frac{\sin(D_x \frac{\pi}{\lambda} \sin(\alpha))}{D_x \frac{\pi}{\lambda} \sin(\alpha)} \right)^2 \left(\frac{\sin(D_y \frac{\pi}{\lambda} \sin(\beta))}{D_y \frac{\pi}{\lambda} \sin(\beta)} \right)^2 \,, \tag{4.4}$$

where α and β represent the angular divergence of the diffracted light in x and y direction and λ is the illumination wavelength. For a squared-entrance pupil geometry, the two-dimensional integral of Eq.4.4 over the angles of divergence determines the intensity in the aerial image plane, and is expressed as[119]

$$I_i \propto \frac{2}{\pi} (D_x D_y)^2 \int_0^{\theta/2} \int_0^{\theta/2} I_d(\alpha, \beta) \; d\alpha \, d\beta \,, \tag{4.5}$$

where $\theta/2$ acts as spatial cut-off frequency of the optical low-pass filter. The impact of altering intensities on the contrast curve in Eq.4.1 can be considered by k_F (henceforth designated Fourier factor), which includes the contribution of accessible intensity propagating

through the entrance pupil. The Fourier factor is expressed using Eq.4.2 as[119]

$$k_F = GS^2 \left(\frac{2k_x \ Si\left(2k_x\right) + cos\left(2k_x\right) - 1}{\pi k_x} \right) \left(\frac{2k_y \ Si\left(2k_y\right) + cos\left(2k_y\right) - 1}{\pi k_y} \right) , \tag{4.6}$$

where $k_x = \pi D_x sin\left(\alpha\right)/\lambda$ and $k_y = \pi D_y sin\left(\beta\right)/\lambda$ and the expression $Si()$ represents the sine integral. By multiplying Eq.4.6 with the exposure dose E in Eq.4.1, the contrast curve for individual GS is described via the expression[119]

$$T = \frac{D_0}{1 + e^{\left(a \ k_F \ E \ e^{-\alpha(D_0 - T)} + b\right)}} . \tag{4.7}$$

A closer examination on Eq.4.6 reveals that the transmitted light is not merely proportional to the squared fill factor, but also dependent upon the transmitted wavelength, system entrance pupil, and pattern size. The part of illumination passing the entrance pupil of the optical system applied in this work is illustrated in Fig.4.2 and is dependent on the size of the mask features. To ensure the Fourier factor is dependent just on the fill factor, mask features

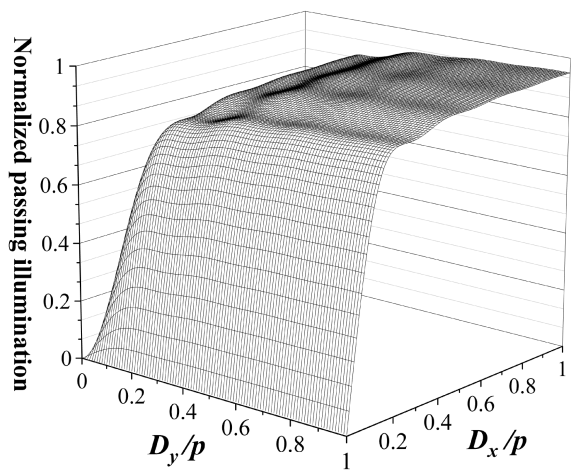

Figure 4.2: Contribution of diffraction to k_F in dependence on the standardized mask pattern dimensions D_x/p and D_y/p.[119]

are limited to quadratic shapes. This limitation provides the additional benefit of lowering the calculation efforts required for the model. In this case, k_F becomes one-dimensional. The course of k_F for quadratic mask features compared to a simple quadratic dependency is displayed in Fig.4.3.

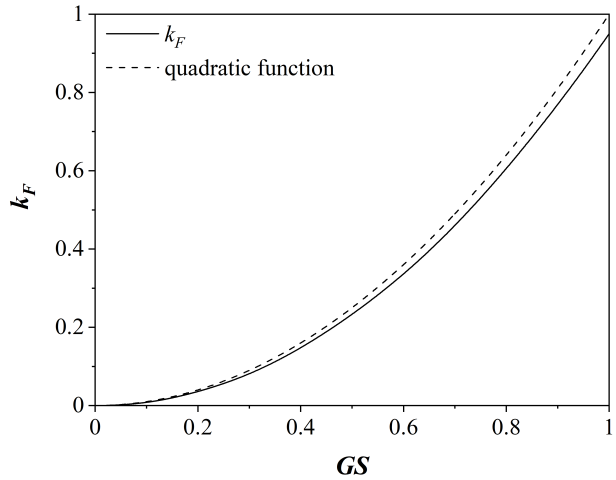

Figure 4.3: Fourier factor k_F for quadratic mask pattern compared to the quadratic function $k_F = GS^2$.[119]

As a consequence of lower intensities for narrower mask patterns, the threshold for chemical transformation in the resist shifts to higher energy doses. This altered threshold E_{shift} is dependent upon GS and is added to the initial threshold energy dose E in Eq.4.1 with respect to the expression[119]

$$E_{shift} = -c\ ln(GS)e^{-d\ GS}\ , \tag{4.8}$$

where c and d represent characteristic parameters for each type of photoresist. These parameters are empirically determined by exposing a test mask to a variable exposure dose.

During exposure, the optical properties of the positive photoresist change due to the chemical formation of carboxylic acid. The chemical conversion, which primarily impacts the extinction coefficient, causes the photoresist to appear transparent to UV radiation. This effect, which is known as bleaching, is strongly dependent upon the chemical compounds of the photoresist and affects the slope of the contrast curve individually for any mask pattern fill factor. For a good approximation, the soluble photoresist component near the resist-developer surface is modeled by utilizing Eq.4.1 and Eq.4.8, without taking Lambert-Beer into account. The solubility of deeper-lying material within the photoresist follows Eq.4.7. To create a continuous transition between shallow and deep photoresist solubilities, an intermediate phase is mathematically expressed via a spline-interpolation function and is

defined individually, depending on the fill factor. Thus, the TSLM follows the sectionally-defined expression[119]

$$E = \begin{cases} \dfrac{ln\,(D_0/T-1)+b}{a} - E_{shift} & T > P_1 & \text{(I)} \\ eT^3 + fT^2 + gT + h & T < P_1 \wedge T > P_2 & \text{(II)} \\ \dfrac{ln\,(D_0/T-1)+b}{a\ k_F\ e^{-\alpha(D_0-T)}} & T \leq P_2 & \text{(III)} \end{cases}, \tag{4.9}$$

where the boundary points P_1 and P_2 represent the intersections between the distinct phases. The symbols e, f, g, and h operate as fit parameters for the spline function. To decrease the complexity of calculation, the implicit expressions in Eq.4.1 and Eq.4.7 are expressed in their explicit forms in Eq.4.9, depending upon the photoresist thickness T.

4.2 Determination of model parameter

To execute of the TSLM, the free parameters of Eq.4.9 must be defined for fixed optical properties of the layer stack and illumination system. Every change of materials or process tools leads to a new definition of the parameters of the TSLM. The procedure of the parameter definition involves five steps listed in Tab.4.1 and discussed later on.

Table 4.1: Procedure of the parameter definition.[119]

Step	**Operation**	**Materials**
1	Exposure experiment	1st test wafer
2	Dose correction	
3	Test mask experiment	Test mask & 2nd test wafer
4	Parameter determination	
5	Parameter optimization	

Step 1: Exposure experiment

In order to determine the parameter a and b of Eq.4.9(I) and Eq.4.9(III), a test wafer with optical properties similar to the fabrication substrates is illuminated to a set of exposure doses. Measurements of remaining photoresist following development for each exposure dose are displayed in Fig.4.4 and determine the contrast curve shape for GS = 1. The measurement data is derived from a set of six measurement sites across the wafer with similar exposure doses; the error is calculated from the standard deviation of the mean of a data set.

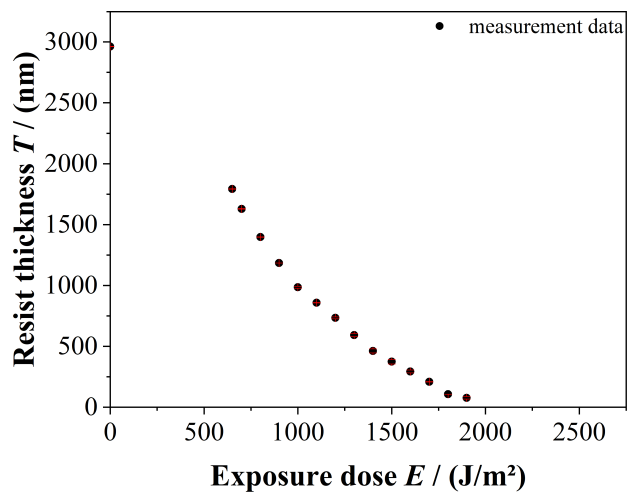

Figure 4.4: Measurement data from the exposure experiment

Step 2: Dose correction

Due to the absorption of UV radiation in the resist film, the preset exposure doses from step 1 must be corrected. For this correction, Lambert's law (Eq.2.4) is applied with an absorption coefficient for an unbleached photoresist. With $\kappa = 0.0202$[120] for the used photoresist and Eq.2.5 the absorption coefficient results to 0.7 1/µm. This approximation is only valid for exposure times smaller than the reaction time of the photoresist up to the tens of milliseconds.[121] It should be mentioned that the absorption coefficient in this example is adjusted to 0.52 1/µm. This is necessary when exposure times are longer than the approximation of a static absorption coefficient allows for. Figure 4.5 shows the corrected

data and the fit function following Eq.4.9(I) for $E_{shift} = 0$. Table 4.2 lists the fit parameters from the corrected data.

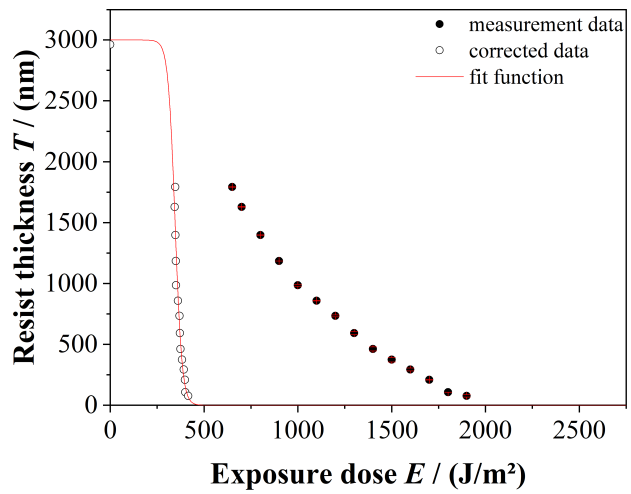

Figure 4.5: Corrected data and fit function from the dose correction

Table 4.2: Fit parameters of 4.9(I) for the dose corrected data. D_0 is fixed at 3000 nm.

D_0 / (nm)	3000±0
a / (m^2/J)	0.05377±0.01997
b	18.56977±6.93707
R^2_{cor}	0.96839

Step 3: Test mask experiment

A test mask is used to determine the variables k_F, c, and d. An exemplary chip design for the test experiment used in the present work is illustrated in Fig.4.6. This figure contains squared fields with side lengths of 540 µm, consisting of quadratic shapes with a pitch of 300 nm and fill factors from 0.04 to 1. For $GS > 0.48$, the quadratic shapes are altered from window to wire design based upon babynet's principle.[2] Moreover, the influence of neighbored structures on specific GS can be found by the investigation of stitched lines of 3.57 mm length and 540 µm width in different ambient conditions with varied open areas.

The results lead to an optical proximity correction (OPC).[8] A second test wafer as in step 1 is fabricated and illuminated again with a set of different exposure doses. Measurements of remaining resist for each exposure dose determine the contrast curve shape for each GS.

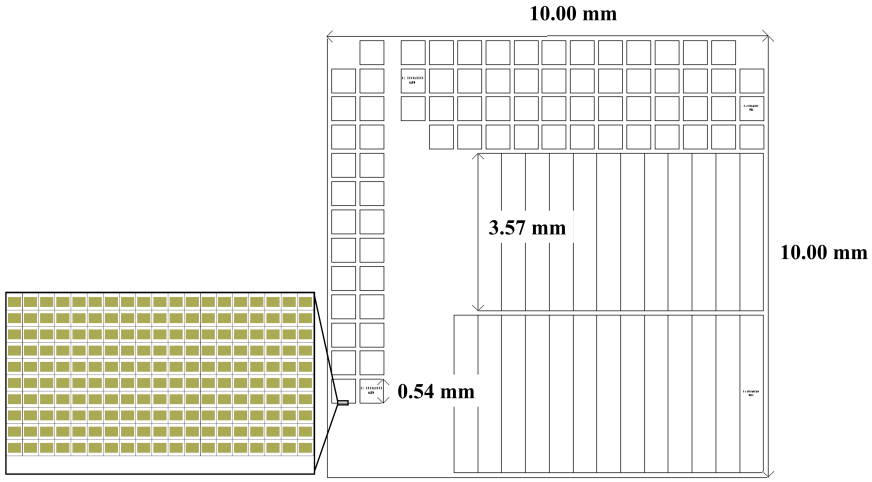

Figure 4.6: Chip design of the test mask experiment.

Step 4: Parameter determination

For the definition of k_F, only measurements with exponential decay for each GS are used for the fit to Eq.4.9(III). The data cut-off for the fit must be done manually. To define of E_{shift}, the threshold exposure doses for every GS are graphically examined. The threshold exposures are observable at the energy levels where resist begins to solve in developer. These values are fitted to Eq.4.8 to determine the variables c and d. The parameters of Eq.4.9(II) are determined by the solution of the undefined system of equations

$$dE_1 = eP_1^2 + 2fP_1 + g \tag{4.10}$$

$$dE_2 = 3eP_2^2 + 2fP_2 + g \tag{4.11}$$

$$E_1 = eP_1^3 + fP_1^2 + gP_1 + h \tag{4.12}$$

$$E_2 = eP_2^3 + fP_2^2 + gP_2 + h, \tag{4.13}$$

where P_1 is set to 2950 nm in this work and P_2 varies depending on GS via the expression $P_2 = 2$ (Eq.4.9(I) $\cap$ Eq.4.9(II)). Iterative solutions for e, f, g, and h are calculated for

distinct GS until a preset thickness error of simulated remaining resist is reached. Figure 4.7 illustrates simulated contrast curves for AZ ECI 3027 photoresist and measurements of remaining photoresist after development for different exposures and GS.

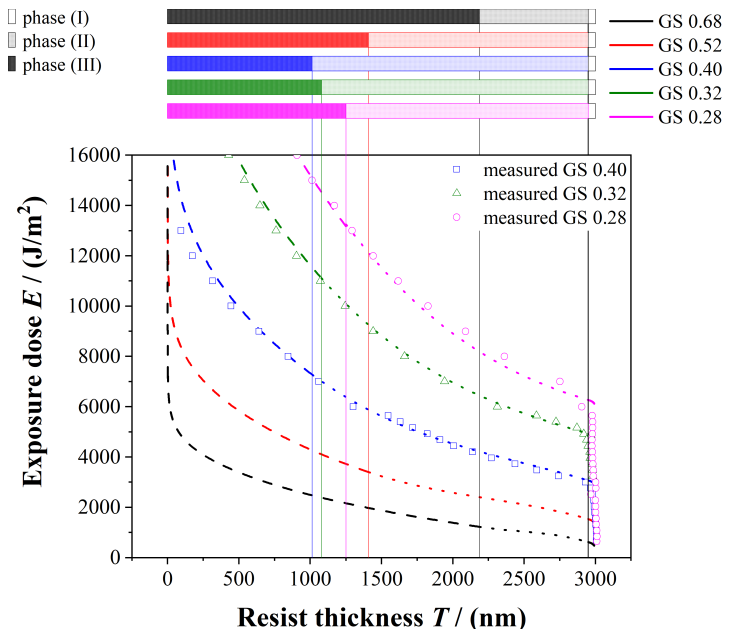

Figure 4.7: Contrast curves for photoresist on bare silicon for the fill factors $GS = 0.28$, 0.32, 0.40, 0.52, 0.68 calculated via the three-state lithography model in comparison to sample measurements of the resist thickness produced with a test mask. Straight lines correspond to Eq.4.9(I), dotted lines corresponding to Eq.4.9(II) and dashed lines to Eq.4.9(III).[119]

4.3 Parameter optimization

With the completion of step 4, all of the relevant parameters for the use of the TSLM have defined. A subsequent optimization of the determined values is performed in order to minimize the prediction errors of the model. To optimize parameters, Eq.4.9(I) and Eq.4.9(III) are suitable. Variables of Eq.4.9(II) are recalculated in an iterative manner for a preset thickness error limit. By lowering this error limit, the parameters of the spline function automatically increase their accuracy. For Eq.4.9(I) and Eq.4.9(III), the parameters a, b,

k_F, and the parameters c and d of E_{shift} are optimized via statistical evaluation of the error between the simulated contrast curve and measurements of the remaining resist for different GS. The fit values for all of the parameters are determined on several fabricated test wafers. The standard deviations of the mean values examine the statistical optimum for each parameter. This procedure can be done for several values of P_1 and P_2 to find the minimum error figure. Due to the amount of calculations involved in the optimization, step 5 is excluded from the TSLM source code in order to guarantee integration in standard layout software tools with limited programming possibilities.

4.4 Fourier analysis of the areal image

In the TSLM, the contribution of accessible intensity passing the entrance pupil of the illumination system is expressed via the Fourier factor k_F. This factor is based upon the object-sided opening angle θ (Eq.4.3) and acts as a cut-off frequency in Eq.4.5. Thus, k_F can be calculated for a single fill factor GS in an analytic manner. Simulations of the spatial filtering are applied to validate the analytically computed Fourier factors. To this end, a fast Fourier transformation (FFT) method is applied to calculate the Fourier image in the entrance pupil of the illumination system. The resulting Fourier image is manipulated by a squared low-pass filter with a cut-off frequency of $\theta/2$ and subsequently reverse-transformed. The produced intensity distribution of the spatial filtered image is used for the validation of analytically calculated Fourier factors k_F and compared to the intensity attenuation for measurement data.

A discrete, 2D-array, exemplary displayed for a fill factor $GS = 0.24$ in Fig.4.8, is prepared with 50x50 varying openings in pitch $p = 1.5$ µm which operates as photomask in the simulations. The resulting image following spatial filtering is illustrated in Fig.4.10. The Fourier transformation of the photomask in the entrance pupil of the illumination system with a numerical aperture $NA = 0.63$ is displayed in Fig.4.9. For evaluation, data from the test mask experiment of step 4 in Sec.4.2 are exploited for comparison with the simulation data. Thus, a set of simulations with similar fill factors to the test mask experiment is

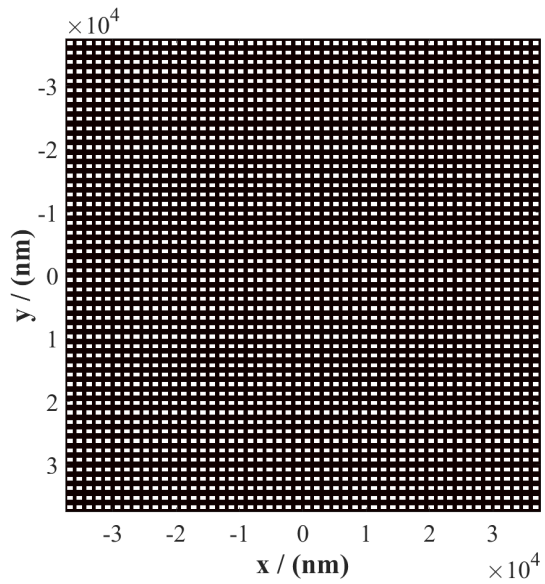

Figure 4.8: Exemplary photomask in the simulations of the Fourier analysis with squared fields acting as photomask openings in a size of 900x600 nm.

computed and the decrease in intensity in the areal image after spatial filtering is observed. The attenuation correlates to the Fourier factor k_F and is expressed by the ratio of intensity in the areal image to the incident illumination intensity. The intensity reduction is determined via the mean of the normalized intensity field in Fig.4.10. Cross-sections in the center and quarter in the y-plane of the areal image, displayed in Fig.4.11, enable the investigation of intensity homogeneity. Relevant variations of intensity particular occur in an area of approx. 10 µm at the structure edges. Variations in the structure center lead to a observable ripple on the photoresist surface, albeit without significant impact on the structure geometry.

The comparison of simulated, measured, and analytically determined Fourier factors k_F is shown in Fig.4.12. In the case of measurements out of the test mask experiment, the attenuation of intensity in the areal image is determined by the ratio of exposures needed for a certain resist thickness for the contrast curve of $GS = 1$ and the exposure dose set at the illumination tool. The simulated, measured, and analytically calculated data match well in an area of $GS = 0.36 - 0.48$. Measurement data above $GS = 0.48$ show larger errors compared to the simulated and analytic data sets. It is assumed that an insufficient photomask writing

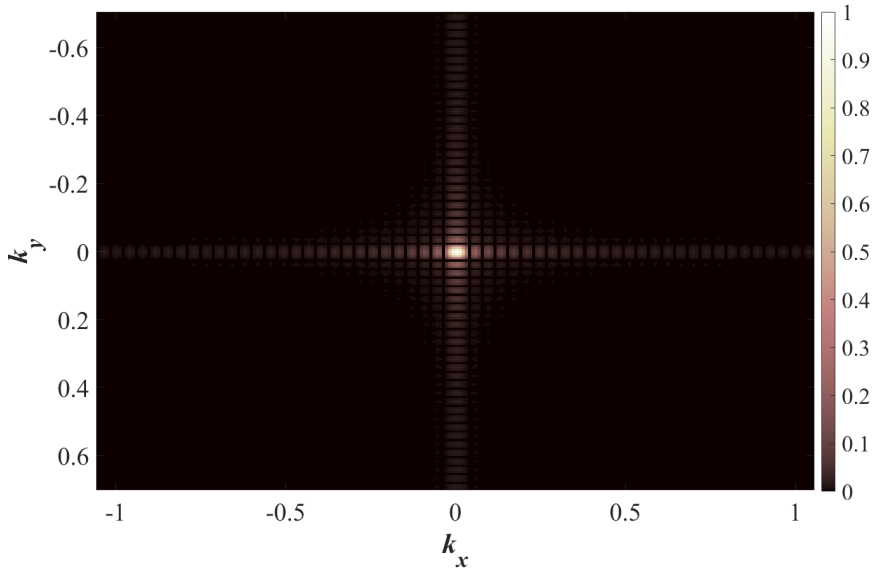

Figure 4.9: Simulated Fourier transformation of the photomask pattern in Fig.4.8 with normalized intensity distribution.

process leads to the overexposed areal image. Figure 4.13 shows a micorscopy image of a test field containing grayscale fill factors of $GS = 0.56$. The pinkish squares with a 50 µm base length of the remaining resist are spread equidistant in 1 µm to each other across the test field. Due to the pattern regularity, the assumption is that the error comes from the spatial filtering of slightly misaligned mask patterns. Due to the larger error of the wired design of mask patterns above fill factors of $GS = 0.48$, all subsequent photomask layouts of the present work are based on the window shaped design for grayscales.

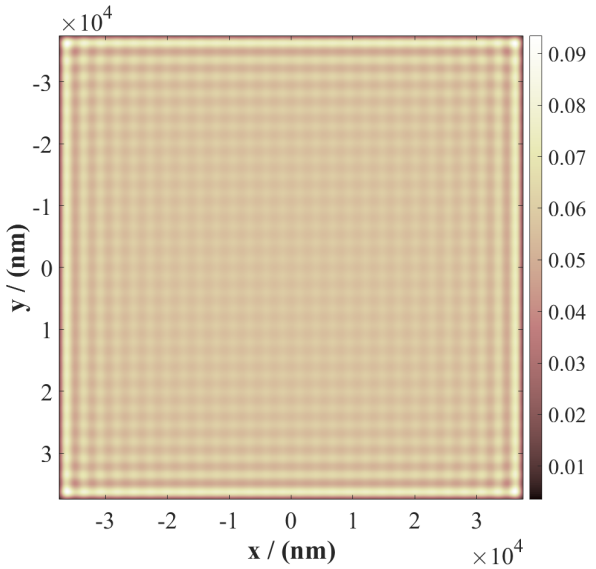

Figure 4.10: Simulated image of the photomask pattern after spatial filtering. The scale of intensity is normalized to the incident intensity.

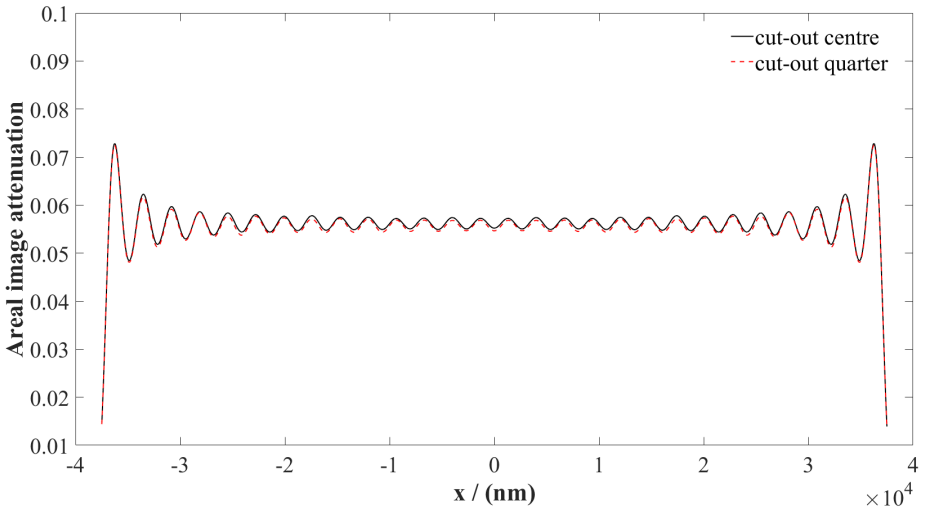

Figure 4.11: Cross-sections of the simulated areal image after spatial filtering in the center and quarter of the y-plane of Fig.4.10.

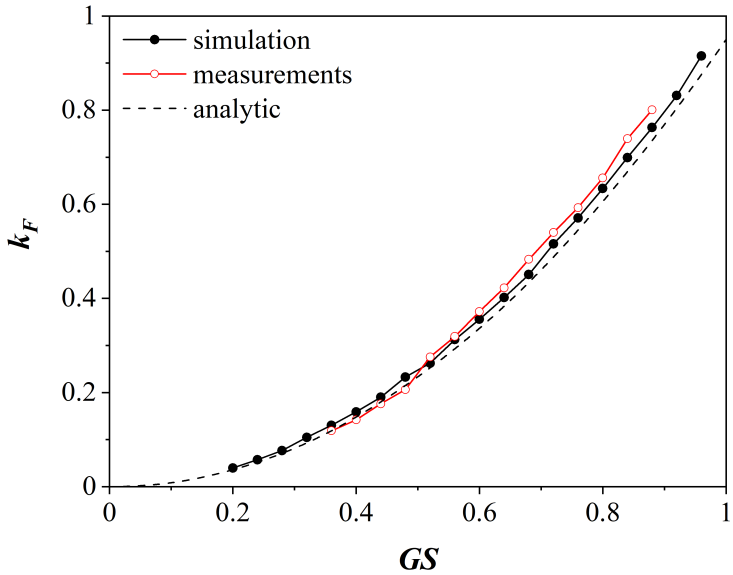

Figure 4.12: Comparison of simulated, measured and analytically determined attenuation of the intensity in the areal image.

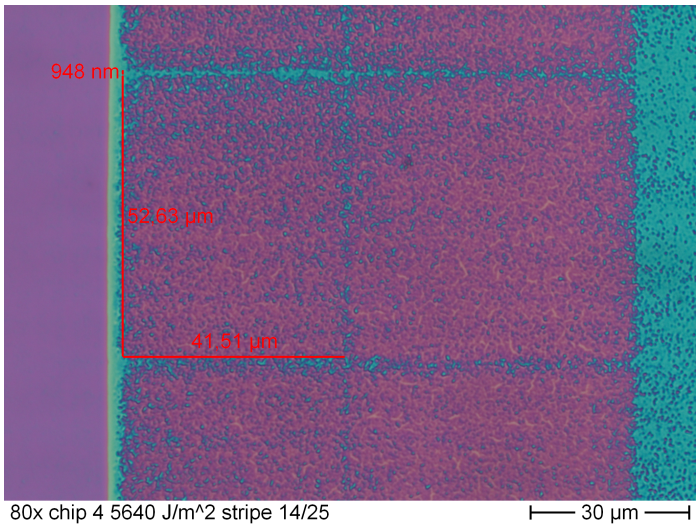

Figure 4.13: Microscopy image of a grayscale test field with a wire shaped grayscale design for a fill factor $GS = 0.56$.

CHAPTER 5

Process optimization and fabrication of test structures

In this chapter, the postive-tone AZ ECI 3027 photoresist is again utilized for all of the experiments as well as the fabrication of 3D-structures. Photoresist coating, exposure and development process are performed with equipment similar to that as in Chapter 4 for the puddle development experiments. Development experiments for spray development are executed on a EVG 150 coating and development tool. The development of the test structures are either completed via dip development or spray development on a Suess Gamma with transferred process parameters from the EVG 150. To flatten the resist irregularities on the pyramidal resist structures, a subsequent hardbake at 115° C was performed for 120 s. Spray development is used in experiments with anti-reflective coatings using AZ BARLi II for BARC and AZ Aquatar VIII A45 for TARC on a Suess Gamma. A Suess ACS is used for the spin coating process of the anti-reflective layers. Thickness measurements were carried out using a KLA-Tencor UV1280. The resultant pyramidal and chess field structures were investigated via KLA Tencor P-17 Stylus Profiler, while the spherical structures are inspected with a Digital Instruments Dimension 5000 Atomic Force Microscope system. Microscopy pictures are captured with a Reichert-Jung Polyvar SC.

5.1 Optimization of the development uniformity

Process optimization is a significant task during the fabrication of 3D-topographies in photoresist. The process optimization in the present work is targeted not only at high fabrication yield and structure accuracy, but also at the minimization of used materials and media. The process optimization is based upon the standard resist coating and development process used

at the Fraunhofer EMFT for 3 µm photoresist films in the CMOS fabrication.

The optimization procedure is executed on a stepper job design, which is illustrated in Fig.5.1, with a blank photomask on the reticle stage in order to consider the absorption of incident light in the glass substrate. The stepper layout is comprised of exposure fields in the size of 5x5 mm, separated in a pitch of 7 mm. A variation of exposure doses from top to bottom in a test field of 20x20 chip dices is used in the test processes. After replacing the UV source in the illumination tool, the experiment's minimal exposure dose was fixed at 650 J/m^2 due to an increased source intensity and limited shutter opening times. For

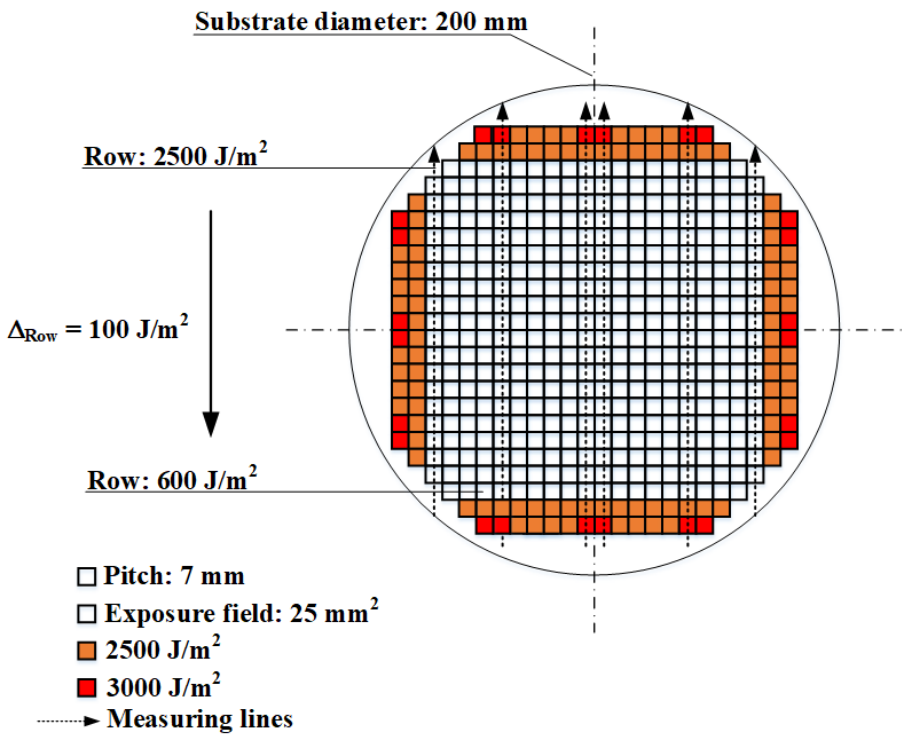

Figure 5.1: Stepper job design used for the process development and optimization.

the measurement of photoresist uniformity across the substrate, six columns of the test field that are optically evaluated in the chip center and shown in Fig.5.2-Fig.5.4. Photoresist homogeneity in specific exposure fields are illustrated in Fig.5.5a-Fig.5.5f. Both investigations are performed for several puddle and spray development processes. The influence of the developer concentration and the exposure dose to the development rate is shown in Fig.5.6.

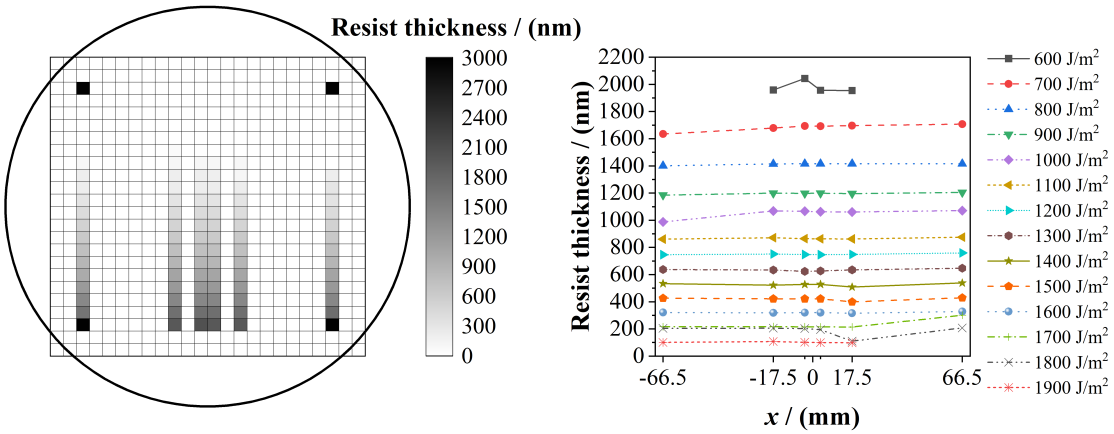

Figure 5.2: Photoresist thickness for double puddle development.

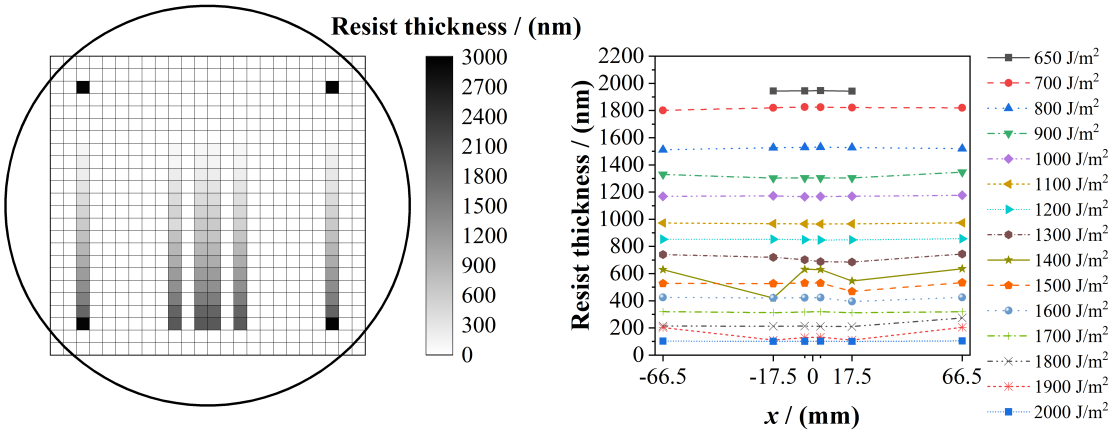

Figure 5.3: Photoresist thickness for quadruple puddle development with half development times.

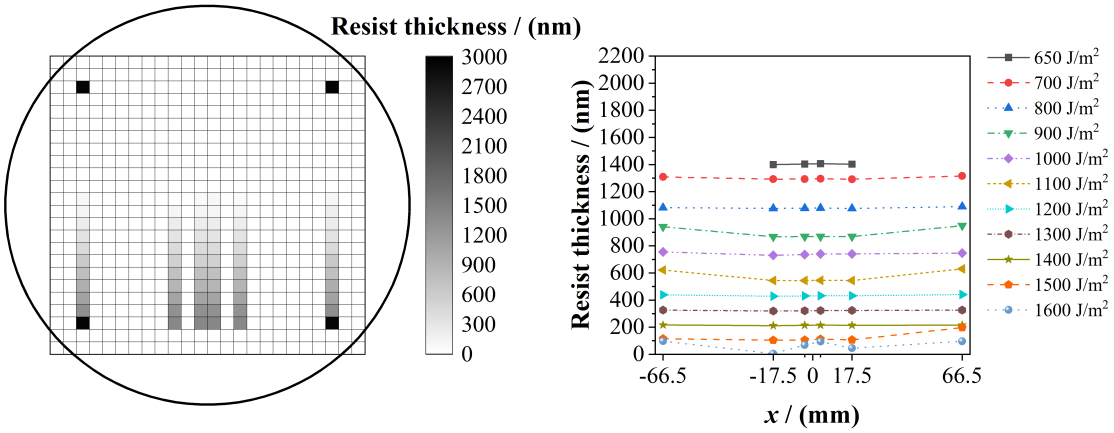

Figure 5.4: Photoresist thickness for quadruple spray development with half development times.

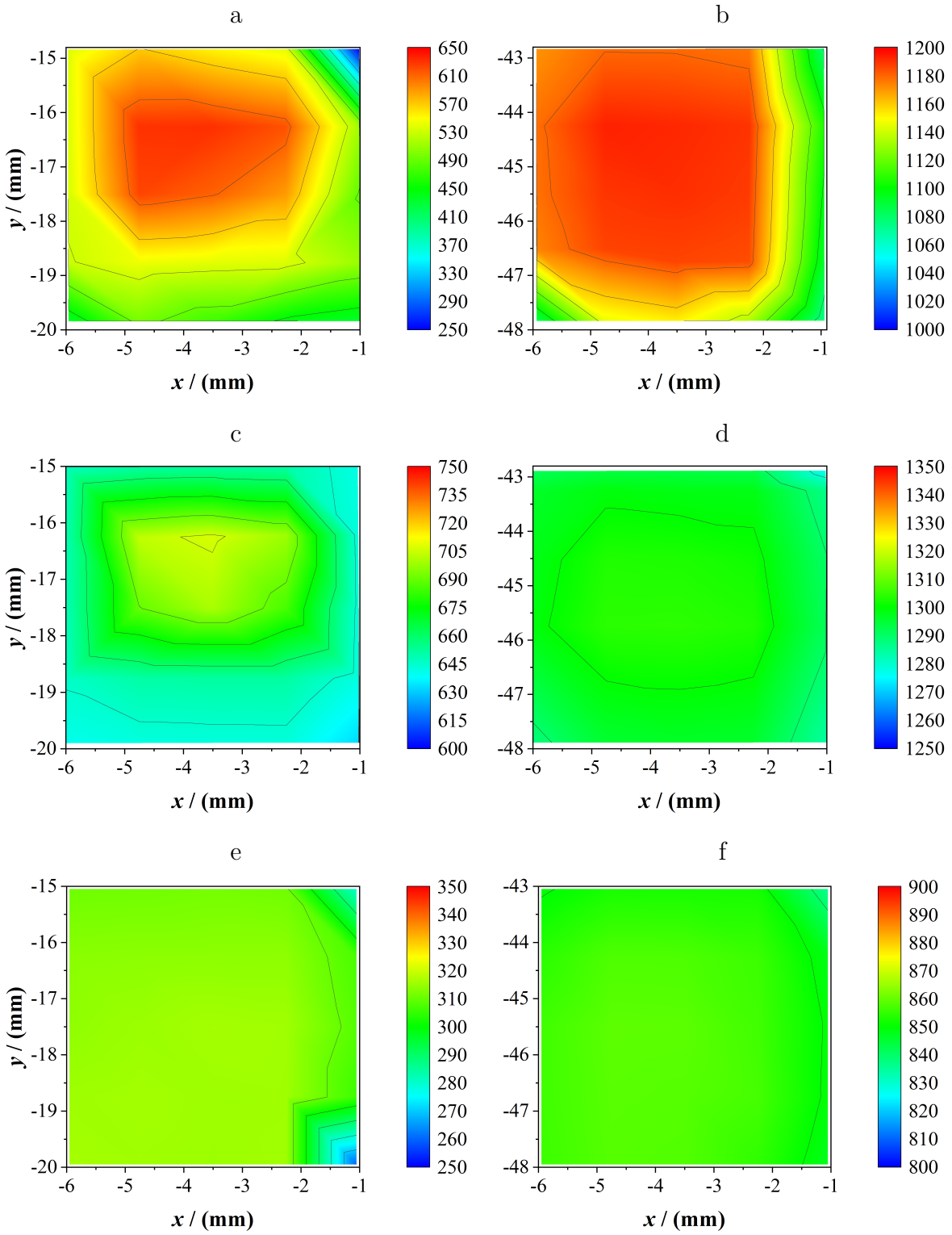

Figure 5.5: Photoresist uniformity of test fields with exposure doses of 1300 J/m^2 and 900 J/m^2 for double puddle development in a) and b), quadruple puddle development in c) and d) and quadruple spary development in e) and f).

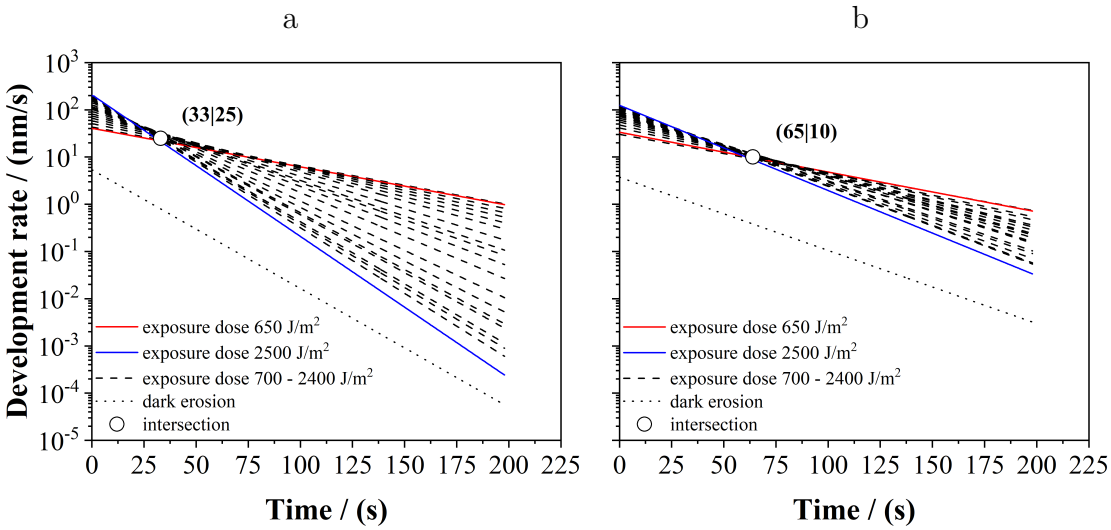

Figure 5.6: Development rate for TMAH developer concentrations of 2.6% in a) and 2.38% in b) dependent upon the exposure dose for the quadruple spray development process.

Experiments employing the standard double puddle process exhibit irregularities of remaining photoresist for specific exposure doses. This is especially the case when the spot of dispense in the substrate center generates larger thickness variations due to a turbulent flowing developer medium during the dispense. This effect is confirmed via the measurements of the field homogeneity. For exposure fields near the spot of dispense, irregularities of up to 400 nm are monitored in Fig.5.5a, while the photoresist surface of the more distant exposure field displays a homogeneity of approx. 100 nm. The development uniformity is enhanced for a quadruple puddle process at a similar overall development time as the double puddle. The doubled swap of the developer medium results in a photoresit uniformity approximately 70 nm and 30 nm for 1300 J/m^2 and 900 J/m^2, respectively. Nevertheless, irregularities in the spot of dispense still occur. The best results are produced by a quadruple spray development process with similar cycle times to the quadruple puddle process. Caused by steady nozzle movement during developer coating, minimum turbulences are generated and result in nearly homogeneous surfaces across the substrate. The homogeneity of measured exposure fields range between 50 nm and 24 nm for exposure doses of 1300 J/m^2 and 900 J/m^2. Although the contrast curve for spray development is steeper and consequently

the process window for grayscale lithography shrinks compared to puddle development, this development technique nonetheless produces best photoresist uniformity at a lower developer consumption cost.

The development uniformity seems to be affected by the TMAH developer concentration and the exposure doses of the test fields. Of course, the development rate changes from the edges to the center of the exposure fields due to the diffusion limitation of TMAH in the aqueous developer solution. To further enhance the photoresist homogeneity, experiments with TMAH developer concentration of 2.6% (standard MIF developer contains 2.38% TMAH) are performed using the quadruple spray development with exposure doses similar to those from previous experiments. In addition, the correlation of exposure dose to the development rate is investigated for both TMAH concentrations. Figure 5.6a examines surprisingly high development rates for a relatively small increase of the TMAH concentration in the developer solution. The unexpected hike in the development rate with higher TMAH concentration leads to its uselessness for the development in grayscale lithography processes. For both developer concentrations, the development rate shows a strong dependence upon the exposure dose. The higher the exposure dose, the higher the development rate, a finding that fits the observations of the exposure field homogeneity. A high development rate leads to a higher consumption of alkaline molecules and development depletion at the exposure field center if the diffusion rate of alkaline molecules is slower than their consumption. For this reason, test fields with lower exposure doses result in more uniform photoresist surfaces. Despite the different development properties for distinct exposure doses, the development rates converge at one point, which is marked as an intersection in Fig.5.6a and 5.6b. At this point, the exponential decay of the development rate turns into saturation, indicating the start of developer depletion. For a developer concentration of 2.38%, this intersection appears after 65 s for a development rate of 10 nm/s.

5.2 Fabrication of test structures

The study of the TSLM prediction quality is performed on the fabrication of pyramidal, chess field and spherical test structures, which are illustrated in Fig.5.7-Fig.5.9. Each structure is produced with two exposure doses of 3000 J/m^2 and 15000 J/m^2. This exposure variance spans a wide process window, in which the prediction accuracy of the TSLM is investigated. In Sec.5.1 of the present work, the relevance of diffusion effects during the development process was revealed. To this end, the sample structures are created in lightfield and darkfield ambients to test the influence of ambient development conditions on the targeted topographies. In order to handle the significant amount of data necessary for photomask design, a combination of Matlab and Tanner L-Edit scripts were used to automatically generate mask features and their positioning on the photomask based upon the TSLM.

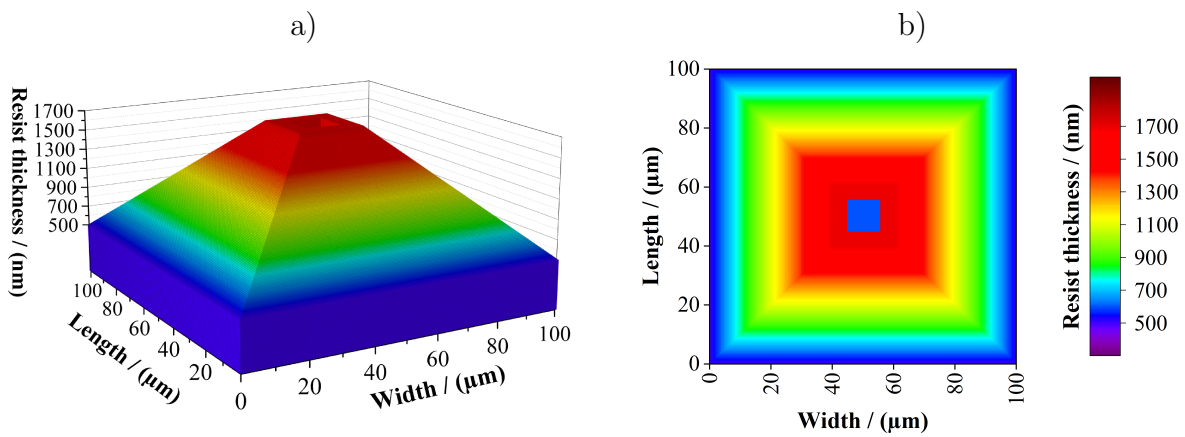

Figure 5.7: a) 3D-layout of the pyramid topography with a base length of 100 µm and a slope angle of ≈2.4°.[119] The tip of the pyramid is replaced by a quadratic cavity with a surface area of 11 µm x 11 µm and a depth of 1.1 µm. b) Top-view of the pyramidal topography.

Figure 5.10 shows a microscopy image of an exposure field of the test structures for an exposure dose of 3000 J/m^2 after spray development. The entire exposure field consists of four horizontal repeated sphere, bowl, chess field and pyramid arrangements in distinct ambient development conditions. The magnification of the test structures in the dark field ambient shows discrete coloring, which indicates different height steps of the remaining

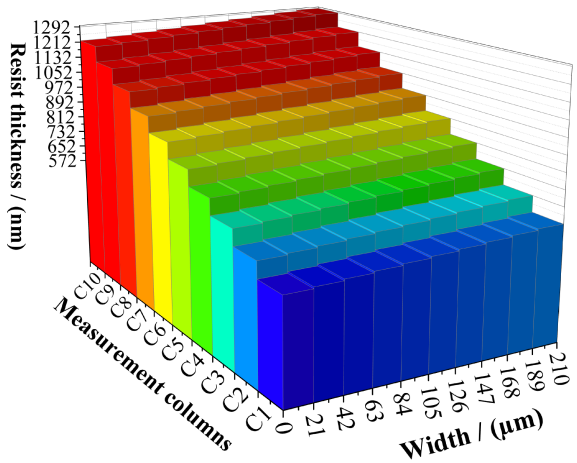

Figure 5.8: 3D-layout of the chess field topography with a base length of 210 µm and height variation of 8 nm in a range of 500-1292 nm between the 21 µm x 21 µm fields.[119]

photoresist. Profilometer measurements, which are displayed in Fig.5.11 to Fig.5.13, confirm the microscopy inspection. The number of printable height variations in the photoresist is limited due to a fixed step size of ≈ 100 nm. Pyramidal and spherical structures exhibit more or less satisfying precision for the desired topographies. However, the chess field samples could only be printed insufficiently into the photoresist. Chess field columns are illustrated in Fig.5.11a and Fig.5.11b. The measured lines cannot replicate any of the 8 nm steps. Instead, the measurement lines follow a decreasing exposure energy to certain thresholds where the next height step of approx. 100 nm is attainable. With respect to Fig.2.19, the thicknesses of height jumps correlate with the maximum intensities for a standing wave with a mercury i-line wavelength. Unique to the spherical shapes, a measured dome and bowl structure is shown in Fig.5.12a and Fig.5.12b. Both shapes exhibit high errors in the arc between 1500-2500 nm for the dome and 500-2500 nm for the bowl, which are caused by a linear increase of feasible height steps. The best results were measured on the pyramid samples, which are illustrated in Fig.5.13a for light field and in Fig.5.13b for dark field ambient. Both structures are closely to the sample design with accurate pyramid slopes and trenches in the structure center. Photoresist thickness in the dark field is thinner than in light field ambient, which results from the distinct development conditions of the sample structures.

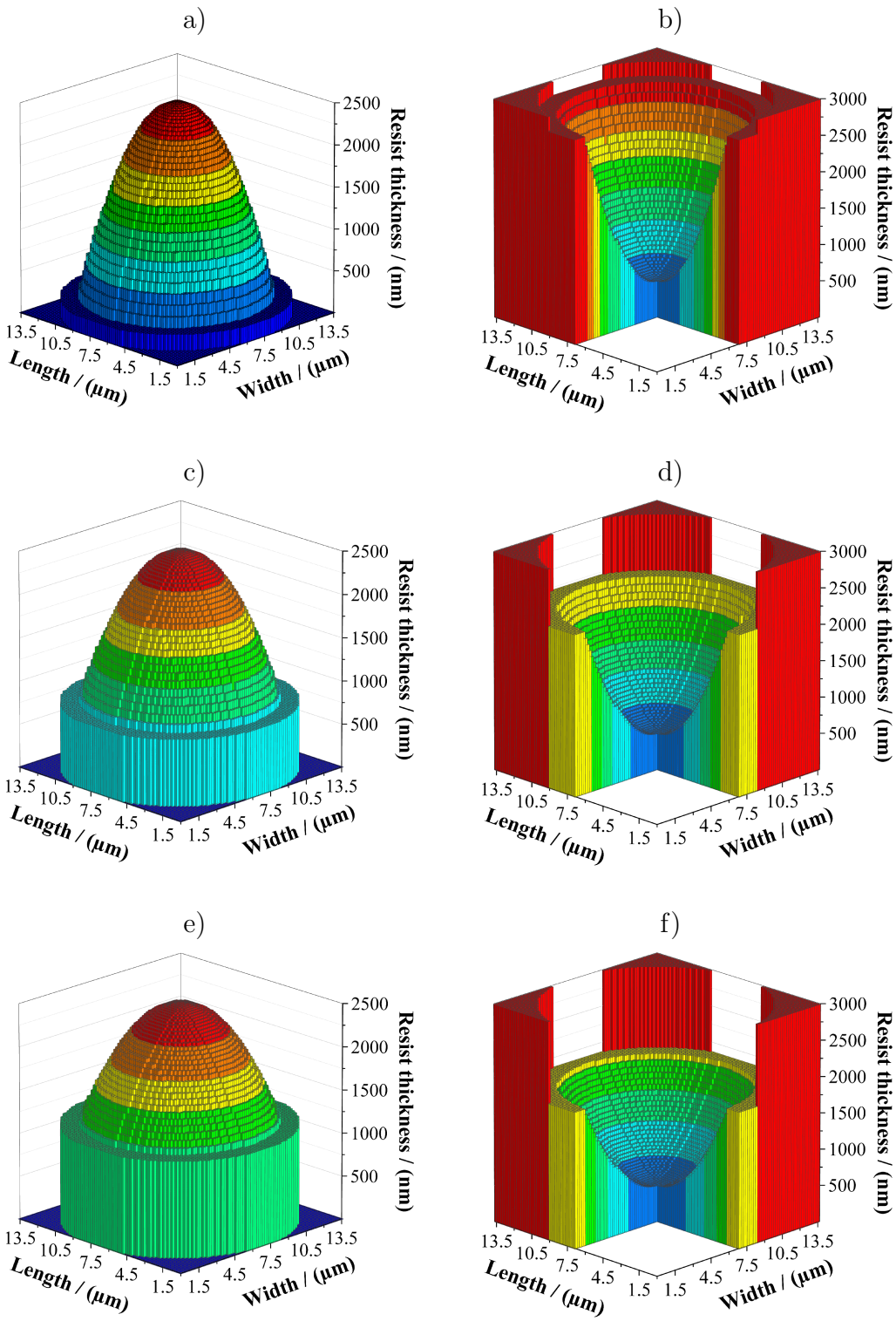

Figure 5.9: 3D-layout of dome and bowl topographies with a base diameter of 12.3 µm, radii of 120 µm in a)[119] and b), 160 µm in c) and d) and 200 µm in e) and f) with heights and depths of 2.5 µm.

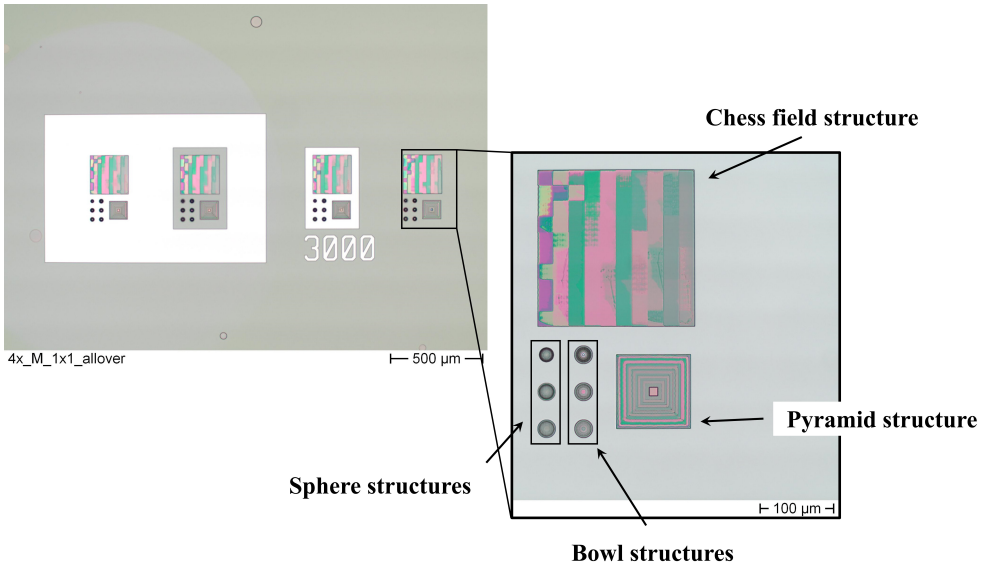

Figure 5.10: Microscopy image of an exemplary exposure field of the test structures for an exposure dose of 3000 J/m^2.

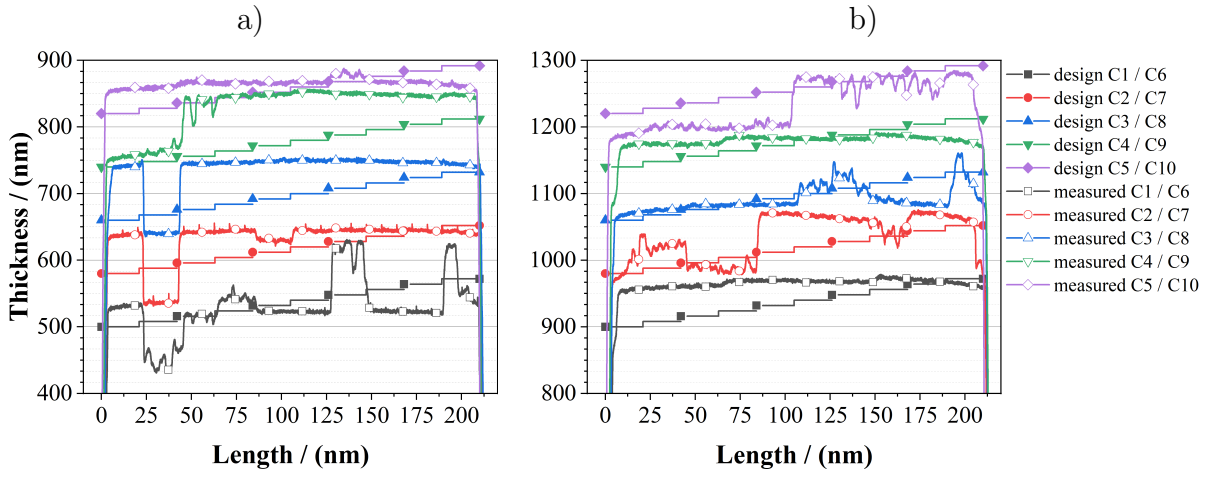

Figure 5.11: Measurements on an exemplary chess field for each column from C1-C5 in a) and from C6-C10 in b) in a light field ambient for an exposure dose of 3000 J/m^2. Dip development with similar overall development time to puddle development was applied for fabrication.

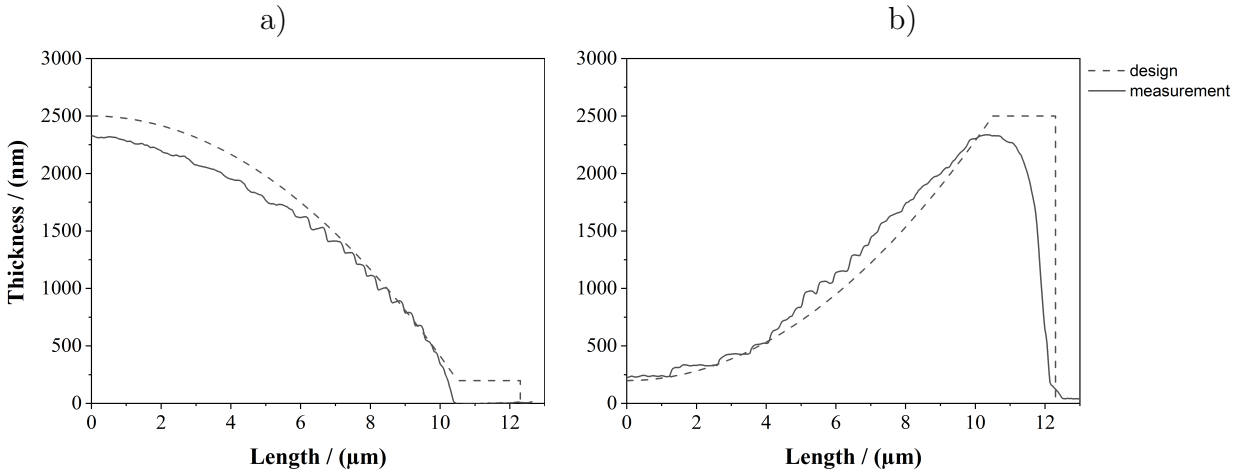

Figure 5.12: Measurements of an exemplary dome in a) and bowl in b) with a radius of 120 µm in a light field ambient for an exposure dose of 3000 J/m^2. Spray development is applied for fabrication.

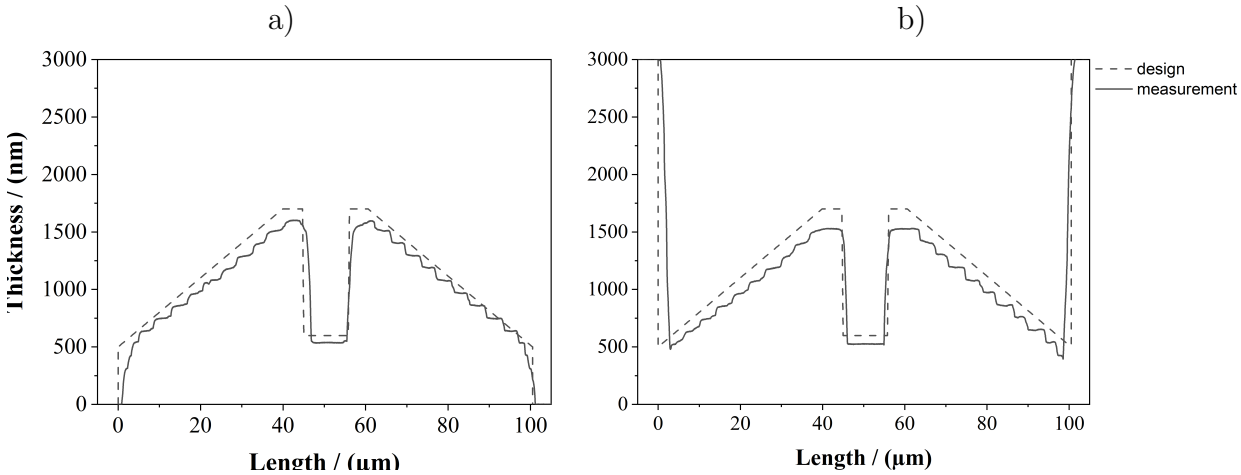

Figure 5.13: Measurements of exemplary pyramid structures in light field ambient in a) and dark field ambient in b) for an exposure dose of 3000 J/m^2. Dip development with similar overall development times to puddle development was applied for fabrication.

In order to flatten the surface of the pyramid sample structures, a subsequent heat treatment above the softening temperature of the photoresist is executed. The optional lithography process is referred to as hardbake or reflow and can be applied for several reason, which are discussed in further detail by C. Koch and T. Rinke.[10] At temperatures approximately 110-130°C, the photoresist begins deforming, especially in areas with higher surface tension. The reflow is applied on the pyramidal sample structures of Fig.5.13a and Fig.5.13b and the relevant results shown in Fig.5.14a and 5.14b. Both samples were successfully flattened

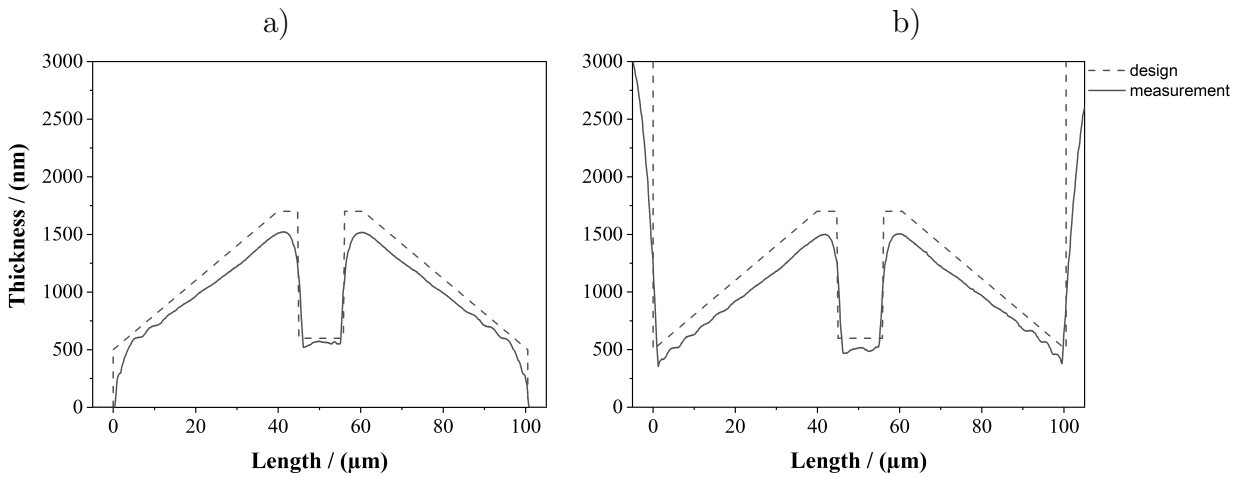

Figure 5.14: Measurements of the pyramid structures of Fig.5.13a and Fig.5.13b after hardbake.

on the pyramid slopes, resulting in deformed slope angles. The trench edges are rounded after the reflow and the trench bottom exhibits a hillock that is caused by the surface tension at the trench top and bottom edges. The deformation of the structures during the subsequent heat treatment demonstrates that the reflow process is an inappropriate method for flattening the structure surfaces. In addition, the further hardbake could lead to other photoresist reaction (e.g., cross-linking or brittle of the photoresist). The application with limited thermal budget may be harmed through this kind of surface-smoothing technique.

5.3 Application of anti-reflective coatings

In Sec.2.3.5, the formation of a standing wave in the photoresist film and the resulting sidewall scallops are discussed. The post-exposure bake is used in standard lithography processing to eliminate sidewall scallops through the diffusion of exposed PAC. The PEB is not applied in the presented grayscale lithography processes, due to the isotropic PAC diffusion and the resultant washed-out concentration profiles of converted PAC in the photoresist film. Further, the TSLM does not integrate a diffusion model for the calculation of the remaining photoresist, which would led to inaccurate predictions at the intersection of exposed and unexposed PAC concentrations. As was presented in the previous section, thin 3D-structures and profiles with low photoresist gradients cannot be fabricated accurately without suppressing the standing wave. In the semiconductor industry, the exploitation of anti-reflective coatings is state-of-the-art for resolution enhancement. These anti-reflective coatings act as quarter-wavelength layer on the top (TARC) or bottom layer (BARC) of the photoresist. A simulation of the suppression of the standing wave is shown in Fig.5.15 for a BARC anti-reflective coating with a substrate reflectivity from 0-1. The simulation reveals

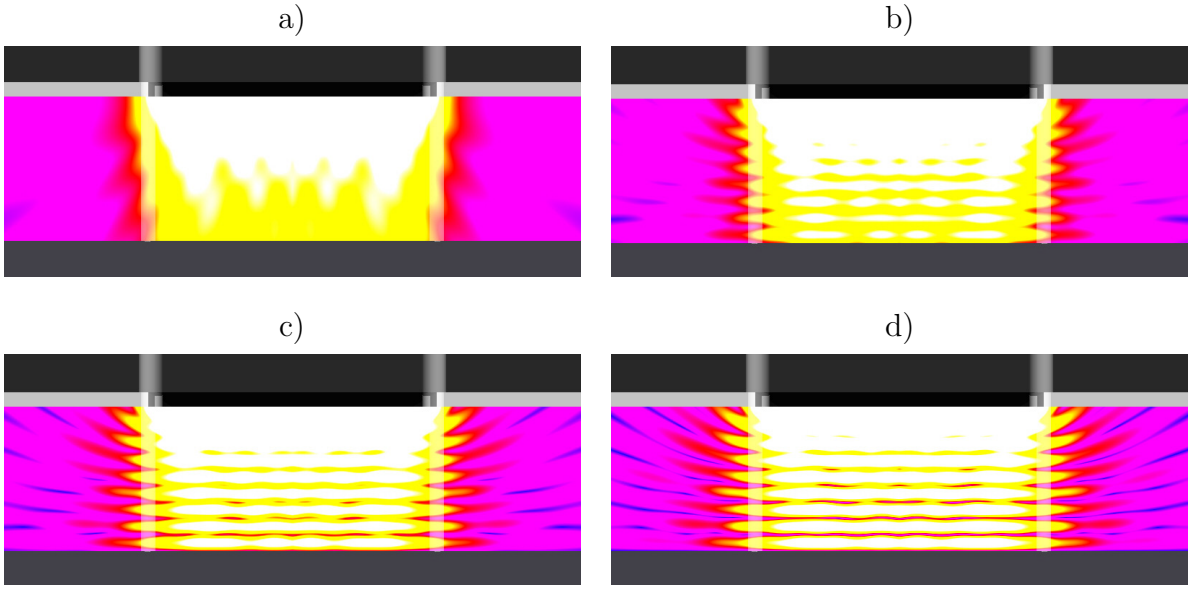

Figure 5.15: Simulation of a standing wave in the photoresist film with increasing intensity from blue to white for substrate reflectivity of 0 in a), 0.25 in b), 0.5 in c) and 1 in d).[10]

a nearly complete suppression of destructive interference inside the photoresist film with the use of a BARC. The BARC material AZ BARLi II is specified with an attenuation of the standing wave up to 94%[122], while the TARC material AZ Aquatar VIII A45 provide 83%[123]. Both materials work with similar optical principles but require different processing procedures. The application of TARC is preferred in the semiconductor industry because of its process simplicity. AZ Aquatar do not require any additional heat treatment and is water soluble, which leads to clean photoresist structures after the development process. Thus, subsequent processes (e.g., dry etching) can be executed with recipes for standard photoresist on silicon. The use of BARC is connected to several processing disadvantages. The material requires an additional softbake after the spin coating and reduces the thermal budget of the processed semiconductor device. Moreover, BARC remains on the substrate after the finished lithography process with slightly different etch selectivity compared to the photoresist, as is illustrated in Fig.5.16. Following conventional lithography with BARC,

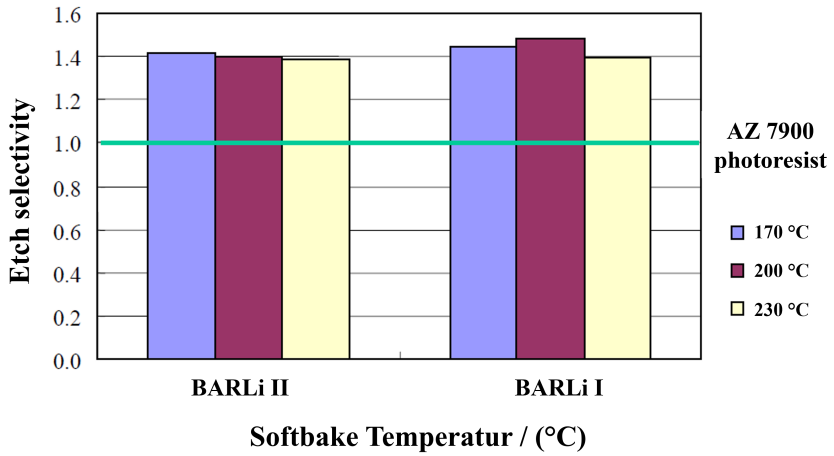

Figure 5.16: Etch selectivity of AZ BARLi I and AZ BARLi II versus novolak-based photoresist AZ 7900 for different softbake temperatures. Etch condition: Samco RIE-10N, CHF_3/O_2 in 40/10 sccm, 60 W, 60 s.[122]

plasma conditions and etch time for both materials are set in sub-sequences of the recipe for each etch process. The relatively small required effort of process adjustments becomes more demanding when etching gray-scaled photoresist. Due to the permanent change of open ar-

eas of the substrate, photoresist and BARC, the plasma conditions need to be continuously adjusted. Multiple test procedures are necessary to find a stable process window.

Investigating the smoothing performance of both anti-reflective coatings are performed on the photomask design of the previous spherical, pyramidal and chess field samples. To this end, processes for the coating of TARC on photoresist and BARC on silicon are developed. To produce sufficient anti-reflective coatings, the thickness accuracy of the coated layer is from high priority. Optimal, anti-reflective performance requires a layer thickness of 200 nm[122] for BARC and 65 nm[123] for TARC material. Before exposure, the anti-reflective coatings are optically measured to ensure the best possible performance. Figure 5.17 shows the measured thickness distribution and the relative error vis-a-vis the optimum across the substrates for the BARC and TARC samples that are used.

To ensure an optimal suppression of the standing wave, just structures at sites with a maximum error of $\pm 6\%$ in terms of the thickness of the anti-reflective coating are evaluated. Exemplary measurements of pyramidal structures in light field ambient with anti-reflective coatings for an exposure dose of 15000 J/m^2 are shown in Fig.5.19. The pyramidal samples exhibit smooth slope surfaces with a distinct slope angle compared to the design with BARC. Further, the generated cavity extends too deep in the pyramidal structure. Both the inaccurate slope angles and the cavity arise from the shifted optical properties of the film stack with BARC. The application of TARC does not provide any smoothing capability in the conducted experiments. All of the measured test structures still exhibit the minimal step size of ≈ 100 nm of the photoresist. It is thus assumed that an insufficient attenuation of the standing wave with the use of TARC lead to this result. The presence of a standing wave causes a varying clearance exposure dose, dependent upon the photoresist thickness. The dependency of clearance dose on the initial photoresist film thickness is known as the swing curve.[8] Therefore, the attenuation of the standing wave should result in suppressed amplitudes of the swing curve. In order to confirm the assumption of insufficient attenuation of the standing wave with TARC for surface-smoothening, the clearance dose is measured for 24 different resist thicknesses with the spray development process used for the fabrication

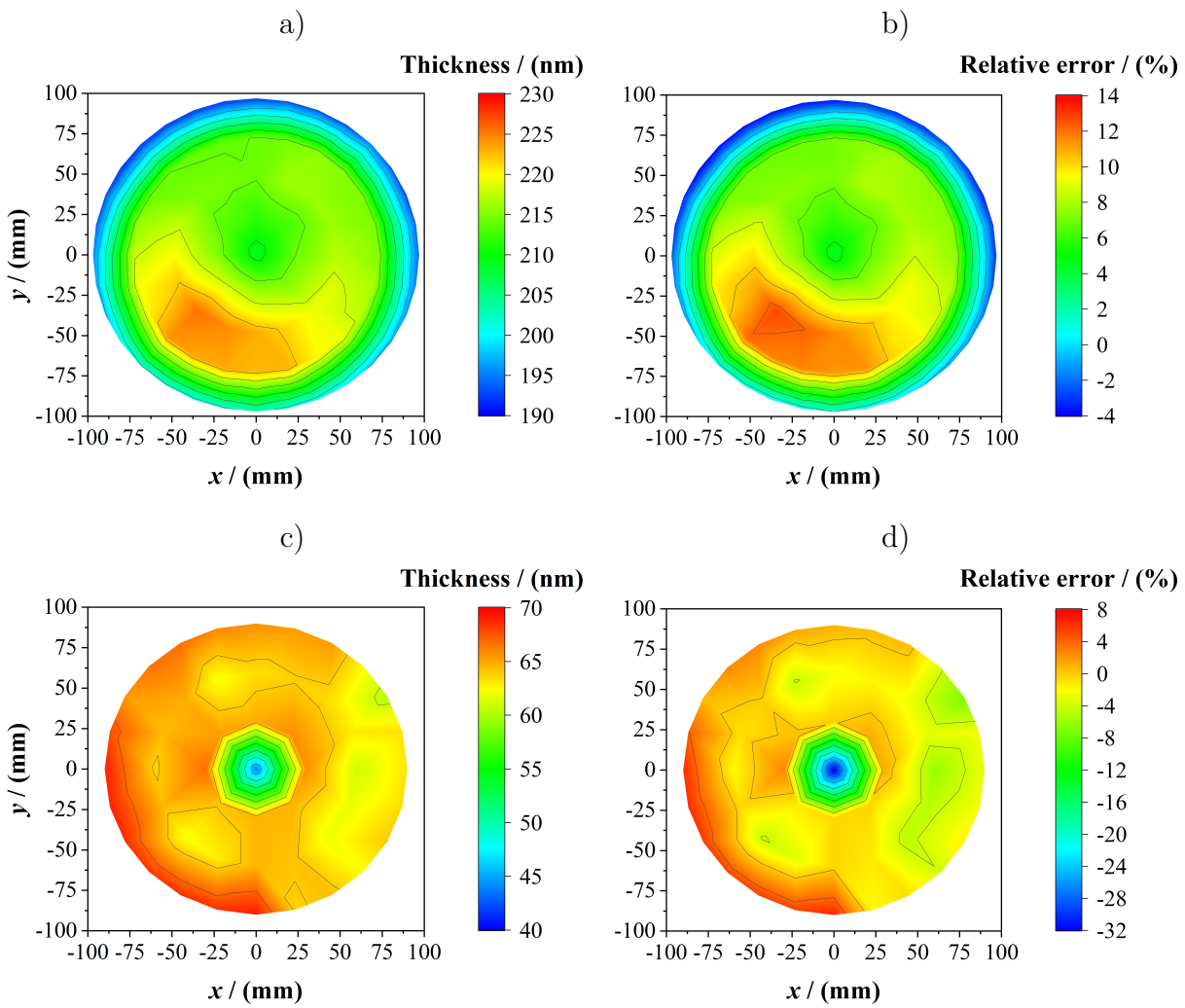

Figure 5.17: Thickness measurement and relative error to the optimum for BARC in a) and b) and TARC in c) and d).

of the test structures. The measurement data of the swing curve is illustrated in Fig.5.18 together with a sinusoidal fit function following

$$E_{Clearance} = A\ sin\left(\frac{T-e}{b}\right) + cT + d, \tag{5.1}$$

where $E_{Clearance}$ is the clearance dose, T represents the photoresist film thickness and A, b, c, d and e are variable fit parameters. The fit parameters of the swing curve, which are listed in Tab.5.1, reveal a swing curve amplitude of approximately 15.4 J/m^2, which is equal within the error tolerance to the parameter b of the fit in the dose correction of Sec.4.2.

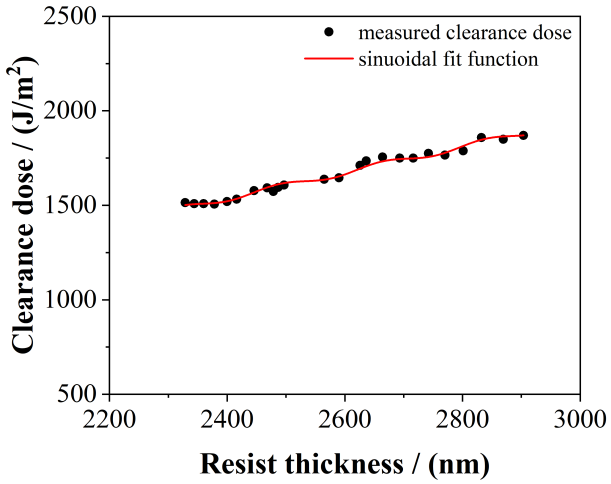

Figure 5.18: Swing curve of the photoresist with use of TARC. Spray development is applied for the determination of the clearance doses.

This parameter approximates the threshold exposure energy needed for the PAC conversion. It is the swing curve amplitude in the range of this threshold energy that means no PAC conversion occurs in the swing curve maxima. The fit parameters found in Tab.5.1 show high errors due to a limited data set of clearance doses. However, with a coating accuracy <6% and a functional surface-flattening with the use of BARC, the conclusion presented seems plausible in this context.

Performance of the surface smoothing ability of BARC is also tested on the spherical test structures and chess fields. The investigation of a set of chess field columns in light field ambient, which is displayed in Fig.5.20, involved an exposure dose of 3000 J/m^2 and 15000 J/m^2. For both exposures, the edge data points are neglected due to a missing proximity exposure correction for the edge areas. In addition, measurement profiles of exemplary domes of all radii in light field ambient for an exposure dose of 3000 J/m^2 and corresponding atomic force microscopy 3D-scans of the dome surfaces are shown in Fig.5.22-Fig.5.24. The data of the random measured chess field columns cannot replicate any of the desired 8 nm height steps of the actual chess field design. The surface roughness is significantly higher for an exposure dose of 3000 J/m^2 than for 15000 J/m^2, with a peak-peak mean value approximately 20-40 nm. The higher surface roughness for an exposure dose of 3000 J/m^2 is

Table 5.1: Fit parameters of Eq.5.1 for the determination of the photoresist swing curve with TARC.

A / (J/m^2)	15.35198±18.31065
b / (nm)	27.83879±1.42864
c / (J/nm m^2)	0.6827 ±0.02026
d / (J/m^2)	-101.69902±52.51203
e / (nm)	-178.12899 ±136.74976
R^2_{cor}	0.98253

the result out of a low exposure time conditional on higher areal image intensities for larger photomask features. Nevertheless, chess field column slopes are fabricated precisely for an exposure dose of 15000 J/m^2. The discrepancies between design and sample structures resulting from the chemical resolution limit of the photoresist of approximately 400 nm[120]. A closer inspection of the measured columns shows height variations at lateral positions that fit to the design but that are covered from a surface roughness higher than 8 nm. The AFM 3D-scan of the surface area of four single height steps of a sample chess field with an exposure dose of 15000 J/m^2 is illustrated in Fig.5.21b. A horizontal and a vertical line measurement is displayed in Fig.5.21a. In the vertical line measurement, the height variation between two columns is clearly visible, as is a height step of approximately 8 nm, which remains evident in the noisy data for the horizontal line measurement. The finding of a visible 8 nm height step in a surface with noise in the same scale is not practically relevant, but of significant interest for the investigation of the model prediction accuracy. A change to a high-resolution photoresist would lead to a more precise fabrication of the small step size of the chess field samples. The profiles of the sphere structures examine a precise replication of the designed domes. Arcs of the three radii are accurately printed. However, the base of the dome with 120 µm radius is not existent and is deformed for the domes with radii of 160 µm and 200 µm, caused by the photomask fabrication for photoresist on bare silicon.

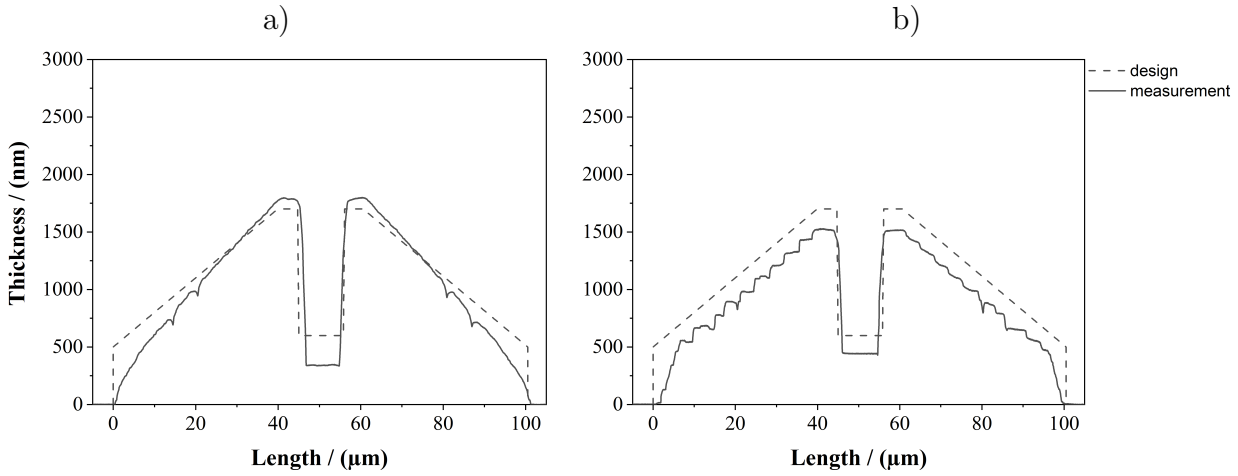

Figure 5.19: Measurement of exemplary pyramid structures in light field ambient with BARC in a) and TARC in b). Spray development is applied for the fabrication.

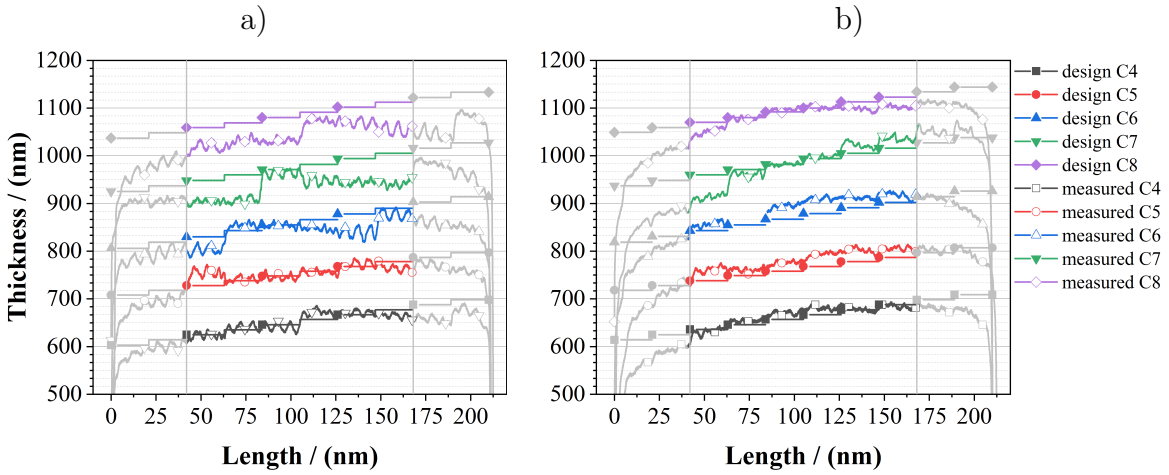

Figure 5.20: Measurement of a set of chess field columns in light field ambient with BARC for an exposure dose of 3000 J/m^2 in a) and 15000 J/m^2 in b). Spray development is applied for the fabrication. The first two steps on the structure edges are neglected.

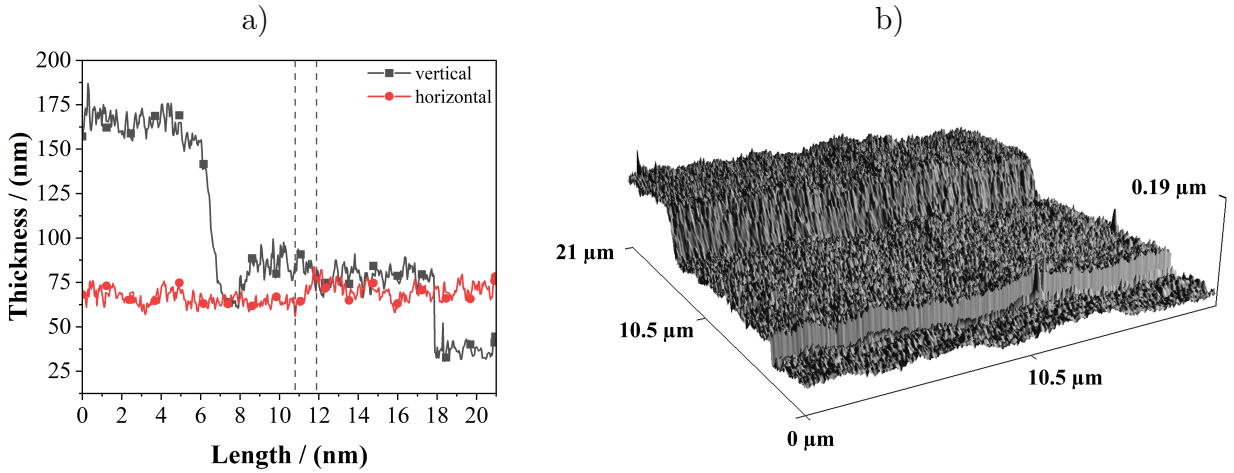

Figure 5.21: AFM measurement of four chess field steps between C4 and C5. Horizontal line measurement at $y = 12.73$ µm and a vertical line measurement at $x = 12.60$ µm is shown in a). Dashed lines highlight the area of the 8 nm height step. The 3D-scan of the surface of a 21 µm x 21 µm measurement field is displayed in b).

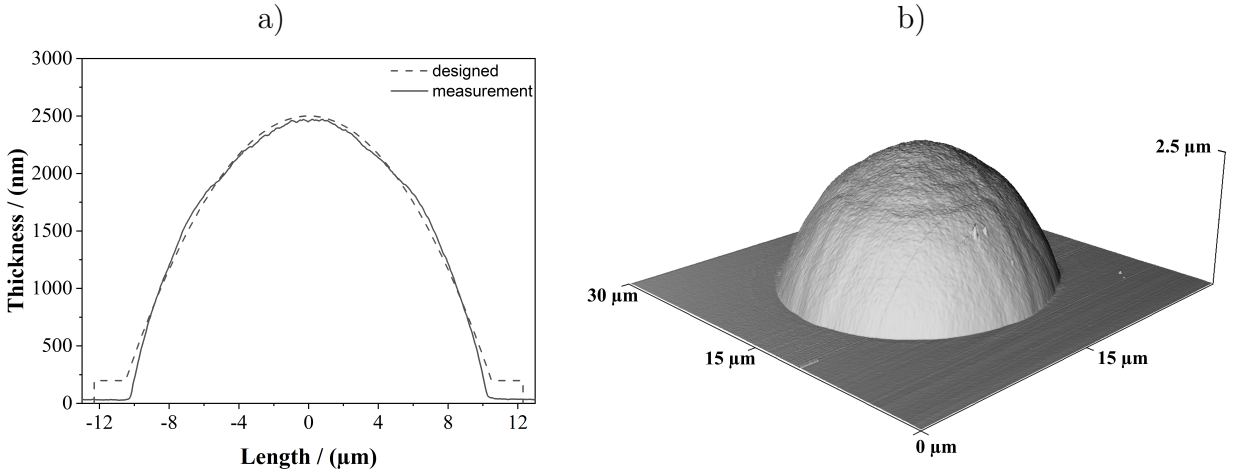

Figure 5.22: AFM measurement of the dome profile with a radius of 120 µm in a) and the corresponding 3D-scan of the spherical surface.

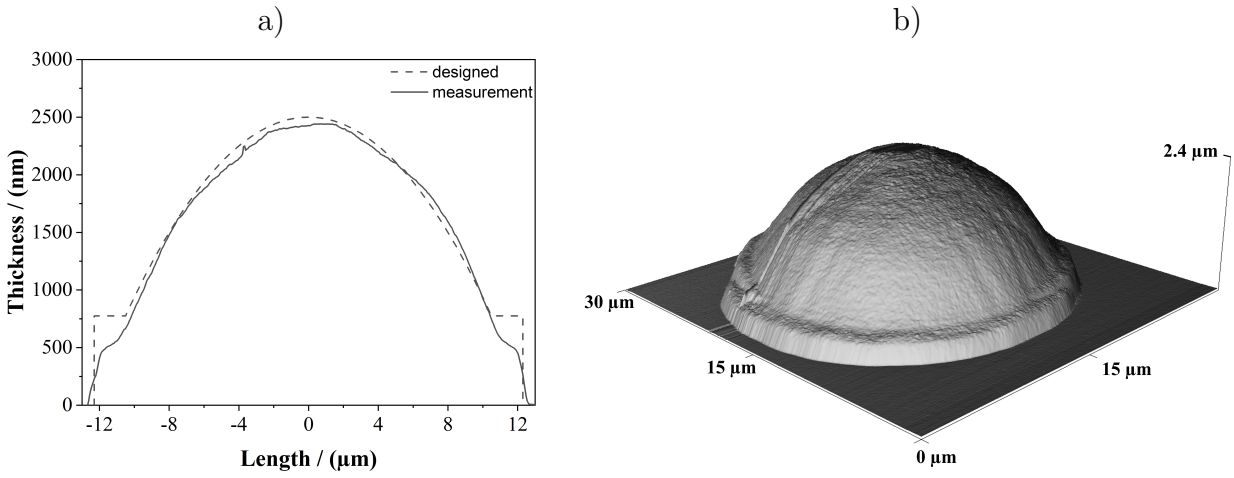

Figure 5.23: AFM measurement of the dome profile with a radius of 160 µm in a) and the corresponding 3D-scan of the spherical surface.

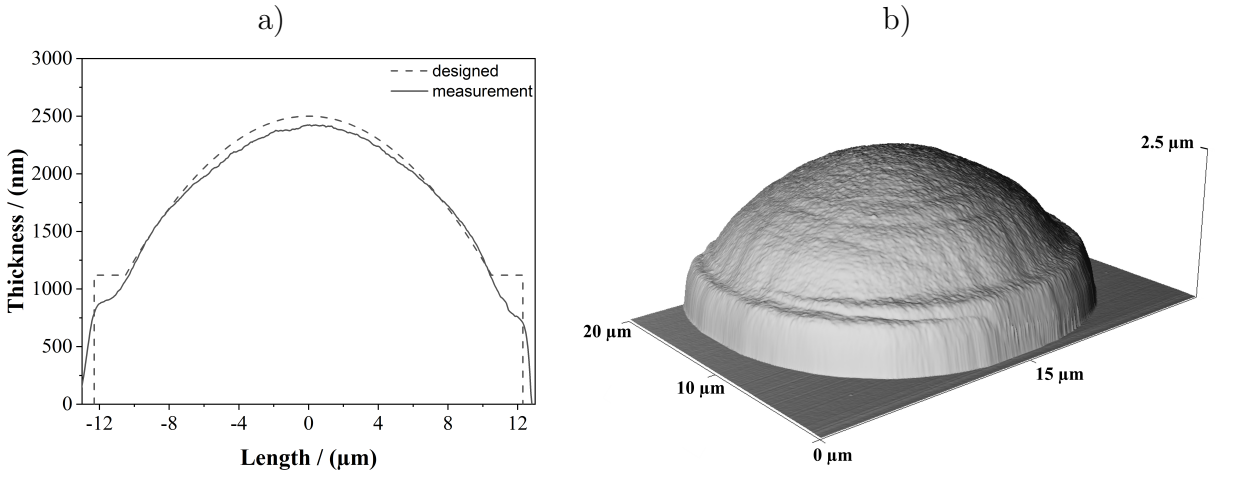

Figure 5.24: AFM measurement of the dome profile with a radius of 200 µm in a) and the corresponding 3D-scan of the spherical surface.

CHAPTER 6

Reduction of process costs and environmental footprint

In previous chapters, grayscale lithography was discussed as a sophisticated method to print arbitrary 3D-structures into photoresist, which are subsequently transferred into the substrate by etching techniques or implantation. Moreover, by applying grayscale lithography rather than several binary lithography steps, the process costs and environmental impact of traditional process flows can be reduced. To determine the extend of the potential savings, this chapter compares a traditional process flow with an imaginary process flow that includes grayscale lithography for the fabrication of a low-noise junction-gate field-effect transistor (JFET). The applied JFET device is entirely manufactured in the Fraunhofer EMFT's cleanroom. For detailed information of the semiconductor device, the present work makes reference to the thesis from L. Sturm-Rogon.[124]

The low-noise JFET concept allows DC characteristics, such as channel current and transconductance, to be set largely independent from the length of the top gate control electrode via dividing the channel of the JFET into two distinct regions: a main channel and an extended drain channel. A schematic process flow of the JFET fabrication developed by L. Sturm-Rogon is illustrated in Fig.6.1. The applied process begins with the local oxidation of the silicon substrate, which acts as an implantation mask for the back gate. Subsequently, in two consecutive lithography steps the main channel and the extended drain channel are generated by separated implantation processes. After the generation of the gate oxide, the source and drain of the JFET are produced via high implant doses after another lithography step. The top gate is implanted before a borophosphosilicate glass (BPSG) is coated on top of the device; another annealing follows. In order to contact source, drain and the top gate, the BPSG is opened and filled with conductive material before contact pads for wire

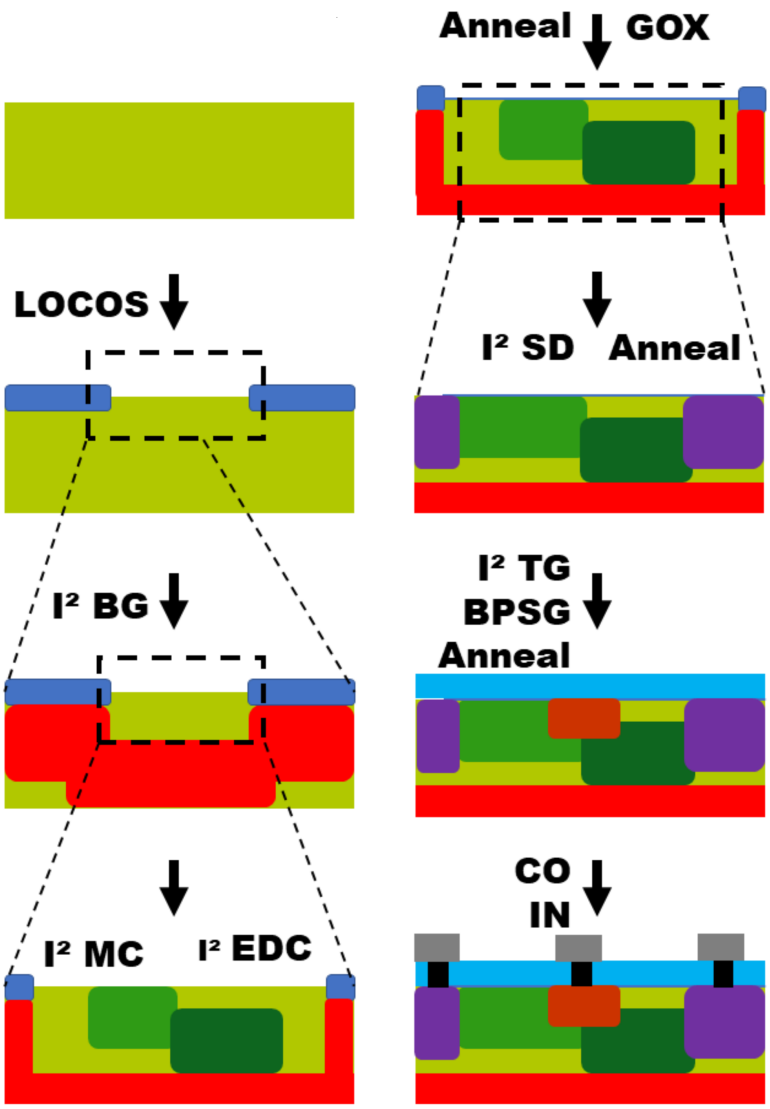

Figure 6.1: Schematic process flow of the main steps for the fabrication of the developed JFET.[124] Abbreviations: LOCOS = Local oxidation of silicon; I^2 BG = Implantation of back gate; I^2 MC = Implantation of main channel; I^2 EDC = Implantation of extended drain channel; GOX = Gate oxide; I^2 SD = Implantation of source/drain; I^2 TG = Implantation of top gate; BPSG = Borophosphosilicate glass; CO = Contact opening; IN = Metal I;

bonding are generated in a final process step. The main process flow does not include several essential cleaning steps and inspections, such as optical microscopy or layer thickness measurement via ellipsometry. More specifically, the two-step implantation of the main and extended drain channel offer the possibility of enhancement through grayscale lithography. To this end, an alternative process flow is developed in which the two-step implantation is substituted with a single grayscale approach in order to reduce the process costs and overall environmental impact.

In Tab.6.1, the traditional process flow is shown in comparison to a slimmed down process flow that contains the grayscale lithography approach. The presented flow shows the creation of the main and extended drain channel and begins after the successful generation of the back gate with subsequent clean and ends with the wafer clean in front of the production of the gate oxide. With the use of grayscale lithography, eight process steps could be saved in the overall process flow. The relative fabrication costs for the generation of the main and extended drain channel are reduced by 43.35% via the grayscale approach.

In future industrial micro- and nanotechnology manufacturing, the majority of process costs will be affected by environmental sustainability. Caused by increasing effects of global warming and species extinction, the trend is increasingly towards more environmentally friendly manufacturing. In lithography processes, in particular, the material yield and toxicity is an issue and future regulations are expected to become stricter. Thus, examining the possible material savings for the change of binary to grayscale lithography is necessary. For this purpose, the used material volumes and electric energy consumption of the standard CMOS double puddle development process used for 3 µm photoresist films at the Fraunhofer EMFT is compared to the spray development process that is applied for grayscale lithography. The consumption of photoresist, developer, de-ionized water and stripper medium are displayed in Tab.6.2 for both processes. The use of spray development reduces the consumed developer medium by 45.92% compared to puddle development. Electric energy consumption for spray development will increases approx. 0.1 kWh as a result of the quadruple spray treatment.

Table 6.1: Comparison of the traditional and the grayscale process flow for the generation of the main and extended drain channel of the JFET device.

Traditional process flow	**Grayscale process flow**
Photoresist coating	Photoresist coating
Exposure	Exposure
Photoresist development	Photoresist development
Microscopy inspection	Microscopy inspection
Implantation of MC	Implantation of MC & EDC
Photoresist strip	Photoresist strip
Microscopy inspection	Microscopy inspection
Wafer clean	Wafer clean
Photoresist coating	
Exposure	
Photoresist development	
Microscopy inspection	
Implantation of EDC	
Photoresist strip	
Microscopy inspection	
Wafer clean	

Table 6.2: Media volumes used for the puddle and spray development. The presented volumes corresponding to the development of 3 µm photoresist films for CMOS compliant production.

Medium	**Puddle development**	**Spray development**
Photoresist volume / (ml)	7	7
Developer volume / (ml)	113.4	61.33
De-ionized water volume / (ml)	161.67	161.67
Stripper volume / (g)	2.22	2.22

However, the presented grayscale lithography omits the PEB, which compensates the electric energy increase. Even though PEB is applied, the slight increase of energy consumption is of secondary importance when cleaning wastewater is taken into account. Considering the presented techniques in Sec.2.3.6, the reduction of wastewater cleaning costs exceed the increase in electricity costs by a factor of five for spray development with the application of U.S. electricity prices.[125]

It is clear that the energy and material consumption decreases significantly the more binary lithography steps can be substituted by one grayscale lithography process. At this point, however, the lithography process should not be just considered in and of itself. A relevant amount of electricity, water and chemical media consumption, garbage disposal costs and wastewater cleaning is produced via intermediate process steps, such as photoresist stripping, inspections or standard wafer cleans. These intermediate processes would be reduced in similar quantity to the lithography steps, resulting in much lower costs and a lesser overall environmental impact. Precisely how much media and money could be saved depends upon several variables, including cleanroom infrastructure, energy prices, public regulations, among others. Gaining comparable results would take many more investigations that exceed the scope of this technological PhD thesis. However, it is shown that the greater efforts for the photomask creation and empirical tests for process optimization will result in lower process costs and reduced environmental footprint in production.

CHAPTER 7

Results and Conclusion

In the present thesis, an alternative method to the state-of-the-art grayscale lithography simulation for positive-tone photoresist in projection lithography is developed. Through a semi-empirical approach, the contrast curve of a given photoresist is mathematically described via a sectionally defined expression. This expression consists of three different phases in which the photoresist exhibits distinct absorption properties, which led to the name "three-state lithography model" or TSLM for short. The photoresist contrast curve is modeled via two sigmoid functions that include absorption properties and a factor correlated to the spatial filtering of the illumination system, which are interconnected by a spline function without physical content. All of the model parameters are determined through a straightforward test procedure, including the exposure with a test photomask. The empirical procedure and the data preparation of the parameter definition is explained in detail. Further, a parameter optimization method is presented for high prediction quality, resulting in better fabrication yield. The TSLM is highly beneficial for photomask designing due to the direct correlation between mask features and the remaining photoresist thicknesses following development. Thus, straightforward software programs can solve the TSLM for desired photoresist thicknesses and provide corresponding squared patterns for the photomask desing depending upon a preset exposure dose and illumination wavelength. For the context of this work, a MATLAB source code was programmed in order to solve the TSLM and generate command files for automatic pattern positioning. The generated command files were tested with the commercial photomask design software Tanner L-Edit.

In experiments, pyramidal, spherical and chess field structures were produced with a minimum vertical resolution of 20-40 nm if a bottom-anti-reflective coating (BARC) is applied.

Without using anti-refelective coatings, the vertical resolution is tied to the maxima distance of the photoresist swing curve with approx. 100 nm. In our tests, a top-anti-reflective coating (TARC) could not improve the vertical resolution due to the lower suppression of the standing wave in the photoresist. On chess field structures with BARC optimization, 8 nm height steps are visible for surfaces with a roughness in the same scale. For the practical fabrication of these step sizes a change to high resolution photoresists is recommended. Nevertheless, it is assumed that the TSLM is able to deliver proper values even in a sub-10 nm scale.

In a market analysis conducted, distinct grayscale lithography techniques were investigated with regard to future market trends. Primary markets for the use of grayscale lithography include the fabrication of micro-optical elements, micro-electro-mechanical systems, the semiconductor industry and market for microfluidic devices. Direct-write lithography techniques will increase their market volume for rapid prototyping, high resolution applications and intrinsic 3D fabrication. However, a closer look into the equipment market reveals future growth for projection lithography tools, especially for the i-line wavelength applied for the production of more-than-Moore devices. For this reason, the projection grayscale lithography technique will remain relevant in future fabrication sites. The use of this equipment for novel devices fabricated by grayscale lithography is quite likely.

Grayscale lithography can play an important role for prospective sustainable fabrication techniques in the future. This is particularly clear in the fabrication of a low-noise junction-gate field-effekt transistor (JFET). By applying grayscale lithography to the implantation of the main and extended drain channel, more than 43% of the fabrication costs could be saved. Moreover, developer medium volume is reduced by 46% for spray development compared to standard puddle development. The small increase of energy consumption is outweighed by the larger decrease of wastewater cleaning costs.

In general, grayscale lithography is a well-known technique through which arbitrary 3D-structures can be created. However, the simulation of these techniques require expensive software or is established on a semi-empirical basis with narrow process windows and non-

standardized test procedures. In contrast, the TSLM is an open-source photoresist model with a straightforward approach, which enables simple and cost-efficient photomask generation.

CHAPTER 8

Future Prospects

The TSLM is developed and tested for thin photoresist films of 3 µm. UV absorption in the photoresist film for such thicknesses is approximately homogeneous from top to bottom. This is altered for thick photoresist films due to the nonuniform distribution of photoactive compound. In order to find the limitations of the TSLM, further tests with thick photoresist films must be performed. In the case of significant prediction quality loss, a similar approach to the state-of-the-art simulators is followed, in which a thick resist is split into several thin areas where the approximation of continuous absorption is valid.

For commercial lithography simulation software, the integration of the TSLM could be a promising feature in order to integrate the straightforward method to correctly predict the photoresist heights in combination with a simplified photomask layout process, as recommended by Bhardwaj et al.[126]

One significant advantage of the TSLM is its simple parameter definition procedure, which is essential for unknown photoresist materials where no Dill parameters are available. Therefore, the TSLM is beneficial for recent academic works with biodegradable photoresists on chitosan basis.[127] The promising water-soluble photoresist has already been tested for UV and e-beam exposure and could also be used for grayscale lithography. The Fraunhofer EMFT began with this PhD thesis its work on this biopolymer. To date, the very high exposure doses required for the chemical photoreaction are still insufficient for industrial integration. However, the enzymatic modification of chitosan is under investigation to solve this problem. As long as these materials are not standardized, TSLM offers a simple and cost-efficient way to simulate the characteristics of these lithography photoresist materials.

Bibliography

[1] R. Cecchini and G. Pelosi. Diffraction: the first recorded observation. *IEEE Antennas and Propagation Magazine*, 32(2):27–30, 1990.

[2] Eugene Hecht. *Optics*. Pearson Education Inc, Harlow, 5th edition, 2017.

[3] Bahaa E. A. Saleh and Malvin Carl Teich. *Fundamentals of Photonics*. Wiley Series in Pure and Applied Optics. John Wiley & Sons, Chicester, 2nd edition, 2013.

[4] Martin Löffler-Mang. *Optische Sensoren und Messtechnik: Lasertechnik, Experimente, Light Barriers*. Studium. Vieweg+Teubner, Wiesbaden, 2012.

[5] Joseph W. Goodman. *Introduction to Fourier Optics*. McGraw-Hill international editions. Electrical engineering series. McGraw-Hill, New York, 2nd edition, 2004.

[6] Gordon E. Moore. Lithography and the future of Moore's law. *IEEE Solid-State Circuits Society Newsletter*, 11(3):37–42, 2006.

[7] Gordon E. Moore. Cramming more components onto integrated circuits, reprinted from electronics. *IEEE Solid-State Circuits Society Newsletter*, 11(3):33–35, 2006.

[8] Chris Mack. *Fundamental principles of optical lithography: The science of microfabrication*. Wiley, Chichester, reprinted with corr edition, 2012.

[9] Richard E. Novak. *Cleaning Technology in Semiconductor Device Manufacturing: Proceedings of the Sixth International Symposium*, volume 5 of *Proceedings*. Electrochemical Society, Pennington, NJ, 2000.

[10] Christian Koch and Titus J. Rinke. *Photolithography: Basics of microstructuring*. MicroChemicals GmbH, Ulm, 1st edition, 2017.

[11] Reinhard Voelkel, Uwe Vogler, Arianna Bramati, and Wilfried Noell. Micro-optics and lithography simulation are key enabling technologies for shadow printing lithography in mask aligners. *Advanced Optical Technologies*, 4(1), 2015.

[12] Reinhard Voelkel, Uwe Vogler, Andreas Bich, Pascal Pernet, Kenneth J. Weible, Michael Hornung, Ralph Zoberbier, Elmar Cullmann, Lorenz Stuerzebecher, Torsten Harzendorf, and Uwe D. Zeitner. Advanced mask aligner lithography: new illumination system. *Optics Express*, 18(20):20968–20978, 2010.

[13] A. Blicher. Physics of semiconductor power devices. *Reports on Progress in Physics*, 45(4):427–468, 1982.

[14] I. Papapolymerou, R. Franklin Drayton, and L.P.B. Katehi. Micromachined patch antennas. *IEEE Transactions on Antennas and Propagation*, 46(2):275–283, 1998.

[15] Mohamed Gad-el Hak. *The MEMS Handbook*. Mechanical engineering handbook series. CRC Press, Boca Ratón (Florida), 2001.

[16] Mikhail Merzlyakov. Integrated circuit thermopile as a new type of temperature modulated calorimeter. *Thermochimica Acta*, 403(1):65–81, 2003.

[17] Klavs F. Jensen. Microreaction engineering — is small better? *Chemical Engineering Science*, 56(2):293–303, 2001.

[18] Jeong Hoon Lee, Kyo Seon Hwang, Jaebum Park, Ki Hyun Yoon, Dae Sung Yoon, and Tae Song Kim. Immunoassay of prostate-specific antigen (PSA) using resonant frequency shift of piezoelectric nanomechanical microcantilever. *Biosensors & bioelectronics*, 20(10):2157–2162, 2005.

[19] Prem Pal, Yong-Jun Kim, and Sudhir Chandra. Front-to-back alignment techniques in microelectronics/MEMS fabrication: A review. *Sensor Letters*, 4(1):1–10, 2006.

[20] Dave A. Markle. A new projection printer. *Solid State Technology*, 17(6):50–53, 1974.

[21] Jere D. Buckley and Charles Karatzas. Step and scan: A systems overview of a new lithography tool. In Burn J. Lin, editor, *Optical/Laser Microlithography II*, SPIE Proceedings, pages 424–433. SPIE, 1989.

[22] Harry J. Levinson. *Principles of lithography*. SPIE, Bellingham, 3rd edition, 2010.

[23] Larry Zhang. Silicon process and manufacturing technology evolution: An overview of advancements in chip making. *IEEE Consumer Electronics Magazine*, 3(3):44–48, 2014.

[24] Nan Fu, Yanxiang Liu, Xiaolong Ma, and Zhanfeng Chen. EUV lithography: State-of-the-art review. *Journal of Microelectronic Manufacturing*, 2(2):1–6, 2019.

[25] L. W. Liebmann, S. M. Mansfield, A. K. Wong, M. A. Lavin, W. C. Leipold, and T. G. Dunham. TCAD development for lithography resolution enhancement. *IBM Journal of Research and Development*, 45(5):651–665, 2001.

[26] Bertrand Le-Gratiet, Jean De-Caunes, Maxime Gatefait, Auguste Lam, Alain Ostrovsky, Jonathan Planchot, Vincent Farys, Julien Ducoté, Marc Mikolajczak, Vincent Morin, Nicolas Chojnowski, Frank Sundermann, Alice Pelletier, Regis Bouyssou, Cedric Monget, Jean Damien Chapon, Bastien Orlando, Laurene Babaud, Celine Lapeyre, Emek Yesilada, Anna Szucs, Jean-Christophe Michel, Latifa Desvoivres, Onintza Ros Bengoechea, and Pascal Gouraud. Patterning critical dimension control for advanced logic nodes. *Journal of Micro/Nanolithography, MEMS, and MOEMS*, 14(2), 2015.

[27] SEMI. SEMI international standards: Compilation of terms.

[28] Cheng-Qun Gui, Willy van Buel, Frans G. C. Bijnen, and Joeri Lof. Extended front-to-back alignment capability for MEMS/MOEMS applications. In Roxann L. Engelstad, editor, *Emerging Lithographic Technologies VI*, SPIE Proceedings, page 867. SPIE, 2002.

[29] Christie R. K. Marrian and Donald M. Tennant. Nanofabrication. *Journal of Vacuum Science & Technology A: Vacuum, Surfaces, and Films*, 21(5):207–215, 2003.

[30] D. M. Tennant. Limits of conventional lithography. In Gregory Timp, editor, *Nanotechnology*, pages 161–205. Springer-Verlag, New York, NY, 1999.

[31] T.H.P. Chang, Marian Mankos, Kim Y. Lee, and Larry P. Muray. Multiple electron-beam lithography. *Microelectronic Engineering*, 57-58:117–135, 2001.

[32] Norio Saitou and Yoshio Sakitani. Cell projection electron-beam lithography. In David O. Patterson, editor, *Electron-Beam, X-Ray, and Ion-Beam Submicrometer Lithographies for Manufacturing IV*, SPIE Proceedings, page 11. SPIE, 1994.

[33] L. R. Harriott. SCALPEL: projection electron beam lithography. In A. U. Luccio and William W. MacKay, editors, *Proceedings of the 1999 Particle Accelerator Conference*, pages 595–599, Piscataway, N.J., 1999. Institute of Electrical and Electronics Engineers.

[34] Hsin-I Liu, Vito Dai, Avideh Zakhor, and Borivoje Nikolic. Reduced complexity compression algorithms for direct-write maskless lithography systems. In Michael J. Lercel, editor, *Emerging Lithographic Technologies X*, SPIE Proceedings. SPIE, 2006.

[35] Steven Steen, Sharee J. McNab, Lidija Sekaric, Inna Babich, Jyotica Patel, Jim Bucchignano, Michael Rooks, David M. Fried, Anna W. Topol, Jim R. Brancaccio, Roy Yu, John M. Hergenrother, James P. Doyle, Ron Nunes, Raman G. Viswanathan, Sampath Purushothaman, and Mary Beth Rothwell. Hybrid lithography: The marriage between optical and e-beam lithography. A method to study process integration and device performance for advanced device nodes. *Microelectronic Engineering*, 83(4-9):754–761, 2006.

[36] Heinz Kueck, Michael Bollerott, Wolfgang Doleschal, Andreas Gehner, Wolfram Grundke, Detlef Kunze, Rolf Melcher, Joerg Paufler, Rolf Seltmann, and Guenter Zimmer. New system for fast submicron laser direct writing. In Timothy A. Brunner, editor, *Optical/Laser Microlithography VIII*, SPIE Proceedings, pages 506–514. SPIE, 1995.

[37] Chris A. Spence, Cyrus E. Tabery, Gerald Cantrell, Leslie B. Dahl, Peter D. Buck, and William L. Wilkinson. Comparison of DUV wafer and reticle lithography: What is the resolution limit? In Brian J. Grenon and Kurt R. Kimmel, editors, *22nd Annual BACUS Symposium on Photomask Technology*, SPIE Proceedings, page 177. SPIE, 2002.

[38] Chunfei Li. *Nonlinear Optics: Principles and Applications*. Springer Singapore, Singapore, 2017.

[39] Jürgen Stampfl, Robert Liska, and Aleksandr Ovsianikov, editors. *Multiphoton lithography: Techniques, materials and applications*. Wiley-VCH, Wienheim, Germany, 2017.

[40] Jun-ichi Kato, Nobuyuki Takeyasu, Yoshihiro Adachi, Hong-Bo Sun, and Satoshi Kawata. Multiple-spot parallel processing for laser micronanofabrication. *Applied Physics Letters*, 86(4), 2005.

[41] Xian-Zi Dong, Zhen-Sheng Zhao, and Xuan-Ming Duan. Micronanofabrication of assembled three-dimensional microstructures by designable multiple beams multiphoton processing. *Applied Physics Letters*, 91(12), 2007.

[42] Xiaoxu Ma, Yoshiki Kato, Floris van Kempen, Yoshikazu Hirai, Toshiyuki Tsuchiya, Fred van Keulen, and Osamu Tabata. Experimental study of numerical optimization for 3-D microstructuring using DMD-based grayscale lithography. *Journal of Microelectromechanical Systems*, 24(6):1856–1867, 2015.

[43] Hans-Christoph Eckstein, Uwe D. Zeitner, Robert Leitel, Marko Stumpf, Philipp Schleicher, Andreas Bräuer, and Andreas Tünnermann. High dynamic grayscale lithography with an LED-based micro-image stepper. In Andreas Erdmann and Jongwook Kye, editors, *Optical Microlithography XXIX*, SPIE Proceedings. SPIE, 2016.

[44] U. Weidenmueller, P. Hahmann, L. Pain, M. Jurdit, D. Henry, Y. Laplanche, S. Manakli, and J. Todeschini. Critical dimension adapted alignment for EBDW. *Microelectronic Engineering*, 78-79:16–21, 2005.

[45] H. Alves, P. Hahmann, K.-H. Kliem, U. Weidenmueller, S. Jahr, C. G. Frase, D. Gnieser, H. Bosse, R. Zimmermann, and C. Arndt. E-beam direct write alignment strategies for the next generation node. In Frank M. Schellenberg, editor, *Emerging Lithographic Technologies XII*, SPIE Proceedings. SPIE, 2008.

[46] Raphaël Dawant, Robyn Seils, Serge Ecoffey, Rainer. Schmid, and Dominique Drouin. Hybrid cross correlation and line-scan alignment strategy for CMOS chips electron-beam lithography processing. *Journal of Vacuum Science & Technology B*, 40(1), 2022.

[47] Heidelberg Instruments Mikrotechnik GmbH. MLA 150: The advanced maskless aligner.

[48] Jinlun Zheng, Guodong Chen, Lu Wang, Xiaohang Sheng, Xing Liu, Tianyu Gao, Xiaozhong Xu, Peijun Zhao, and Jingsong Wei. Alignment method for rotary stage axis and optical axis in the polar coordinate direct laser writing system. *Optical Engineering*, 61(03), 2022.

[49] Merck KGaA. Safety data sheet according to regulation (EC) No. 1907/2006: AZ 400 K developer, 2022.

[50] Environmental Protection Agency. Substance evaluation conclusion as required by REACH article 48 and evaluation report for dipotassium tetraborate, 2018.

[51] Merck KGaA. Safety data sheet according to regulation (EC) No. 1907/2006: AZ developer, 2018.

[52] Merck KGaA. Technical datasheet: AZ inorganic developers: Sodium and potassium based photoresist developers, 2021.

[53] Merck KGaA. Safety data sheet according to regulation (EC) No. 1907/2006: AZ 726 MIF developer.

[54] Chun-Chi Lin, Chen-Chang Yang, Jiin Ger, Jou-Fang Deng, and Dong-Zong Hung. Tetramethylammonium hydroxide poisoning. *Clinical toxicology (Philadelphia, Pa.)*, 48(3):213–217, 2010.

[55] Seung-Hyun Park, Jungsun Park, Ki-Ho You, Hae-Chul Shin, and Hyun-Ock Kim. Tetramethylammonium hydroxide poisoning during a pallet cleaning demonstration. *Journal of occupational health*, 55(2):120–124, 2013.

[56] Chih-Kang Huang, Alan H. Hall, Ming-Ling Wu, Chen-Chang Yang, Dong-Zong Hung, Yan-Chiao Mao, and Jou-Fang Deng. Presentations of tetramethylammonium hydroxide dermal exposure and the valuable potential of diphoterine solution in decontamination: a retrospective observational study. *BMC pharmacology & toxicology*, 21(1):83, 2020.

[57] Izumi C. Mori, Carlos R. Arias-Barreiro, Apostolos Koutsaftis, Atsushi Ogo, Tomonori Kawano, Kazuharu Yoshizuka, Salmaan H. Inayat-Hussain, and Isao Aoyama. Toxicity of tetramethylammonium hydroxide to aquatic organisms and its synergistic action with potassium iodide. *Chemosphere*, 120:299–304, 2015.

[58] Directive 2010/75/EU of the European parliament and of the council.

[59] K. Hirano, J. Okamura, T. Taira, K. Sano, A. Toyoda, and M. Ikeda. An efficient treatment technique for TMAH wastewater by catalytic oxidation. *IEEE Transactions on Semiconductor Manufacturing*, 14(3):202–206, 2001.

[60] Yaoming Wang, Zenghui Zhang, Chenxiao Jiang, and Tongwen Xu. Electrodialysis process for the recycling and concentrating of tetramethylammonium hydroxide (TMAH) from photoresist developer wastewater. *Industrial & Engineering Chemistry Research*, 52(51):18356–18361, 2013.

[61] H. M. Citraningrum, J. C. Liu, and J. M. Chern. Removal of tetramethylammonium hydroxide from solution using ion exchange. *IEEE Transactions on Semiconductor Manufacturing*, 26(2):214–220, 2013.

[62] Sheng-Jie You, Galilee Uy Semblante, Yu-Pu Chen, and Tien-Chin Chang. Combined photocatalysis and membrane bioreactor for the treatment of feedwater containing thin film transistor-liquid crystal display discharge. *Environmental technology*, 36(21):2681–2690, 2015.

[63] T. K. Chen and J. N. Chen. Combined membrane bioreactor (MBR) and reverse osmosis (RO) system for thin-film transistor-liquid crystal display TFT-LCD, industrial wastewater recycling. *Water science and technology : a journal of the International Association on Water Pollution Research*, 50(2):99–106, 2004.

[64] T. K. Chen, C. H. Ni, and J. N. Chen. Nitrification-denitrification of opto-electronic industrial wastewater by anoxic/aerobic process. *Journal of environmental science and health. Part A, Toxic/hazardous substances & environmental engineering*, 38(10):2157–2167, 2003.

[65] V. Innocenzi, S. Zueva, M. Prisciandaro, I. de Michelis, A. Di Renzo, G. Di Mazziotti Celso, and F. Vegliò. Treatment of TMAH solutions from the microelectronics industry: A combined process scheme. *Journal of Water Process Engineering*, 31, 2019.

[66] Imtisal-e Noor, Jan Coenen, Andrew Martin, Olli Dahl, and Miriam Åslin. Experimental investigation and techno-economic analysis of tetramethylammonium hydroxide removal from wastewater in nano-electronics manufacturing via membrane distillation. *Journal of Membrane Science*, 579:283–293, 2019.

[67] Regulation (EC) No 1272/2008 of the European parliament and of the council.

[68] Microchemicals GmbH. Safety data sheet according to regulation (EC) No 1907/2006: DMSO, 2020.

[69] Herbert Meier and Klaus-Peter Zeller. The wolff rearrangement of alpha-diazo carbonyl compounds. *Angewandte Chemie International Edition in English*, 14(1):32–43, 1975.

[70] Y. Oppliger, P. Sixt, J. M. Stauffer, J. M. Mayor, P. Regnault, and G. Voirin. One-step 3D shaping using a gray-tone mask for optical and microelectronic applications. *Microelectronic Engineering*, 23(1-4):449–454, 1994.

[71] B. Wagner, H. J. Quenzer, W. Henke, W. Hoppe, and W. Pilz. Microfabrication of complex surface topographies using grey-tone lithography. *Sensors and Actuators A: Physical*, 46(1-3):89–94, 1995.

[72] K. Reimer, W. Henke, H. J. Quenzer, W. Pilz, and B. Wagner. One-level gray-tone design — mask data preparation and pattern transfer. *Microelectronic Engineering*, 30(1-4):559–562, 1996.

[73] Klaus Reimer, Hans Joachim Quenzer, M. Juerss, and Bernd Wagner. Micro-optic fabrication using one-level gray-tone lithography. In M. Edward Motamedi, Larry J. Hornbeck, and Kristofer S. J. Pister, editors, *Miniaturized Systems with Micro-Optics and Micromechanics II*, SPIE Proceedings, pages 279–288. SPIE, 1997.

[74] Torsten Harzendorf, Lorenz Stuerzebecher, Uwe Vogler, Uwe D. Zeitner, and Reinhard Voelkel. Half-tone proximity lithography. SPIE Proceedings. SPIE, 2010.

[75] Thomas Dillon. Continuous-tone grayscale mask fabrication using high-energy-beam-sensitive glass. *Journal of Micro/Nanolithography, MEMS, and MOEMS*, 3(4):550, 2004.

[76] T. Fujita, H. Nishihara, and J. Koyama. Blazed gratings and Fresnel lenses fabricated by electron-beam lithography. *Optics letters*, 7(12):578–580, 1982.

[77] Daniel W. Wilson, Paul D. Maker, Richard E. Muller, Pantazis Z. Mouroulis, and Johan Backlund. Recent advances in blazed grating fabrication by electron-beam lithography. In Pantazis Z. Mouroulis, Warren J. Smith, and R. Barry Johnson, editors, *Current Developments in Lens Design and Optical Engineering IV*, SPIE Proceedings, page 115. SPIE, 2003.

[78] Wei-Er Lu, Xian-Zi Dong, Wei-Qiang Chen, Zhen-Sheng Zhao, and Xuan-Ming Duan. Novel photoinitiator with a radical quenching moiety for confining radical diffusion in two-photon induced photopolymerization. *Journal of Materials Chemistry*, 21(15):5650, 2011.

[79] L. Jay Guo. Recent progress in nanoimprint technology and its applications. *Journal of Physics D: Applied Physics*, 37(11):123–141, 2004.

[80] Clivia M. Sotomayor Torres, editor. *Alternative Lithography: Unleashing the Potentials of Nanotechnology*. Nanostructure Science and Technology, 1571-5744. Springer US and Imprint and Springer, Boston, MA, 2003.

[81] Mark Neisser and Stefan Wurm. ITRS lithography roadmap: 2015 challenges. *Advanced Optical Technologies*, 4(4), 2015.

[82] Kazuya Fukuhara, Masato Suzuki, Masaki Mitsuyasu, Takuya Kono, Tetsuro Nakasugi, Yonghyun Lim, and Wooyung Jung. Overlay control for nanoimprint lithography. In Christopher Bencher and Joy Y. Cheng, editors, *Emerging Patterning Technologies*, SPIE Proceedings. SPIE, 2017.

[83] Samuel Tobias Howell, Anya Grushina, Felix Holzner, and Juergen Brugger. Thermal scanning probe lithography-a review. *Microsystems & nanoengineering*, 6:21, 2020.

[84] Colin D. Rawlings, Tero S. Kulmala, Martin Spieser, Felix Holzner, Thomas Glinsner, Arne Schleunitz, and Franziska Bullerjahn. Single-nanometer accurate 3D nanoimprint lithography with master templates fabricated by nanofrazor lithography. In Eric M. Panning and Martha I. Sanchez, editors, *Novel patterning technologies 2018*, page 37, 2018.

[85] Yole Développement. Status of the camera module industry - focus on wafer level optics: 2019 report.

[86] Yole Développement. Status of the MEMS industry 2022: Market and technology report.

[87] Yole Développement. Status of the microfluidics industry 2022: Market and technology report.

[88] Yole Développement. Nano-imprint technology trends for semiconductor applications 2019.

[89] Yole Développement. Lithography and bonding equipment 2022: Focus on more than Moore: Market and technology report.

[90] F. H. Dill, A. R. Neureuther, J. A. Tuttle, and E. J. Walker. Modeling projection printing of positive photoresists. *IEEE Transactions on Electron Devices*, 22(7):456–464, 1975.

[91] F. H. Dill. Optical lithography. *IEEE Transactions on Electron Devices*, 22(7):440–444, 1975.

[92] K. L. Konnerth and F. H. Dill. In-situ measurement of dielectric thickness during etching or developing processes. *IEEE Transactions on Electron Devices*, 22(7):452–456, 1975.

[93] F. H. Dill, W. P. Hornberger, P. S. Hauge, and J. M. Shaw. Characterization of positive photoresist. *IEEE Transactions on Electron Devices*, 22(7):445–452, 1975.

[94] Chris A. Mack. Prolith: A comprehensive optical lithography model. In Harry L. Stover, editor, *Optical Microlithography IV*, SPIE Proceedings, page 207. SPIE, 1985.

[95] Chris A. Mack. *Inside Prolith TM: A comprehensive guide to optical lithography simulation : for the Prolith family of lithography simulation tools, v5.0.* Finle Technologies, Austin, Texas, 1997.

[96] Tim Fühner, Thomas Schnattinger, Gheorghe Ardelean, and Andreas Erdmann. Dr.LiTHO: a development and research lithography simulator. In Donis G. Flagello, editor, *Optical Microlithography XX*, SPIE Proceedings. SPIE, 2007.

[97] Marcel Heller, Dieter Kaiser, Maik Stegemann, Georg Holfeld, Nicoló Morgana, Jens Schneider, and Daniel Sarlette. Grayscale lithography: 3D structuring and thickness control. In Will Conley, editor, *Optical Microlithography XXVI*, SPIE Proceedings. SPIE, 2013.

[98] James Loomis, Dilan Ratnayake, Curtis McKenna, and Kevin M. Walsh. Grayscale lithography—automated mask generation for complex three-dimensional topography. *Journal of Micro/Nanolithography, MEMS, and MOEMS*, 15(1), 2016.

[99] W. Henke, W. Hoppe, H. J. Quenzer, P. Staudt-Fischbach, and B. Wagner. Simulation and experimental study of gray-tone lithography for the fabrication of arbitrarily shaped surfaces. In *Micro Electro Mechanical Systems, 1994, MEMS '94, Proceedings, IEEE Workshop on*, pages 205–210. IEEE / Institute of Electrical and Electronics Engineers Incorporated, 1994.

[100] V.A.K. Temple and M. S. Adler. The theory and application of a simple etch contour for near ideal breakdown voltage in plane and planar p-n junctions. *IEEE Transactions on Electron Devices*, 23(8):950–955, 1976.

[101] V.A.K. Temple. Junction termination extension (JTE), a new technique for increasing avalanche breakdown voltage and controlling surface electric fields in p-n junctions. In *1977 International Electron Devices Meeting*, pages 423–426. IRE, 1977.

[102] Eugene A. Imhoff, Fritz J. Kub, and Karl D. Hobart. Grayscale junction termination for high-voltage SiC devices. *Materials Science Forum*, 615-617:691–694, 2009.

[103] Jens Schneider, Henning Feick, Dieter Kaiser, Marcel Heller, and Daniel Sarlette. 3D lithography for implant applications. In *2013 International Semiconductor Conference Dresden - Grenoble (ISCDG)*, pages 1–4. IEEE, 2013.

[104] IMEC. Linescan hyperspectral image sensor.

[105] Calum Williams, George S. D. Gordon, Timothy D. Wilkinson, and Sarah E. Bohndiek. Grayscale-to-color: Scalable fabrication of custom multispectral filter arrays. *ACS photonics*, 6(12):3132–3141, 2019.

[106] Andy Lambrechts, Pilar Gonzalez, Bert Geelen, Philippe Soussan, Klaas Tack, and Murali Jayapala. A CMOS-compatible, integrated approach to hyper- and multispectral imaging. In *2014 IEEE International Electron Devices Meeting*, pages 10.5.1–10.5.4. IEEE, 2014.

[107] P. Baeck, J. Blommaert, S. Delalieux, B. Delauré, S. Livens, D. Nuyts, A. Sima, G. Jacquemin, and J.P. Goffart. High resolution vegetation mapping with a novel compact hyperspectral camera system. *Precision Agriculture*, (11119), 2016.

[108] David Bannon. Cubes and slices. *Nature Photonics*, 3(11):627–629, 2009.

[109] J. Kim, S. Park, D. Kwak, H. Ko, W. Carr, J. Buss, and D. D. Cho. Robust SOI process without footing for ultra high-performance microgyroscopes. In *Digest of technical papers*, pages 1691–1694, New York, 2003. Institute of Electrical and Electronics Engineers.

[110] W. E.N. Xiaolong, Pengfei Yang, C. H.U. Zhaozhi, Chunrong Peng, L. I.U. Yutao, and W. U. Shuang. MEMS-based electric field sensor with environmental adaptability consideration and its application in the near-ground atmosphere. *Journal of Physics: Conference Series*, 1775(1), 2021.

[111] Barry E. DeMartini, Jeffrey F. Rhoads, Kimberly L. Turner, Steven W. Shaw, and Jeff Moehlis. Linear and nonlinear tuning of parametrically excited MEMS oscillators. *Journal of Microelectromechanical Systems*, 16(2):310–318, 2007.

[112] B. Morgan and R. Ghodssi. Vertically-shaped tunable MEMS resonators. *Journal of Microelectromechanical Systems*, 17(1):85–92, 2008.

[113] Brian Morgan and Reza Ghodssi. Design and simulation of comb-drive actuators incorporating gray-scale technology for tailored actuation characteristics (invited paper). In Carles Cane, Jung-Chih Chiao, and Fernando Vidal Verdu, editors, *Smart Sensors, Actuators, and MEMS II*, SPIE Proceedings, pages 468–476. SPIE, 2005.

[114] Martin Oellers, Frank Bunge, Frieder Lucklum, Sander van den Driesche, and Michael J. Vellekoop. Novel design of additively manufactured micromixer in a microchannel comprising mounting and sealing elements. In *EUROSENSORS*, page 1000, Basel Switzerland, 2018. MDPI.

[115] Martin Oellers, Frieder Lucklum, and Michael J. Vellekoop. On-chip mixing of liquids with swap structures written by two-photon polymerization. *Microfluidics and Nanofluidics*, 24(1), 2020.

[116] Ran He, Doruk Yunus, Christopher Uhl, Wentao Shi, Salman Sohrabi, and Yaling Liu. Fabrication of circular microfluidic channels through grayscale dual-projection lithography. *Microfluidics and Nanofluidics*, 21(1), 2017.

[117] Stephen C. Balmert, Cara Donahue Carey, Gabriel D. Falo, Shiv K. Sethi, Geza Erdos, Emrullah Korkmaz, and Louis D. Falo. Dissolving undercut microneedle arrays for multicomponent cutaneous vaccination. *Journal of controlled release : official journal of the Controlled Release Society*, 317:336–346, 2020.

[118] Ran He, Shunqiang Wang, Geoffrey Andrews, Wentao Shi, and Yaling Liu. Generation of customizable micro-wavy pattern through grayscale direct image lithography. *Scientific reports*, 6, 2016.

[119] Bassem Badawi, Olfa Sayadi, Ignaz Eisele, and Christoph Kutter. Three-state lithography model: an enhanced mathematical approach to predict resist characteristics in grayscale lithography processes. *Journal of Micro/Nanopatterning, Materials, and Metrology*, 20(01), 2021.

[120] Merck KGaA. Technical data sheet: AZ ECI 3000 photoresist.

[121] J. R. Sheats. Reciprocity failure in novolak/diazoquinone photoresist with 364-nm exposure. *IEEE Transactions on Electron Devices*, 35(1):129–131, 1988.

[122] AZ Electronic Materials. AZ BARLi II: Solvent compatible bottom antireflective coating for i-line process.

[123] AZ Electronic Materials. Non pfos & non pfoa tarc: Introduction AZ AQUATAR-VIII-series for i-line, KrF, and ArF application. 2007.

[124] Leonhard Sturm-Rogon. *Realisierung und Charakterisierung eines neuen Konzepts für siliziumbasierte Sperrschichtfeldeffekttransistoren*. PhD thesis, Universität der Bundeswehr München, 2022.

[125] U.S. Energy Information Administration. Short-term energy outlook November 2022.

[126] Pankaj Bhardwaj, Andreas Erdmann, and Robert Leitel. Modeling of grayscale lithography and calibration with experimental data for blazed gratings. In Daniel G. Smith, Frank Wyrowski, and Andreas Erdmann, editors, *Computational Optics 2021*, page 17. SPIE / International Society for Optical Engineering, 2021.

[127] Jean-Louis Leclercq, Olivier Soppera, Mathieu Caillau, Céline Chevalier, Pierre Crémillieu, Thierry Delair, Emmanuelle Laurenceau, Yann Chevolot, Benjamin Leuschel, Cédric Ray, Christophe Moulin, Christian Jonin, Emmanuel Benichou, Pierre-François Brevet, and Christelle Yeromonahos. Sub-micron lines patterning into silica using water developable chitosan bioresist films for eco-friendly positive tone e-beam and uv lithography. In Jongwook Kye and Soichi Owa, editors, *Optical microlithography XXXI*, page 29, 2018.

Curriculum Vitae

2011 – 2015	B.S. in Engineering Physics, University of Applied Sciences, Munich, Germany.
2015 – 2017	M.S. in Micro- and Nanotechnology, University of Applied Sciences, Munich, Germany.
2017 – Present	Ph.D. student in Physics, Bundeswehr University, Munich, Germany.

Publications

[1] Bassem Badawi, Olfa Sayadi, Ignaz Eisele, Christoph Kutter, "Three-state lithography model: an enhanced mathematical approach to predict resist characteristics in grayscale lithography processes," Journal of Micro/Nanopatterning, Materials, and Metrology **20**, 014601 (2021), DOI:10.1117/1.JMM.20.1.014601.

[2] Bassem Badawi, Christoph Kutter, "Application of the three-state lithography model for grayscale lithography," Proc. SPIE 12472, 37th European Mask and Lithography Conference, 124720D (2022), DOI:10.1117/12.2641182.